



Study of Na-M-(O,F) phases: synthesis,  
crystal chemistry and electrochemical  
performance in sodium – based batteries

## **Jessica María Nava Avendaño**

PhD dissertation

Materials Science Program

**Director: Dr. M. Rosa Palacín Peiró**

**UAB Mentor: Dr. José A. Ayllón Esteve**

Chemistry Department

Faculty of Sciences



2014





Estudio de fases Na-M-(O,F): síntesis,  
cristaloquímica y rendimiento  
electroquímico en baterías de sodio

**Jessica María Nava Avendaño**

Tesis Doctoral

Programa de Doctorado en Ciencia de Materiales

**Director: Dra. M. Rosa Palacín Peiró**

**Tutor UAB: Dr. José A. Ayllón Esteve**

Departamento de Química

Facultad de Ciencias



2014



*To my family, the country of my heart*

## Acknowledgements

I would like to deeply acknowledge my advisor Dr. M.R. Palacín for her unconditional support and guidance. Her optimism and diligence have encouraged me to work hard and commit with this project. She gave me the opportunity to keep learning and has trusted me all the way on. With her I am greatly indebted. I am also especially thankful to Dr. C. Frontera, who has walked with me along the elucidation of crystal structures and had the patience to discuss all the crazy ideas that came to my mind. A vosaltres, moltes gràcies per acompanyar-me en aquesta experiència de vida!

Also, I would like to acknowledge all the collaborative work with Dr. J.A. Ayllón, the UAB mentor of this work, which widened the scope of the synthesis methods used and with Dr. M. Alfredsson for her disposition to help me and for giving me the opportunity to learn XAS basics. To Dr. G. Rousse, my gratitude for her compromise to the structural studies of the sodium titanate developed during this work and to Dr. P. Senguttuvan for all the advice for the better development of the *in situ* experiments. Many thanks to Dr. M. Morcrette and Dr. C. Masquelier for their contribution to the *in situ* XRPD measurements developed at Université de Picardie Jules Verne and Dr. F. Fauth for his help to the *in operando* XRPD experiments carried out at ALBA synchrotron. I am also indebted to Dr. E. Molins for the single crystal measurements of the vanadium compounds, and to Dr. M. E. Arroyo y de Dompablo for the DFT calculations presented in this work. I also acknowledge the Fundació Empresa i Ciència and MICINN for funding.

To Dr. A. Ponrouch an immense MERCI for his many advices and for his patience every time I knocked to his door to ask for help.

To Dr. J. Oró goes my infinite gratitude for the countless hours dedicated to help me with the characterization of my always tricky samples and for supporting me professionally and personally.

This thesis was carried out in the company of numerous charismatic, creative and friendly coworkers. I would like to extend my acknowledgement to all the ICMAB members, and

especially, to the members Solid State Chemistry Department for sharing so many anecdotes with me. In my memories I will always preserve all the dances, relaxing cups of café con leche, gordurillas variadas, laughter and drama shared during these years. You welcomed me since day one and for that I am greatly thankful.... It has been a blast!

Last but not least, I would like to thank my family for giving me the opportunity to follow my dreams. You are my greatest gift. Also, to the city of Barcelona for being the perfect atmosphere that introduced me to all the marvelous people I have met within the years. This place has become my home and all the good friends gained have become my family. To all of you that supported me in the hardest times and celebrated with me the small daily victories... GRACIAS.

## Abstract

This thesis reports on the preparation, using mostly mild synthetic routes, crystal chemical characterization and electrochemical testing in sodium based batteries of Na- M-(O,F) phases ( M= Ti, V, Mn and Mo). The most significant results achieved for M=Mn concern the synthesis in aqueous medium of  $\text{Na}_2\text{MnF}_5$ ,  $\text{NaMnF}_3$  and the novel oxyfluoride  $\text{NaMnMoO}_3\text{F}_3 \cdot \text{H}_2\text{O}$  which exhibits a layered structure with  $a = 3.5947(1)$ ,  $b = 21.246(1)$ , and  $c = 7.3893(2)$  Å cell parameters and  $Cmcm$  (No.63) space group.

In the case of M=V, solvothermal methods allowed to prepare different phases such as the already known  $\text{NaVF}_4$  or the new cryolite  $\text{Na}_{3-\delta}\text{VOF}_5$  ( $a = 5.54034(2)$  Å,  $b = 5.68041(2)$  Å,  $c = 7.95229(3)$  Å cell parameters,  $\beta = 90.032(7)^\circ$  and space group  $P21/n$  (n°14)) by modifying the synthesis conditions. The chiolite  $\text{Na}_{5-\delta}\text{V}_3\text{F}_{14-\delta}$  ( $a = 10.5482(2)$  Å,  $b = 10.4887(1)$  Å and  $c = 10.3243(1)$  Å and  $Cmc2_1$  (n° 36) space group) was also prepared at 100 °C but using higher HF concentration, and was characterized by means of neutron and SXRPD data.

For M=Ti, an oxyfluoride with chiolite related structure with space group  $Cmca$  (n° 64) and cell parameters  $a = 10.496(2)$  Å,  $b = 10.398(1)$  Å and  $c = 10.291(1)$  Å.  $\text{Na}_5\text{Ti}_3\text{O}_3\text{F}_{11}$  was prepared by a microwave assisted method.

The electrochemical performance of all such fluoride and oxyfluoride phases was found to be poor if any, which is presumably related to the high insulating character of fluorides and to a redox operation potential outside the stability window of conventional electrolytes, as deduced in some specific cases from DFT calculations.

Finally, additional research was carried out to get some insight on the factors affecting the capacity retention of  $\text{Na}_2\text{Ti}_3\text{O}_7$  upon electrochemical cycling, and which included both *in situ* experiments and ageing tests. Preliminary conclusions seem to indicate that capacity fading is mostly related to reactivity with the electrolyte and not related to structural degradation.

## Resumen

En la presente Tesis se describe el estudio de fases en los sistemas Na- M-(O, F) con (M = Ti, V, Mn y Mo), incluyendo la preparación, en condiciones suaves, la caracterización cristaloquímica y el ensayo electroquímico en baterías de sodio. Los resultados más significativos obtenidos para M = Mn comprenden la síntesis en medio acuoso de los fluoruros  $\text{Na}_2\text{MnF}_5$  y  $\text{NaMnF}_3$ , y del nuevo oxifluoruro  $\text{NaMnMoO}_3\text{F}_3 \cdot \text{H}_2\text{O}$ , que presenta una estructura laminar con parámetros de celda  $a = 3.5947(1)$ ,  $b = 21.246(1)$  y  $c = 7.3893(2)$  y grupo espacial  $Cmcm$  (No.63).

En el caso de M = V, la síntesis por vía solvotermal en diferentes condiciones permitió la preparación de diversas fases tales como la ya conocida  $\text{NaVF}_4$  o la nueva criolita  $\text{Na}_{3-6}\text{VOF}_5$  ( $a = 5.54034(2) \text{ \AA}$ ,  $b = 5.68041(2) \text{ \AA}$ ,  $c = 7.95229(3) \text{ \AA}$ ,  $\beta = 90.032(7)$  y grupo espacial  $P21/n$  (n°14)). También se preparó a  $100 \text{ }^\circ\text{C}$  la quiolita  $\text{Na}_{5-6}\text{V}_3\text{F}_{14-6}$  ( $a = 10.5482(2) \text{ \AA}$ ,  $b = 10.4887(1) \text{ \AA}$  y  $c = 10.3243(1) \text{ \AA}$ , y grupo espacial  $Cmc2_1$  (N° 36)) en un medio de reacción con concentraciones de más altas, la cual fue caracterizada mediante difracción de neutrones y radiación sincrotrón.

En el caso de M= Ti, se preparó el oxifluoruro  $\text{Na}_5\text{Ti}_3\text{O}_3\text{F}_{11}$  mediante síntesis asistida por microondas. Su estructura cristalina es también de tipo quiolita con grupo espacial  $Cmca$  (n° 64) y parámetros de celda  $a = 10.496(2) \text{ \AA}$ ,  $b = 10.398(1) \text{ \AA}$  y  $c = 10.291(1) \text{ \AA}$ .

El rendimiento electroquímico de dichos fluoruros y oxifluoruros resultó ser limitado, presumiblemente debido al carácter altamente aislante de los fluoruros y al hecho de que los potenciales redox, se encuentran fuera de la ventana de la estabilidad de los electrolitos convencionales, lo cual pudo confirmarse en algunos casos específicos mediante cálculos DFT.

Finalmente, se llevó a cabo un estudio adicional dirigido a determinar los factores que afectan el comportamiento electroquímico y más concretamente la retención de la capacidad del  $\text{Na}_2\text{Ti}_3\text{O}_7$ . Éste incluyó medidas *in situ* y ensayos de envejecimiento en contacto con el electrolito. Las conclusiones preliminares parecen indicar que la pérdida

de la capacidad no está relacionada principalmente con la degradación estructural del compuesto sino con su reactividad con el electrolito.



## Table of Contents

CHAPTER 1: Introduction.....	3
1.1 Relevant crystal structures of (oxy)fluorinated materials .....	2
1.1.2. Crystal structures with isolated octahedra: $A_3MF_6$ and $A_2BMF_6$ .....	3
1.1.3. Chain structures: $A_2MF_5$ .....	4
1.1.4. Layered structures .....	5
1.1.4.1. Chiolite ( $A_5M_3F_{14}$ ).....	5
1.1.5. 3D Framework structures .....	6
1.1.5.1. Perovskites.....	6
1.2. Common synthetic methods to obtain (oxy)fluorinated compounds .....	8
1.3. Introduction to battery basics .....	10
1.3.1. Sodium ion batteries .....	12
1.3.2. Positive electrodes .....	13
1.3.3. Negative electrodes .....	14
1.4. Motivation of the study.....	16
2.1 Synthesis and compositional characterization of materials .....	18
2.1.1. Synthetic routes.....	18
2.1.2. Chemical Analysis .....	19
2.1.3. Magnetic measurements.....	19
2.1.4. Scanning Electron Microscopy (SEM) .....	20
2.1.5. Attenuated total reflection infrared (ATR-IR) .....	20
2.2. Structural characterization techniques .....	21
2.2.1. X- ray diffraction (XRD) .....	21
2.2.2. Neutron powder diffraction (NPD) .....	22
2.2.3. Pauling's second rule: anion distribution in crystals .....	23

2.2.4. Selected area electron diffraction (SAED) .....	23
2.2.5. X-ray absorption .....	24
2.2.5.1. K- edge of vanadium compounds .....	24
2.2.5.2. In situ X-ray absorption experiment.....	24
2.3. Electrochemical characterization.....	25
2.3.1. General setup .....	25
2.3.2. Electrode preparation .....	26
2.3.3. Galvanostatic method.....	27
2.3.4.1. In situ X-ray diffraction experiment .....	28
CHAPTER 3: .....	31
3.1. Synthesis of sodium manganese fluorides. ....	32
3.2. NaMnF <sub>3</sub> .....	33
3.2.1. Chemical analysis and microstructural characterization .....	33
3.3. Na <sub>2</sub> MnF <sub>5</sub> .....	35
3.3.1. Chemical analysis and microstructural characterization .....	35
3.4. Electrochemical characterization.....	37
3.4.1. Electrode preparation .....	37
3.4.2. Electrochemical testing .....	39
3.5. Sodium manganese (oxy)fluorides. ....	44
3.5.1. NaMnOF <sub>2</sub> · 2.8H <sub>2</sub> O .....	44
3.5.1.1. Chemical analysis and microstructural characterization .....	45
3.5.2. NaMnMoO <sub>3</sub> F <sub>3</sub> · H <sub>2</sub> O .....	49
3.5.2.1. Chemical analysis and microstructural characterization .....	50
3.8. Electrochemical characterization.....	60
4.1. Synthesis of sodium vanadium (oxy)fluorides.....	63

4.2. NaVF <sub>4</sub> .....	65
4.2.1. Chemical analysis and microstructural characterization .....	65
4.3. Cryolite-type phase: Na <sub>3-δ</sub> VOF <sub>5</sub> .....	67
4.3.1. Chemical analysis and microstructural characterization .....	67
4.4. Na <sub>5-δ</sub> V <sub>3</sub> F <sub>14</sub> .....	75
4.4.1. Chemical analysis and microstructural characterization .....	75
4.5. Electrochemical characterization.....	89
CHAPTER 5: .....	92
5.1. Chiolite- type: Na <sub>5-δ</sub> Ti <sub>3</sub> O <sub>3-δ</sub> F <sub>11+δ</sub> .....	93
5.1.1. Chemical analysis and microstructural characterization .....	93
5.2.2. Electrochemical characterization .....	99
5.2. Studies on stability and redox mechanism Na <sub>2</sub> Ti <sub>3</sub> O <sub>7</sub> .....	100
5.2.1. Synthesis of Na <sub>2</sub> Ti <sub>3</sub> O <sub>7</sub> .....	100
5.2.2. Electrochemical performance of Na <sub>2</sub> Ti <sub>3</sub> O <sub>7</sub> .....	102
5.2.3. Studies on the redox mechanism of Na <sub>2</sub> Ti <sub>3</sub> O <sub>7</sub> .....	106
5.2.3.1. In situ X- ray absorption measurements .....	106
5.2.3.2. In operando XRPD measurements .....	109
5.2.3.3. Stability of Na <sub>2</sub> Ti <sub>3</sub> O <sub>7</sub> in different electrolytes. ....	113
General conclusions.....	116
REFERENCES.....	120

## List of Figures

Figure 1.1. Schematic view of the crystal structure of $\text{Na}_3\text{AlF}_6$ cryolite.....	4
Figure 1.2. Schematic view of the $\text{Na}_2\text{MnF}_5$ chain- type structure.....	5
Figure 1.3. Schematic view of the crystal structure of $\text{Na}_5\text{Al}_3\text{F}_{14}$ chiolite. ....	6
Figure 1.4. Schematic view of the crystal structure of the cubic $\text{SrTiO}_3$ perovskite. ....	7
Figure 1.6. Schematic of an operating Na- ion battery. Modified from reference [66].....	11
Figure 1.7. Scheme depicting electrode electrochemical potentials vs potential window of the electrolyte (adapted from reference[69]). The open- circuit voltage ( $V_{OC}$ ) is determined by the difference between the electrochemical potential of the electrodes ( $\mu_A - \mu_C$ ).....	12
Figure 2.1. ED patterns taken during rotation along a specific crystal axis (left) and the corresponding 2D projection and diffraction spot indexation (right). ....	24
Figure 2.2. Scheme of the Swagelok cell used to perform the electrochemical tests.....	25
Figure 2.3. Fifth cycle voltammograms for the electrolytes 1 M $\text{NaClO}_4$ in EC:PC and 1 M $\text{NaClO}_4$ in EMS:PC.....	26
Figure 2.4. (Left) Potential vs capacity profile corresponding to the SP carbon blank experiment carried out between 4.8 and 1.0 V in 1 M $\text{NaClO}_4$ in EC: PC at C/25. (Right) Plot showing the evolution of the electrochemical capacity with cycle number for the blank experiment.....	28
Figure 2.5. Potential vs capacity profile corresponding to the SP carbon blank experiment carried out between OCV and 0.1 V in 1 M $\text{NaClO}_4$ in EC: PC at C/25. In situ experiments .....	28
Figure 2.6. Electrochemical cell used for <i>in situ</i> X-ray diffraction measurements constituted by three main parts. A) Stainless steel plunger with a Be on the top where Na metal is placed. B) Body of the cell covered with a Mylar to isolate it from the plunger. C) Counter electrode current collector with Be window, where the active material to test is placed in contact with the separator. ....	29

Figure 2.7. Experimental set up for the <i>in operando</i> of synchrotron X- ray diffraction experiment.....	29
Figure 3.1. SEM images at different magnifications for NaMnF <sub>3</sub> .....	33
Figure 3.2. XRPD pattern of NaMnF <sub>3</sub> precipitated from a basic aqueous solution. (♦) denotes a peak corresponding to a small amount of MnF <sub>2</sub> impurity present in the sample (2θ= 25.8°). .....	34
Figure 3.3. Inverse susceptibility vs temperature of NaMnF <sub>3</sub> measured with an applied field of 100 Oe. Observed Néel temperature $T_N= 66$ K.....	34
Figure 3.4. SEM images of Na <sub>2</sub> MnF <sub>5</sub> micrometric particles obtained from: a) NaMnO <sub>4</sub> in ethanol/water and b) Mn <sub>2</sub> O <sub>3</sub> in water.....	35
Figure 3.5. XRPD pattern of Na <sub>2</sub> MnF <sub>5</sub> obtained from aqueous solutions using as manganese precursors: a) NaMnO <sub>4</sub> (route A) and b) Mn <sub>2</sub> O <sub>3</sub> (Route B). .....	36
Figure 3.6. Plot of the inverse of susceptibility vs, temperature for Na <sub>2</sub> MnF <sub>5</sub> obtained with an applied field of 100 Oe.....	37
Figure 3.7. a) Typical SEM images corresponding to NaMnF <sub>3</sub> ball-milled for 2 and 12 hours with 40% SP carbon. b) XRPD patterns for mixtures of NaMnF <sub>3</sub> and 40% SP carbon ball- milled for different periods of time (0.5h to 12h) at 350 rpm. ....	38
Figure 3.8. XRPD patterns of Na <sub>2</sub> MnF <sub>5</sub> as prepared and after mixing with 40% of SP carbon by 15 min hand milling (HM) or ball- milling (BM) for different periods of time (0.5 to 12h) at 350 rpm. ....	39
Figure 3.9. a) Electrochemical curve of NaMnF <sub>3</sub> mixed with 40% SP carbon cycled vs Na <sup>+</sup> . b) Variation of the capacity as function of the number of cycles. Charge capacity is shown in full circles, discharge capacity in hollow ones. ....	40
Figure 3.10. Potential vs. capacity profile for Na <sub>2</sub> MnF <sub>5</sub> (hand- milled) tested at C/25 in 1 M NaClO <sub>4</sub> in EC: PC. ....	41
Figure 3.11. a) Potential vs. capacity profile for Na <sub>2</sub> MnF <sub>5</sub> (0.5 h ball- milled) cycled at C/25 with electron transfer in each half oxidation-reduction cycle limited to x=0.5 (pink dotted line) and x=0.8 (black continuous line). b) Capacity achieved upon oxidation (full symbol)	

and reduction (hollow symbol) as function of the number of cycles for the experiments with oxidation limited to $x=0.5$ (pink circles) and $x=0.8$ (black square). .....	41
Figure 3.12. XRPD patterns taken <i>in situ</i> and corresponding to electrodes containing $\text{Na}_2\text{MnF}_5$ at open circuit potential (1) and after full oxidation (2). Indexed diffraction peaks correspond to Be metal used in the electrochemical cell. (see Section 2.3) .....	42
Figure 3.13. XRPD patterns of the as precipitated brownish sample a) before and b) after pelletizing at 2 bar for 50 s, and c) after heating 100 °C, which yields to decomposition to a mixture containing $\text{NaMnF}_4$ and additional unidentified product(s) (peaks marked with stars). .....	44
Figure 3.14 Typical SEM image of the as precipitated brown sodium manganese oxyfluoride. ....	45
Figure 3.15. ATR-IR spectrum of the as precipitated brown sodium manganese oxyfluoride. 46	
Figure 3.16. Plot of the inverse of magnetic susceptibility vs. temperature for $\text{NaMnOF}_2 \cdot 2.8\text{H}_2\text{O}$ with an applied field of 100 Oe. ....	47
Figure 3.17. Pattern fitting of SXPDP data (above) and Neutron diffraction data (below). Experimental pattern (red dots), calculated profile (black continuous line) and difference pattern at the bottom (blue). Bragg positions are denoted by vertical bars. ....	48
Figure 3.18. SEM images at different magnifications for $\text{NaMnMoO}_3\text{F}_3 \cdot \text{H}_2\text{O}$ .....	50
Figure 3.19. ATR-IR spectrum of as-prepared sample showing characteristic vibration bands of the water contained in the crystal lattice at 1651 $\text{cm}^{-1}$ , 3516 $\text{cm}^{-1}$ and 3563 $\text{cm}^{-1}$ . ....	51
Figure 3.20. Inverse of the magnetic susceptibility as a function of temperature with and applied field of 1000 Oe. ....	52
Figure 3.21. Typical XRPD patterns (standard (above) and side loaded (below) sample holders) for $\text{NaMnMoO}_3\text{F}_3 \cdot \text{H}_2\text{O}$ by Route 2. ....	52
Figure 3.22. Typical TEM image for $\text{NaMnMoO}_3\text{F}_3 \cdot \text{H}_2\text{O}$ and electron diffraction patterns corresponding to the b) [010], c) [10-4] and d) [001] zone axes. The circles marked in b) correspond to double diffraction spots and the white arrows in c) indicate diffuse extra lines at positions between the $0k0$ and $h0l$ reflections. ....	55

Figure 3.25. Scheme depicting coordination environments around metal atoms. ....	60
Figure 3.26. <i>In situ</i> XRPD patterns corresponding to electrodes containing $\text{NaMnMoO}_3\text{F}_3 \cdot \text{H}_2\text{O}$ upon electrochemical oxidation and reduction. Indexed diffraction peaks correspond to Be metal used in the electrochemical cell. (see Section 2.3) while arrows identify the diffraction peaks corresponding to $\text{NaMnMoO}_3\text{F}_3 \cdot \text{H}_2\text{O}$ .....	61
Figure 4.1. Selected XRPD patterns corresponding sodium vanadium (oxy)fluorides prepared with Na:V ratio of 1 at 100 °C and 200 °C. XRPD lines marked (♦) correspond to chiolite- type structure. ....	64
Figure 4.2. XRPD pattern of $\text{NaVF}_4$ prepared by solvothermal synthesis (black) and reference pattern (green). A typical SEM image of the as prepared sample where the morphology of the crystals can be appreciated is shown as inset. ....	66
Figure 4.3. Plot of the inverse of the magnetic susceptibility vs the temperature for $\text{NaVF}_4$ measured with an applied field of 5K Oe. ....	67
Figure 4.4a. Typical SEM images at two different magnifications of the as prepared cryolite type pure phase together with b) chemical mapping. ....	68
Figure 4.5. Plot of the inverse of the magnetic susceptibility vs the temperature for $\text{Na}_{3-\delta}\text{VOF}_5$ measured with an applied field of 10K Oe. ....	69
Figure 4.6. Normalized K- edge absorption spectra corresponding to cryolite $\text{Na}_{3-\delta}\text{VOF}_5$ (blue), $\text{V}_2\text{O}_5$ (red) and $\text{VO}_2$ (green). The inset depicts superimposed pre- edge features for comparative purposes. ....	70
Figure 4.7. Rietveld refinement of $\text{Na}_{3-\delta}\text{VOF}_5$ considering the existence of sodium vacancies in the structure (above) or full occupation for sodium sites (below). Experimental pattern (red dots), calculated profile (black continuous line) and difference pattern at the bottom (blue). Bragg positions are denoted by vertical bars. ....	73
Figure 4.8. a) SEM images at different magnifications together with b) chemical mapping (EDX) for the as prepared chiolite. ....	75

Figure 4.10. Normalized K- edge absorption spectra corresponding to chiolite $\text{Na}_{5-\delta}\text{V}_3\text{F}_{14}$ (green), $\text{V}_2\text{O}_5$ (blue) and $\text{VO}_2$ (red). The inset depicts superimposed pre- edge features for comparative purposes. ....	77
Figure 4.11. Electron diffraction patterns along the a) [010], b) [0-11] and c) [-110] zone axes. ....	78
Figure 4.12. Rietveld refinement of $\text{Na}_{5-\delta}\text{V}_3\text{F}_{14}$ using (above) synchrotron X- ray diffraction data and (below) neutron diffraction data. Experimental pattern (red dots), calculated profile (black continuous line) and difference pattern at the bottom (blue). Bragg positions are denoted by vertical bars. ....	80
Figure 4.13. Crystal structure of $\text{Na}_{5-\delta}\text{V}_3\text{F}_{14}$ along the c- axis. ....	84
Figure 4.14. Crystal structure of chiolite $\text{Na}_5\text{V}_3\text{O}_3\text{F}_{11}$ . (P1212 space group). ....	88
Figure 4.14. Potential vs capacity profile for a) $\text{NaVF}_4$ , b) $\text{Na}_{3-\delta}\text{VOF}_5$ and $\text{Na}_{5-\delta}\text{V}_3\text{F}_{14}$ tested V at C/25 in 1M $\text{NaClO}_4$ in EC: PC, starting upon oxidation.....	90
Figure 4.15. Potential vs capacity profile for a) $\text{NaVF}_4$ , b) $\text{Na}_{5-\delta}\text{V}_3\text{F}_{14}$ and c) $\text{Na}_{3-\delta}\text{VOF}_5$ cycled upon reduction between OCP to 0.1 V at C/25 in 1M $\text{NaClO}_4$ in EC: PC. ....	91
Figure 5.1. a) SEM image and EDX mapping and b) XRPD pattern corresponding to $\text{Na}_{5-\delta}\text{Ti}_3\text{O}_3\text{F}_{11}$ prepared by a microwave assisted method.....	94
Figure 5.2. Synchrotron XRPD showing the Rietveld refinement of $\text{Na}_{5-\delta}\text{Ti}_3\text{O}_{3-\delta}\text{F}_{11+\delta}$ . The experimental pattern is shown in red dots, the calculated profile in black continuous line and difference pattern at the bottom in blue. Bragg positions are denoted by vertical bars. ....	96
Figure 5.3. Structure of $\text{Na}_{5-\delta}\text{Ti}_3\text{O}_{3-\delta}\text{F}_{11+\delta}$ along c- axis with tentative distribution of O and F as deduced from Pauling's second rule. ....	99
Figure 5.4. Potential vs capacity profile of $\text{Na}_{5-\delta}\text{Ti}_3\text{O}_{3-\delta}\text{F}_{11+\delta}$ cycled vs $\text{Na}^0$ at C/25 in 1 M $\text{NaClO}_4$ in EC: PC.....	100
Figure. 5.5. XRPD pattern of $\text{Na}_2\text{Ti}_3\text{O}_7$ prepared by solid state reaction. Its crystal structure is shown as an inset.....	100



- Figure 5.6. XRPD pattern corresponding to a mixture of  $\text{Na}_2\text{Ti}_3\text{O}_7$  with PDVF in 1:0.5 ratio after thermal treatment at 350 °C under air flow. Peaks corresponding to the identified compounds are denoted with colored vertical bars:  $\text{Na}_2\text{Ti}_3\text{O}_7$  (green, PDF # 31-1329),  $\text{Na}_2\text{Ti}_6\text{O}_{13}$  (pink, PDF# 37-951) and  $\text{Na}_3\text{TiOF}_5$  (blue, PDF# 24-1146). .....102
- Figure 5.9. Potential vs capacity profile at C/15 for electrochemical tests carried out with  $\text{Na}_2\text{Ti}_3\text{O}_7$  using powdered (below) and self- standing (above) electrodes. Plots of the capacity vs. cycle number in for the two electrolyte salts employed are also shown (inset). .....104
- Figure 5.8. XRPD pattern of pristine  $\text{Na}_2\text{Ti}_3\text{O}_7$  (pink) and a self- standing electrode fabricated with  $\text{Na}_2\text{Ti}_3\text{O}_7$  (black). Peak positions and intensities for  $\text{Na}_2\text{Ti}_3\text{O}_7$  (purple, PDF#31-1329) and  $\text{H}_2\text{Ti}_3\text{O}_7$  (orange PDF#47-561)) are shown in the lower part of the graph. ....105
- Figure 5.10. Ti- K edge absorption spectra taken using the *in situ* electrochemical cell for pristine  $\text{Na}_2\text{Ti}_3\text{O}_7$  and fully reduced  $\text{Na}_4\text{Ti}_3\text{O}_7$ . Spectra from reference *r*-  $\text{TiO}_2$  and  $\text{Ti}_2\text{O}_3$  are also shown. ....108
- Figure 5.11. a) Potential vs time profile for  $\text{Na}_2\text{Ti}_3\text{O}_7$  SSE cycled vs  $\text{Na}^\circ$  at C/8. b) 3-D plot showing the evolution of the SXRD patterns collected during electrochemical reduction as a function of time. c) 2-D projection of SXRPD data depicting the changes in intensity and position of the main diffraction peaks as reduction proceeds and sodium intercalation takes place. ....110
- Figure 5.12. a) Potential vs time profile for  $\text{Na}_2\text{Ti}_3\text{O}_7$  SSE tested at C/8 vs  $\text{Na}^\circ$  using an *in situ* cell. Rietveld refinement of the SXRD patterns taken at b) the beginning of reduction ( $\text{H}_2\text{Ti}_3\text{O}_7$ ), c) the end of reduction ( $\text{Na}_4\text{Ti}_3\text{O}_7$ ), d) the end of reoxidation ( $\text{Na}_2\text{Ti}_3\text{O}_7$ ).....111
- Figure 5.13. (Right) SXRD pattern collected at ALBA synchrotron ( $\lambda= 0.602 \text{ \AA}$ ) for SSE after 50 cycles and corresponding cell parameters. The first cycle and the capacity vs. cycle number are also shown (left and center respectively). .....112
- Figure 5.15. a) Calculated entropy variation of Na metal (black squares),  $\text{Na}_2\text{Ti}_3\text{O}_7$  (red dots) and  $\text{Na}_4\text{Ti}_3\text{O}_7$  (green squares) as function of temperature. b) Calculated variation of free energy as function of temperature. ....113

Figure 5.7. Evolution of XRPD patterns of  $\text{Na}_2\text{Ti}_3\text{O}_7$  after 8 months stored in different electrolytes/electrolyte solvents. ....114

## List of Tables

Table 3.1: structural details found by the joint Rietveld refinement of NPD and synchrotron XRPD data. ....	57
Table 3.2. Selected bond lengths and angles resulting from the joint Rietveld refinement of NPD and synchrotron XRPD data. ....	58
Table 4.1. Selected bond distances and angles for Na <sub>3-6</sub> VOF <sub>5</sub> cryolite obtained from Rietveld refinement of SXPDP data.....	74
Table 4.2. Atomic positions determined by Rietveld refinement.....	81
Table 4.3. Selected bond lengths resulting from combined Rietveld refinement of NPD and SXPDP data. ....	82
Table 4.4. Bond distances and Debye- Waller factor determined with EXAFS analysis for the Na <sub>5-8</sub> V <sub>3</sub> F <sub>14</sub> chiolite. ....	83
Table 5.1. Atomic positions determined from Rietveld refinement. Anions (F and O) are commonly denoted as X.....	97
Table 5.2. Selected bond lengths obtained from Rietveld refinement of XRPD data.....	98
Table 5.3. Pre- edge and main – absorption edge energy positions and oxidation states for references Na <sub>2</sub> Ti <sub>3</sub> O <sub>7</sub> and Na <sub>4</sub> Ti <sub>3</sub> O <sub>7</sub> .....	109

## List of chemical products used for the syntheses

**Caution:** hydrofluoric acid is highly corrosive and irritating. Its use requires extreme caution, and it must be handled with protective clothing. Specialized treatment is required in case of contact with liquid or vapor HF.

**Chapter 3: Na-Mn-(Mo)-(O,F) system**

NaMnO <sub>4</sub> · H <sub>2</sub> O.....	40 wt. % in H <sub>2</sub> O Aldrich
NaF.....	≥99%, Sigma- Aldrich
HF.....	48% in H <sub>2</sub> O (≥99.99), Sigma- Aldrich
H <sub>2</sub> O <sub>2</sub> .....	50 % in H <sub>2</sub> O (≥99.99), Sigma- Aldrich
NaHF <sub>2</sub> .....	Granular, 98%, Aldrich
Mn <sub>2</sub> O <sub>3</sub> .....	99.99%, Aldrich
Na <sub>2</sub> MoO <sub>4</sub> · 2H <sub>2</sub> O.....	≥99%, Aldrich
MnF <sub>2</sub> .....	98%, Aldrich
Mn(CH <sub>3</sub> COO) <sub>2</sub> · 4H <sub>2</sub> O.....	≥99%, Aldrich

**Chapter 4: Na-V-(O,F) system**

NaNO <sub>3</sub> .....	analytical standard (Fluka)
V <sub>2</sub> O <sub>5</sub> .....	98%, Aldrich
Ethylene glycol.....	Anhydrous, 99.8%, Sigma- Aldrich
HF.....	48% in H <sub>2</sub> O (≥99.99), Sigma- Aldrich

**Chapter 4: Na-Ti-(O,F) system**

H <sub>2</sub> TiF <sub>6</sub> .....	60 % in H <sub>2</sub> O (≥99.99), Sigma- Aldrich
NaCOOCH <sub>3</sub> .....	≥99%, Aldrich
Anatase TiO <sub>2</sub> .....	powder ( 98%), Aldrich
Na <sub>2</sub> CO <sub>3</sub> .....	anhydrous (99.99%), Aldrich
Polyvinylidene fluoride (PVDF).....	KYNAR
Diethyl ether.....	Anhydrous, 99.0%, Sigma- Aldrich

**Electrochemical tests**

NaClO <sub>4</sub> .....	98%, Aldrich
NaPF <sub>6</sub> .....	98%, Aldrich
Propylene carbonate.....	Anhydrous, 99.7%, Aldrich
Ethylene carbonate.....	Anhydrous, 99.0%, Aldrich
Sodium.....	Cubes (99.9%), Aldrich

# **CHAPTER 1: Introduction**

### 1.1 Relevant crystal structures of (oxy)fluorinated materials

Fluorinated materials have for long attracted the attention of scientists and have become key in many aspects of modern life. They are used in application fields as diverse as nuclear energy, metallurgy, cosmetics, textiles and colour pigments, plastics and domestic ware, catalysis and electronics, amongst many others. Further on, interest on oxyfluorides arose as the physical properties of compounds can be modified through oxygen-fluorine replacement, which is easily enabled due to the similar size of the isoelectronic  $O^{2-}$  and  $F^-$  anions.[1] Such substitution has been reported for structural types as diverse as rutile, perovskite, garnet or pyrochlore;[2] and charge is compensated either by reduction of the metal oxidation state (e.g. for transition metals) or by appropriate cationic balancing through aliovalent substitutions. A striking example of the effect of the oxygen-fluorine exchange is the decrease in the Curie temperature for ferroelectric oxides due to the lower covalency of the M-F bonds.[3] In some cases anionic ordering is achieved as a result of the different coordination tendencies of the cations present in the structure. This is the case for structures like elpasolite- like oxyfluorides containing polar  $[MoO_3F_3]^{3-}$  units.[4,5] Nevertheless, it should be pointed out that ordering of O/F anions is by no means a general trend. Moreover, it is often difficult to detect with routine techniques such as X- ray or neutron diffraction due to the very close ionic radius for both anions and similar scattering factors values.[6]

The crystal structure of metal fluorides is generally governed by geometric and electrostatic principles given the fact that fluorine is the most electronegative element and therefore results in the higher ionic bonds. In most oxidation states for *d* transition metals, radius ratios  $r_M/r_F$  lie in the stability field of octahedral coordination (0.41- 0.73), commonly observed in binary and ternary fluorides. In the following, attention will be focused on ternary and quaternary alkali transition metal fluorides and oxyfluorides, which constitute the topic of this PhD thesis. The  $A_mMF_n$  compounds display differences in their coordination according to the radius ratio  $r_A/r_F$  and  $r_M/r_F$ , which, as mentioned above, mostly results in octahedral coordination of isolate or linked  $[MnF_6]$  units. Cations A influence the arrangement of these units to achieve an optimal  $AF_n$  coordination.[7] The coordination number of the alkali-

metal ions in polynary fluorides is determined by the radius ratio  $r_A/r_F$ , where the larger ions  $K^+, Rb^+, Cs^+$  tends to exhibit 12- coordination, intermediate sized  $Na^+$  compounds generally have 6- to 8- coordination and the smallest cation  $Li^+$  presents 6- to 4- coordination.

In most A-M-F ternary compounds, when the F:M ratio is  $\geq 6$ , isolated octahedral  $[MF_6]$  units are found, as in the case of cryolite structure of general composition  $A_3MF_6$  and the related elpasolite structure ( $A_2BMF_6$ ). The size of the countercation plays an important role in the resulting framework, which is determined by the tolerance factors of the crystal lattice. Indeed,  $A_3MF_6$  cryolite crystallizes with monoclinic symmetry for  $A=Na$ , while in the case of  $A_2BMF_6$  with  $A=K$  and  $B=Na$ , (elpasolite) the symmetry becomes cubic.[8] In this case, the radius of A and B determine the size of the 12- and 6- coordination cavities in the cubic structure, which is favoured when  $r_A \gg r_B$ .

When the F:M ratio is  $<6$ , changes in the connectivity of the  $[MF_6]$  octahedra take place and linked units are observed forming single, double or triple bridges through corner, edge or face sharing of  $[MF_6]$  octahedra.[8] Such connectivity determines the formation of one-, two-, or three dimensional structures. For example, when only forth of the six corners of the octahedra are shared with other octahedra by the edges, layered networks result. The structural types having only corner- shared octahedra can be classified as (i) chain structures of general composition  $A'_2MF_5$  and  $A''MF_5$ , (ii) layer structures as  $A'MF_4$ ,  $A''MF_4$ ,  $A'_2MF_4$  and  $A'_5M_3F_{14}$ ; and (iii) 3D framework structures as the  $AMF_3$  (perovskite),  $A'M''M'''F_6$  or  $A'_2M''M'''F_7$  (weberite). In the following, the most relevant crystal structures that were investigated during the course of this Ph.D. will be described, specifying the structural types where fluorine substitution by oxygen has been reported.

#### **1.1.2. Crystal structures with isolated octahedra: $A_3MF_6$ and $A_2BMF_6$**

$Na_3AlF_6$  is the archetype of the cryolite structure, an aluminum mineral discovered in 1938 by Naray- Szabo *et al.* It crystallizes in the monoclinic crystal system with space group  $P2_1/n$ . Cryolites exhibit an open crystal framework consisting of  $AlF_6$  octahedra placed at the edge of a cubic lattice. Sodium ions surround the  $AlF_6$  units by occupying one- half of the



octahedral sites, which induces a distortion in the unit cell and lowers the lattice symmetry. The cryolite crystal structure is a special case of the elpasolite structure ( $ABB'X_6$ ) ordered perovskite that contains two types of anionic groups ( $BX_6$ ,  $B'X_6$ ) alternated along the 4-fold axes. Therefore, cryolites are described with the general formula  $A_3BB'F_6$  where A and B are chemically equivalent atoms.[9] A scheme of the crystal structure is shown in Figure 1.1.

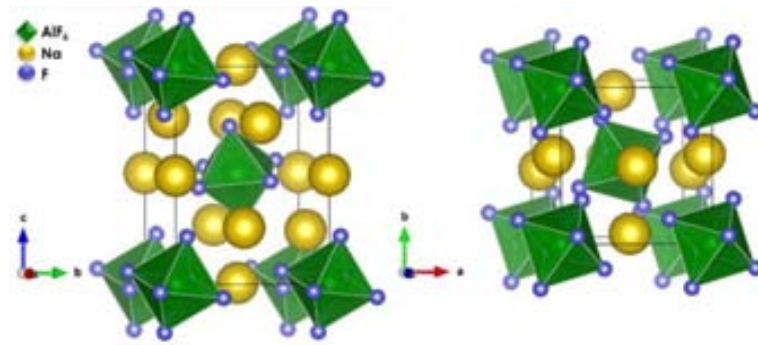


Figure 1.1. Schematic view of the crystal structure of  $\text{Na}_3\text{AlF}_6$  cryolite.

The idealized cubic cryolite structure is only achieved by elpasolites of chemical composition  $\text{K}_2\text{NaAlF}_6$  with sodium ions occupying octahedral sites and potassium ions being placed in 12-coordinated sites.[7]

Among the oxyfluorides presenting cryolite- elpasolite structural type,  $\text{A}_2\text{BMO}_x\text{F}_{6-x}$  with A, B= Na, K,  $\text{NH}_4$ , Rb, Cs and  $\text{M}^{\text{VI}}$ = Mo and W [10,11] have been largely studied for their ferroelectric and ferroelastic properties. The interest in such type of oxyfluorides is motivated by the large distortion exhibited by the  $\text{MO}_x\text{F}_{6-x}$  octahedron for  $x=3$ , which results in polar units that could present macroscopic dipole moments if anionic ordering is achieved. Partial or complete ordering has been observed at a certain temperature ranges  $T_1$ -  $T_2$ [9,12–16] in  $\text{A}_2\text{BMO}_3\text{F}_3$  compounds which results in phase transitions that are accompanied by noticeable dielectric and caloric effects. [17]

### 1.1.3. Chain structures: $\text{A}'_2\text{MF}_5$

Single chains of  $(\text{MnF}_5)_n$  are formed when the F:M ratio is 5 and octahedra are linked by *cis* or *trans*- corner- sharing.  $\text{MF}_5$  octahedra that are connected by *cis*- vertices form infinite

zigzag chains parallel to  $a$ - axis as observed in  $K_2FeF_5$ [18] where bridge angles range from 162 to 173°. Meanwhile, in *trans*- connected chains,  $MF_6$  octahedra are bridged by *trans*-fluorine atoms as in the case of  $Na_2MnF_5$ [19] where  $[MnF_6]$  octahedra are axially elongated due to the Jahn- Teller distortion of  $d^4 Mn^{2+}$  forming infinite chains with bridge F- M- F angles of 132°. The chains are therefore separated by sodium ions that lie between them, as illustrated in Figure 1.2.

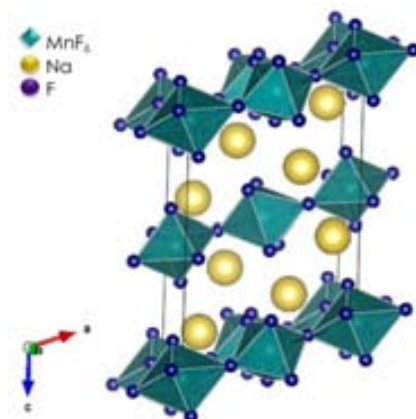


Figure 1.2. Schematic view of the  $Na_2MnF_5$  chain- type structure.

#### 1.1.4. Layered structures

##### 1.1.4.1. Chiolite ( $A_5M_3F_{14}$ )

The chiolite mineral  $Na_5Al_3F_{14}$  was first reported by Brosset [20] in 1938 and fully characterized by Jacobini [21] (1981). Its crystal structure has a tetragonal symmetry with space group  $P4/mnc$ , ( $Z=2$ ) and consists of layers formed by corner- linked octahedra where one of every four octahedra is replaced by a sodium ion. One-third of  $MX_6$  octahedra share four corners with two-thirds of  $MX_6$  octahedra that are rotated 45° with respect to the former. Such layers are stacked along (001) direction and displaced one respect to the other by half the (110) diagonal. 4/5 of the existing sodium ions per formula unit are located between the layers while the remaining one occupies an intralayer position (Figure 1.3).

The chiolite structural type is adopted by a variety of fluorides, oxides and oxyfluorides with general formula  $A_5M_3X_{14}$  and rich diversity in composition (e.g.  $Na_5Fe_2CoF_{14}$ ,  $(NH_4)_5In_3F_{14}$ ,

$\text{Ag}_5\text{W}_3\text{O}_9\text{F}_5$   $\text{SrCa}_4\text{Te}_3\text{O}_{14}$  or  $\text{NaNd}_4\text{Sb}_3\text{O}_{14}$ ). Indeed, phases with M in different oxidation states are formed depending on the nature of the A cations and the O/F ratio. Nonetheless, the majority of studies have focused on  $A = \text{Na}, \text{K}$ ; and  $M = \text{Al}, \text{Ti}, \text{V}, \text{Fe}, \text{Co}, \text{W}$ , [22–26] amongst which  $\text{Na}_5\text{Fe}_3\text{F}_{14}$  and  $\text{Na}_5\text{W}_3\text{O}_9\text{F}_5$  have received most attention because of their ferromagnetic and ferroelectric properties. [27,28]

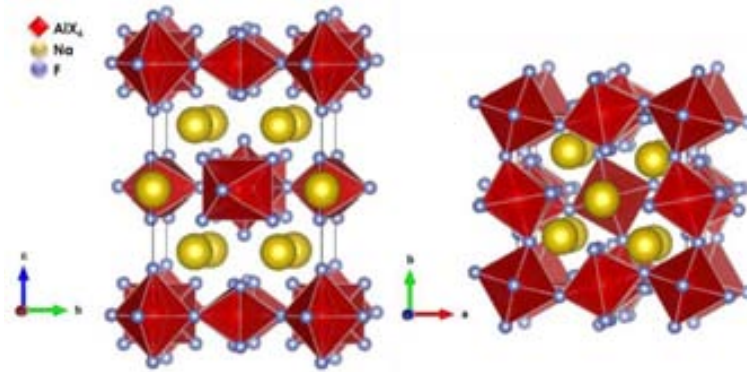


Figure 1.3. Schematic view of the crystal structure of  $\text{Na}_5\text{Al}_3\text{F}_{14}$  chiolite.

### 1.1.5. 3D Framework structures

#### 1.1.5.1. Perovskites

The mineral  $\text{CaTiO}_3$  is the archetype of perovskite structure, discovered in 1839 by Gustave Arose and named after Russian Count Lev Aleksevich von Perovski, it exhibits an orthorhombic structure with space group  $Pnma$ . The ideal cubic  $\text{AMX}_3$  perovskite structure consists of corner-sharing  $\text{MX}_6$  octahedra where A cations are placed at the corners of the cubes with 12- coordination, while M is at the center of the cube and octahedral coordinated to X anions pointing to the cell edges. Perovskites exhibit a large variety of structural modifications, as they can accommodate A and M ions with different sizes and charges. This, together with the possible existence of anionic and cationic vacancies leads to a large structural flexibility and a large variety exists of perovskites with different distortions and related structures.

In the idealized perovskite constructed from rigid spheres, the cell parameter  $a$ - is geometrically related to the ionic radii of the cations and anions through the equation (1)

$a = (2)^{1/2}(R_A + R_X) = 2(R_M + R_X)$  (2), where  $R_A, R_M$  and  $R_X$  are the ionic radii of the cation (A), the transition metal (M) and the anions (X). The ratio between the two equations is known as the Goldschmidt's tolerance factor  $t = (R_A + R_X)/(2)^{1/2} (R_M + R_X)$ , which allows estimating the degree of distortion of the crystal lattice from the cubic perovskite. Cubic perovskite has a tolerance factor range of  $0.89 < t < 1$ , where the ideal ternary oxide perovskite  $\text{SrTiO}_3$  has  $t = 1$ , with  $R_A = 1.44 \text{ \AA}$ ,  $R_M = 0.605 \text{ \AA}$  and  $R_X = 1.40 \text{ \AA}$  (Figure 1.4). When  $t$  is larger than 1 (large A ion or small M ion), the crystal structure exhibits hexagonal symmetry. In contrast, if  $t < 1$ , the  $\text{MO}_6$  octahedra tilt to maintain the coordination of the A ion, and induces a lowering in symmetry crystal lattice. This is the case of sodium containing fluoroperovskites ( $\text{NaMF}_3$ ,  $M = \text{Fe, Mn, Ni, Zn}$ ), which, with the exception of  $\text{NaCuF}_3$ , all exhibit orthorhombic symmetry with  $Pnma$  ( $n^\circ 62$ ) space group.

A very large number of oxides have been reported exhibiting perovskite or perovskite related structures.[29] Fluoride and oxyfluoride perovskites are less abundant. In recent years, the  $\text{Sr}_2\text{CuO}_2\text{F}_{2+\delta}$  phase has attracted increasing attention due to its superconducting properties ( $T_c = 46 \text{ K}$ ).[30] Perovskites with general formula  $\text{AMO}_2\text{F}$  such as  $\text{KTiO}_2\text{F}$  or the series of  $\text{ANbO}_2\text{F}$  with  $A = \text{Li, Na and K}$  have also been investigated due to their interesting magnetic and electric properties.  $\text{ANbO}_2\text{F}$  compounds showed temperature- independent paramagnetism when the susceptibility was extrapolated to infinite fields and were found to be semiconductors ( $10^{-6} - 10^{-7} \Omega^{-1} \text{ cm}^{-1}$ ).

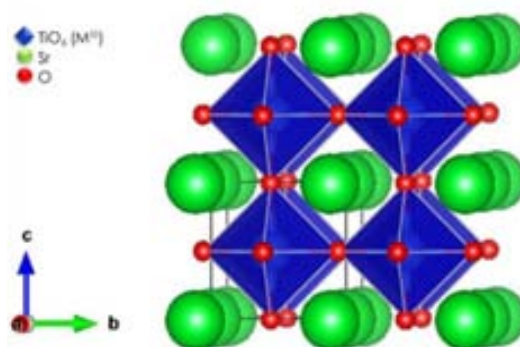


Figure 1.4. Schematic view of the crystal structure of the cubic  $\text{SrTiO}_3$  perovskite.

## 1.2. Common synthetic methods to obtain (oxy)fluorinated compounds

Traditionally, fluorine containing compounds have been prepared via solid state reactions in sealed containers. This method is still widely used as it enables full control over the product stoichiometry preventing hydrolysis of reactants or products. For instance,  $\text{Na}_5\text{Fe}_3\text{F}_{14}$ [25] and  $\text{Na}_{5-x}\text{A}_x\text{W}_3\text{O}_9\text{F}_5$  are prepared at temperatures ranging from 650-700°C and 500 to 700 °C respectively, in gold sealed tubes. Other oxyfluorides as  $\text{KTiO}_2\text{F}$  and  $\text{ANbO}_2\text{F}$  (A= Li, Na, K) have been prepared by direct mixing of KF and the corresponding  $\text{MO}_2$  oxide.[31,32] Also,  $\text{Fe}_2\text{OF}_4$  has been prepared under air flow at 430 °C using as  $\text{FeF}_2 \cdot \text{H}_2\text{O}$  and  $\text{FeF}_2$  as starting materials.[33] Although the solid state route allows preparing a wide variety of compounds with controlled composition, it generally requires intermediate grinding and long thermal treatments in order to achieve pure compounds. Such protocols mostly lead to thermodynamic control of the reactions. Kinetic control can be more easily achieved in mild conditions where phases are obtained at low temperature and in liquid media.

Innovative synthetic routes have been increasingly used in recent years in order to prepare new fluorinated materials under mild- conditions where composition and particle size can be mastered by controlling the reaction medium temperature, pressure, composition, acidity, etc. Microwave- assisted synthesis does also represent a good alternative method due to its unconventional heating mode (microwave radiation), which can bring advantages in terms of time, energy efficiency and cost. [34–37] When a dielectric material such as water is exposed to microwave radiation, microwave energy is absorbed by the material and heat is generated,[38] allowing syntheses to be carried out in short periods of time and often yielding nanoparticles. As an example, non-stoichiometric hydronium titanium oxyfluoride has been prepared pure in only 3 minutes.[39] Also, monodisperse  $\text{MgF}_2$  nanoparticles have been obtained from a solution of  $\text{Mg}(\text{NO}_3)_2$  and  $\text{NH}_4\text{F}$  heated in a domestic microwave oven.[40] Combined synthetic methods have also allowed the preparation of fluorides. Cubic  $\text{KMf}_3$  (M= Zn, Co, Mn, Fe)[41] nanoparticles have been achieved by microwave initiated hydrothermal synthesis while  $\text{FeF}_3$  nanoparticles were obtained by microwave- assisted fluorolytic sol- gel route. [42]

Another synthetic method that also deserves increased attention is the mechanochemical synthesis of inorganic compounds. This method is generally solvent-free and is carried out by successive grinding/milling processes and even sonication. The main drawback is the difficulty in achieving pure phases.[43] Recently, a series of pure and crystalline  $\text{NaMF}_3$  (M = Mn, Fe, Co, Ni, Cu) fluoroperovskites were prepared by ball-milling (750 rpm for 5h) from a stoichiometric mixture of NaF and  $\text{MF}_2$ [44,45] and  $\text{KMF}_3$  (M = Mg, Ca, Mn, Fe, Co, Ni, and Zn) were prepared from  $\text{MF}_2$  and KF by grinding in a planetary ball-mill.[46,47] Some oxyfluorides have also been prepared by mechanochemical synthesis (e.g. LaOF). [48]

Finally, the synthesis of fluorides and oxyfluorides by co-precipitation from aqueous solutions at low temperature (below 100 °C) has also been reported. For example,  $\beta$ -  $\text{Li}_3\text{VF}_6$  was precipitated from an aqueous solution containing stoichiometric amounts of  $\text{VCl}_3$ , HF and  $\text{Li}_2\text{CO}_3$  by addition of 2-propanol at 0- 60 °C.[49] Similarly,  $\alpha$ -  $\text{Li}_3\text{FeF}_6$  has been obtained from aqueous solution of  $\text{Fe}(\text{NO}_3)_3 \cdot 9\text{H}_2\text{O}$ , HF and  $\text{Li}_2\text{CO}_3$  at 50- 60 °C.[50] Also, titanium oxyfluorides  $\text{NH}_4\text{TiOF}_3$  and  $(\text{H}_3\text{O})_{2/3}\text{TiO}_{4/3}\text{F}_2$  have been obtained from aqueous solutions containing  $(\text{NH}_4)_2\text{TiF}_6$  or  $\text{H}_2\text{TiF}_6$ , respectively, and  $\text{H}_3\text{BO}_3$  as F<sup>-</sup> scavenger.[51,52] When considering synthesis in aqueous media at temperatures higher than 100 °C, hydro- and solvothermal methods provide a wider range of experimental conditions (temperature and pressure),[53] which usually entail a single-step synthetic procedure and enable the preparation of samples with controlled particle size.[54] High solvation power, high compressibility, and mass transport properties of a selected solvent or mineralizer at controlled temperature allows the preparation of finely divided materials and microcrystallites with well-defined size and morphology for specific applications.[53] Lightfoot *et al.*[55–57] have extensively studied the synthesis of alkali transition metal fluorides and oxyfluorides via solvothermal synthesis. As an example, they reported the preparation of the chiolite-type  $\text{K}_5\text{In}_3\text{F}_{14}$  or  $\text{Na}_4\text{V}_2\text{O}_2\text{F}_8$ , which were prepared starting from  $\text{K}_2\text{CO}_3$ ,  $\text{InNO}_3$  and  $\text{NaNO}_3$ ,  $\text{V}_2\text{O}_5$ , respectively, dissolved in a mixture of HF and ethylene glycol at 100 °C. Also, the series of (oxy)fluorides  $\text{K}_2\text{TiF}_6$ ,  $\text{K}_2\text{TiOF}_4$ ,  $\text{K}_3\text{TiOF}_5$  and  $\text{K}_7\text{Ti}_4\text{O}_4\text{F}_7$  has been prepared by using diverse alkali and metal

precursors and different solvents such as  $\text{CH}_3\text{OH}$ ,  $\text{H}_2\text{O}$  and  $\text{H}_2\text{O}_2$ , in different molar ratios. [58] There are also examples of alkali metal fluorides such as the  $\text{Na}_3\text{VF}_6$  cryolite and the  $\text{KMgF}_3$ , prepared by hydrothermal synthesis using binary metal fluorides as precursors. [59]

In view of its wider versatility, such methods were selected to be used in the course of this PhD to attempt the syntheses of phases in the Na-M-O,F (M= V, Mn, Ti) systems. Such compounds were expected to exhibit crystal structures suitable for the reversible deinsertion- insertion of sodium atoms and hence be suitable for use as positive electrode materials in sodium-ion batteries.

### **1.3. Introduction to battery basics**

Among the diversity of energy storage systems, batteries are most versatile. A battery is an electrochemical device composed of several electrochemical cells connected in series or parallel, although it is commonly referred to a single electrochemical cell. It consists of two electrodes separated by an electrolyte which is an ion conducting material but is itself an electrical insulator.[60] The spontaneous electrochemical reactions that generate electricity take place at the electrodes and are driven by the difference in electrochemical potential between them.[61] During discharge, a battery is connected to an external circuit through which electrons flow spontaneously from the negative electrode to the positive electrode, leading to the respective oxidation and reduction of each respective active material. Meanwhile, electroneutrality is maintained by the flow of positively charged species contained in the electrolyte (e.g.  $\text{Li}^+$  or  $\text{Na}^+$ ) from the cathode to the anode. When one of the electrode materials is consumed, the electron flow stops. If the process can be reversed by an external current, the battery is rechargeable and is termed secondary battery, while the batteries that cannot be efficiently recharged are usually called primary batteries. [62,63] Figure 1.6 schematically illustrates the operating principle of a typical sodium-ion battery, with the positive and negative electrodes being constituted by a layered compound (e.g.  $\text{NaMO}_2$ ) and disordered carbon respectively. The electrolyte usually

consists of a sodium salt (e.g.  $\text{NaClO}_4$  or  $\text{NaPF}_6$ ) dissolved in organic solvents (such as propylene carbonate (PC), or ethylene carbonate (EC), amongst others). [64,65]

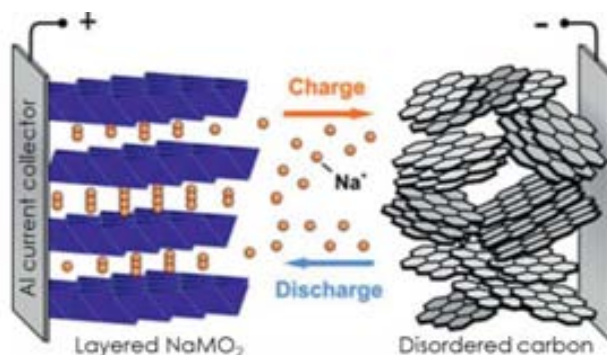


Figure 1.6. Schematic of an operating Na- ion battery. Modified from reference [66].

The cell potential open circuit potential ( $V_{oc}$ ) is determined by the difference between the electrochemical potential of the electrodes while the electrochemical stability window is determined by the energy separation of the lowest unoccupied molecular orbital (LUMO) and the highest occupied molecular orbital (HOMO) of the electrolyte (see Figure 1.7). Electrolyte solvents commonly used are unstable below ca. 1.0 V vs  $\text{Na}^+/\text{Na}$  and above ca. 4.5 V vs  $\text{Na}^+/\text{Na}$  in presence of the electrode materials, which are reducing/oxidizing agents.[67] Degradation reactions often involve the electrolyte salt and result in the generation of a solid passivation layer at the surface of the electrodes formed with insoluble products of degradation. Such layers formed on the negative electrode are usually termed Solid Electrolyte Interphase, SEI and have been widely studied as they allows successful operation of the electrolytes outside their thermodynamic stability window.[68] An interphase is also formed at the surface of the positive electrode, sometimes called Surface Layer (SL) which remains less studied and understood.



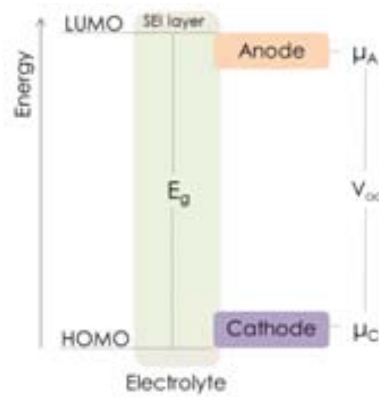


Figure 1.7. Scheme depicting electrode electrochemical potentials vs potential window of the electrolyte (adapted from reference[69]). The open-circuit voltage ( $V_{oc}$ ) is determined by the difference between the electrochemical potential of the electrodes ( $\mu_A - \mu_C$ ).

The energy density of a battery depends on its electrochemical capacity and operation potential. The capacity of each electrode material ( $C$ ) depends on the number of electrons exchanged ( $n$ ) per formula unit ( $M_w$ ) and is expressed as  $C$  (mAh/g) =  $nF/M_w \cdot 3.6$ , where  $F$  is the Faraday constant.

### 1.3.1. Sodium ion batteries

To date, Li-ion battery (LIB) technology dominates the portable electronic market and is increasingly considered to power the next generation of electric vehicles. The prospects of wider scale application (e.g. grid) and concerns regarding the uneven distribution of lithium raw materials in the Earth's crust and most importantly, the supply risk that can be derived from their geopolitical constraints has prompted the study of analogue battery technologies based on other charge carrying ions such as Na-ion batteries (SIB).

Sodium is one of the most abundant elements in Earth crust[70] and the second lightest and smallest alkali metal (after lithium). Its intercalation chemistry is similar to that of lithium, and thus implementation of knowledge gained in the development on Li-ion batteries is expected to foster the development of the SIB. [71] While a penalty in energy density would be derived from the substitution of lithium metal electrodes by sodium metal, the trend does

not hold when comparing LIB and SIB. Indeed, in that case, the energy density is determined by the operation potential and electrochemical capacity of electrode materials and there is no reason why similar performance cannot be expected. The larger radius of sodium ions prompts at different preferred coordination environments which has implications in the stability of certain polymorphs, as the case of maricite and olivine. However, the larger size does not necessarily involve larger diffusion barriers as deduced from recent computational studies, indicating that Na-ion systems can be competitive Li-ion analogues. [72] Sodium metal has been used for long in liquid state in high temperature Na-S and ZEBRA batteries[73,74]. The study of intercalation compounds such as NaCoO<sub>2</sub> [75] was mainly carried out in the 80's, in parallel to that of the lithium analogues, but mostly abandoned in the 90's with commercialization of LIBs.

Recent resurgence of research focused on the achievement of a SIB analogue to LIB and operating at room temperature has prompted the re-investigation of known and new electrode materials, especially those with layered and framework structures suitable for intercalation of sodium ions.[66,71,76–78] The following sections summarize the most significant results achieved.

### **1.3.2. Positive electrodes**

Following analogies with the LIB technology, polyanionic frameworks (e.g. phosphates) are interesting electrode materials due to the strong covalent bonding in (PO<sub>4</sub>)<sup>n-</sup> units, which results in high structural and thermal stability.[79] NASICON- type compounds such as Na<sub>3</sub>Ti<sub>2</sub>(PO<sub>4</sub>)<sub>3</sub> or Na<sub>3</sub>V<sub>2</sub>(PO<sub>4</sub>)<sub>3</sub> have been shown to exhibit interesting behavior but moderate performance either in terms of potential or capacity. Na<sub>3</sub>V<sub>2</sub>(PO<sub>4</sub>)<sub>2</sub>F<sub>3</sub> [80,81] is especially interesting as it exhibits high potential ( V<sup>3+</sup>/ V<sup>4+</sup> redox couple) which is enhanced by the presence of highly electronegative fluoride ions in the structure. It yields a reversible capacity of 110 mAh/g along two plateaus at 3.7 and 4.2 V vs Na<sup>+</sup>/Na with, which is the highest operating voltage amongst the practical positive electrode materials for SIB reported to date.

Layered transition metal oxides  $\text{NaMO}_2$ , analogous to  $\text{LiMO}_2$  used in commercial lithium ion batteries have also been widely studied for SIB.[75,82] Phases containing diverse metals and polymorphs with different coordination for the sodium (octahedral (O) or prismatic (P)) have been largely studied as the case of O3- and P2-  $\text{Na}_x\text{MO}_2$  with  $M=\text{Mn, Fe and Co}$ .[83–87] Polyanionic materials have also received attention, with fluorine containing phases such as  $\text{Na}_3\text{V}_2\text{O}_{2x}(\text{PO}_4)_2\text{F}_{3-2x}$  ( $0 \leq x \leq 1$ )[80,88,89] deserving currently great attention in view of their interesting performance (average operation potential close to 4 V vs.  $\text{Na}^+/\text{Na}$ , and overall reversible capacity around 100 mAh/g, stable upon cycling.

Some reports have also appeared in the course of this PhD on the test of composite electrodes containing transition metal fluorides such as  $\text{MF}_3$  ( $M= \text{Co, Fe, Ti}$ ) in sodium cells.  $\text{FeF}_3$  ball milled with carbon for 24 h with exhibited an average reduction potential of 2.2V with a reversible capacity of  $100\text{mAhg}^{-1}$  Recent reports by Okada *et al.* [90–92] dealing with  $\text{NaMF}_3$  with  $M= \text{Mn, Fe, Co, Ni}$  seem to indicate that the only  $\text{NaFeF}_3$  is electrochemically active towards sodium intercalation exhibiting a reversible capacity of  $197 \text{mAh g}^{-1}$  when tested between 1.5 and 4.5 V vs  $\text{Na}^0$  in 1M  $\text{NaClO}_4$  in EC: DMC.[90] Finally, following reports of electrochemical of  $\text{Li}_3\text{FeF}_6$  cryolite in lithium cells,[93] isostructural  $\text{Na}_3\text{FeF}_6$  was tested in sodium cells and found to exhibit a reversible capacity of 110 mAh/g on the 1<sup>st</sup> cycle. *Ex situ* XRPD measurements pointed to a conversion reaction mechanism with the electrochemical profile exhibiting high polarization and low cycleability, which was attributed to the insulating character of fluorides.[94]

### 1.3.3. Negative electrodes

While graphite is the most common negative electrode material in lithium-ion cells, it does not intercalate any sodium [95–99] However, other carbonaceous materials do react with sodium ions to some extent [65,100,101]. the best performance is exhibited by hard carbon, which can be considered the current standard negative electrode for SIBs and reacts with sodium at low potential exhibiting ca. 300 mAh/g reversible capacity and good cycleability.[99]

Negative electrode materials with a redox mechanism based on alloying reactions has also been considered despite the expected large volumetric expansion. [102] Successful results have been achieved using both tin [103] and antimony as electrode materials, the former exhibiting a reversible capacity of 500 mAh/g between 0.0 and 0.7 V vs Na<sup>0</sup> after 20 cycles. Interestingly, antimony was found to exhibit better electrochemical performance in sodium based than in lithium based cells, which has been attributed to the redox mechanism involving the formation of different phases. [104]

The research of intercalation compounds for negative electrode applications is limited to compounds containing early transition metals (titanium and vanadium), as conversion reactions are observed for the rest. Amongst these, early studies on layered sodium titanate Na<sub>x</sub>TiO<sub>2</sub> (containing Ti<sup>+3</sup>) showed reversible Na<sup>+</sup> intercalation of 0.3mol of Na<sup>+</sup> at 1 V vs Na<sup>+</sup>/Na with concomitant oxidation to Ti<sup>+4</sup>. [105] Our group has recently shown that Na<sub>2</sub>Ti<sub>3</sub>O<sub>7</sub> exhibits reversible intercalation of 2 mol of sodium ions (ca. 177mAh/g) at a surprisingly low average potential (0.3 V vs Na<sup>+</sup>/Na) concomitant to the reduction of 2/3 of Ti<sup>+4</sup> to Ti<sup>+3</sup>. [106,107] The electrochemical activity is related to a two- phase redox process that has been confirmed by preliminar *in situ* X-ray diffraction measurements and involves the formation of a phase with Na<sub>4</sub>Ti<sub>3</sub>O<sub>7</sub> stoichiometry, which could not be fully characterized. Unfortunately the capacity retention of this compound has been poor to date in spite of efforts to modify morphology and particle size or use different electrode technologies [108–112] and thus, further efforts to understand this phenomenon are a must if this material is ever to be considered for practical application.

#### **1.4. Motivation of the study**

The initial objective of the present PhD thesis entailed a prospective study of transition metal fluorides and oxyfluorides as possible electrode materials for sodium ion cells. The advantages of fluorinated phases stem from the higher electronegativity of the M-F bond that leads to higher ionicity and hence higher redox potentials when used as electrode materials, while their drawbacks are usually related to their highly insulating character.

The target compounds prepared during this Thesis contain early transition metals with different possible oxidation states, namely Mn, V and Ti. Chapters 3 and 4 are devoted to the synthesis, structural characterization and electrochemical testing for the manganese and vanadium containing phases. Chapter 5 is devoted to phases containing titanium which may be used as negative electrode materials. The study involves mainly oxyfluorides, but also  $\text{Na}_2\text{Ti}_3\text{O}_7$  for which unsuccessful attempts to introduce fluorine (and create sodium vacancies in the structure) were carried out. Such results prompted us to pursue research a more detailed characterization of the redox mechanism of  $\text{Na}_2\text{Ti}_3\text{O}_7$  to get further insight on the origin of the severe capacity fading observed.

## **CHAPTER 2: Experimental procedures**

*Synthesis and chemical analysis*

*Electron, neutron and X-ray diffraction*

*Spectroscopic techniques*

*Magnetism*

*Electrochemistry*



## 2.1 Synthesis and compositional characterization of materials

### 2.1.1. Synthetic routes

During the development of this work, different synthetic routes were considered in the attempt to prepare sodium transition metal oxyfluorides having crystal frameworks attractive for Na<sup>+</sup> electrochemical intercalation. Most of the samples prepared were precipitated from aqueous solutions in concentrated hydrofluoric acid contained in polypropylene or PTFE beaker of 150- 250 ml. Reactions were carried out in a temperature range of 25 to 80 °C under constant stirring during 6 to 12 h.

Inspired from the work reported by Aldous et al[113], solvothermal synthesis was also considered to prepare new vanadium compounds. The syntheses were carried out in Teflon vessels where precursors were dissolved in hydrofluoric acid and ethylene glycol and subsequently placed in autoclaves tightly closed. Reaction temperatures and times ranged from 100 to 220 °C and 6 to 24 h.

Additionally, microwave- assisted synthesis was attempted to precipitate new sodium titanium oxyfluorides. The syntheses were carried out in a domestic microwave oven (LG Intellowave, 2.45GHz) at 800W power, where the solutions were heated for 15 s. Such procedure was repeated 5-10 times with cooling periods of 1- 3 minutes.

Solid state syntheses were also considered to prepare different sodium metal transition oxyfluorides and Na<sub>2</sub>Ti<sub>3</sub>O<sub>7</sub>. The latter was initially prepared by reaction of *anatase* TiO<sub>2</sub> and Na<sub>2</sub>CO<sub>3</sub> at 800 °C for 40h in a tubular furnace under air. Different attempts were made to introduce fluorine in the structure including starting from precursors containing fluorine or use of fluorinating agents such as polyvinylidene fluoride (PVDF). Such reactions were carried out in tubular furnaces under N<sub>2</sub> or synthetic air or flow and different thermal treatments but unfortunately all of them were unsuccessful.

The list of precursors used for each synthesis is described in Appendix and the detailed synthetic procedures for each specific compound will be described in the corresponding Chapter.



### 2.1.2. Chemical Analysis

Samples for chemical analysis were prepared by digestion (ca. 40 mg) with HNO<sub>3</sub>, HF and H<sub>2</sub>O<sub>2</sub> in a high- pressure Teflon reactor and heated at 220 °C with a microwave Milestone Ethos Plus. The resulting dissolution was brought to level (50 ml). The content of vanadium, titanium, manganese and molybdenum in the samples prepared was determined through inductively coupled plasma optical emission spectrometry (ICP-OES) using a multichannel spectrophotometer Perkin- Elmer Optima 3200 RL. Determination of sodium content was carried out with inductively coupled plasma mass spectrometry (ICP-MS) using a Perkin Elmer ELAN 6000 spectrometer in standard conditions. The analyses were carried out at the Unit of Metal Analysis- University of Barcelona and results are expressed % wt/wt, where 1% corresponds to 1000ppm.

### 2.1.3. Magnetic measurements

Magnetic susceptibility measurements were carried out to estimate the oxidation state of vanadium and manganese in the samples. These were done on a SQUID Quantum Design magnetometer between 10 K to 350 K with an applied field of 100 Oe and 5000 Oe for the samples containing manganese or vanadium, respectively.

Unpaired electrons in a magnetic field across a range of temperatures can align randomly at a given temperature, which corresponds to a paramagnetic behavior. When the alignment of the spins is parallel, the structure presents a ferromagnetic behavior while antiparallel alignment describes an anti- ferromagnetic behavior. Ferromagnetic and anti-ferromagnetic samples present transitions at a critical temperature denoted Curie or Néel temperature, respectively. Above the critical point, the samples are paramagnetic and can be ascribed to have a Curie or Curie- Weiss behavior, where the magnetic susceptibility is inversely proportional to the temperature. The comparison of the effective magnetic moment obtained from measurements with the theoretical one (eq. 1), allows the estimation of the oxidation state of transition metal in the sample measured. Experimentally, effective magnetic moment ( $\mu_{\text{eff}}$ ) can be determined from the Curie- Weiss law (eq. 2-3),

which is valid when linearity is achieved from plotting the inverse of magnetic susceptibility ( $\chi^{-1}$ ) as function of temperature.

$$\mu_{eff,t} = 2\sqrt{S(S+1)}\mu \quad \text{eq. 1}$$

$$\frac{1}{\chi_m} = \frac{T+\theta}{C} = \frac{1}{C}T + \frac{\theta}{C} \quad \text{eq. 2}$$

$$\mu_{eff} = \sqrt{\frac{3kC}{N}} = 2.84\sqrt{C} \quad \text{eq. 3}$$

N: Avogadro's number

k: Boltzmann constant

#### 2.1.4. Scanning Electron Microscopy (SEM)

Morphology and particle size of the samples prepared during this work were examined using a field-emission gun scanning electron microscope (Quanta 200 ESEM FEG FEI).

As part of the characterization protocol used during this thesis, Energy- dispersive X- ray spectroscopy (EDX) analyses have been performed to get a rough estimation of the O/F ratio and Na and M contents (M= Mn, Mo, V, Ti). This technique makes use of the characteristic X- rays emitted by the sample when irradiated with a focused electron beam. This yields a consisting of Gaussian-shaped peaks observed at wavelengths (energies) that are characteristic for each element present in the sample which enables semi-quantitative analysis. [114]

#### 2.1.5. Attenuated total reflection infrared (ATR-IR)

IR spectra (500-4000  $\text{cm}^{-1}$ ) were collected using a Perkin Elmer FT- IR Spectrum One system with a Universal Attenuated Transmission Reflectance (ATR) accessory and a DiComp™

crystal composed of a diamond ATR crystal with a ZnSe focusing element. ATR mode consists in measuring the changes in the evanescent wave produced when the infrared

beam is directed onto an ATR crystal with high refractive index in a given angle. The sample must be in good contact with the ATR crystal to allow the evanescent wave to extend to the surface and therefore observe the attenuated wave. Identification of the main bands presents on the spectra was carried out by comparison with literature.

## **2.2. Structural characterization techniques**

### **2.2.1. X-ray diffraction (XRD)**

The products obtained from syntheses and various treatments performed during this work were monitored primarily with X-ray powder diffraction (XRPD). Such technique allows the identification of the phases formed and the possible impurities obtained. The acquisition of routine XRPD patterns was done using a Siemens D-5000 diffractometer (Cu-K $\alpha$  radiation) in the range  $2\theta = 5-80^\circ$  with a  $2\theta$  step size of  $0.02^\circ$ .

For the mixed phase  $\text{NaMnMoO}_3\text{F}_3 \cdot \text{H}_2\text{O}$ , two different sample holders were used for XRPD measurements: a standard one in which the material is pressed from the top to get a flat surface; and a second one that is side loaded.

Some of the phases prepared have also been characterized by synchrotron X-ray diffraction (SXPDP). High-resolution SXPDP patterns for  $\text{NaMnMoO}_3\text{F}_3 \cdot \text{H}_2\text{O}$  were collected at the 11-BM beamline ( $\lambda = 0.413548 \text{ \AA}$ ) of the Advanced Photon Source (Argonne National Lab, mail-in program) using 0.5 mm diameter borosilicate capillaries which were rotated during data collection.  $\text{Na}_{3-6}\text{VOF}_5$ ,  $\text{Na}_{5-8}\text{V}_3\text{F}_{14}$ ,  $\text{Na}_5\text{Ti}_3\text{O}_3\text{F}_{11}$  and  $\text{NaMnOF}_2 \cdot x\text{H}_2\text{O}$  were measured at the Material Science and Powder Diffraction (MSPD) beamline at ALBA synchrotron. The SXPDP of  $\text{Na}_{3-6}\text{VOF}_5$  was collected in a capillary of 0.5 mm and  $\lambda = 0.70855 \text{ \AA}$  employing a MYTHEN (microstrip system for time-resolved experiments) and a MAD26 (multicrystal analyser detector) detectors.  $\text{Na}_{5-8}\text{V}_3\text{F}_{14}$ ,  $\text{Na}_5\text{Ti}_3\text{O}_3\text{F}_{11}$  and the oxyfluoride  $\text{NaMnOF}_2 \cdot x\text{H}_2\text{O}$ , synchrotron

X-ray diffraction patterns were also collected at MSPD beamline. The samples were measured in capillaries of 0.5 mm with a  $\lambda = 0.61988 \text{ \AA}$  and using a MAD detector.

Phase identification from XRPD patterns was carried out using the data base files JCPDS Powder Diffraction File (PDF) and computer programs DRXWin and Creafit.[115]

Refinements of the crystal structure of the phases prepared were performed with the Rietveld method using FullProf\_suite program.[116]

Single crystal XRD was carried out using an Enraf-Nonius CAD4 diffractometer producing graphite monochromated MoK $\alpha$  radiation ( $\lambda = 0.71073 \text{ \AA}$ ). The crystal was mounted at the tip of a glass fibre. After the random search of 25 reflections indexation was carried out. Intensity data were collected in the  $\omega$ - $2\theta$  scan mode and corrected for Lorenz and polarization effects. Solving structure factor phases was performed with SIR2004 [3], and the full matrix refinement with SHELXL97 [4].

### **2.2.2. Neutron powder diffraction (NPD)**

Unlike X-rays, neutrons can strongly interact with light elements; therefore, a combined analysis of neutron and X-ray diffraction patterns allows a better estimation of the bond distances. Neutron powder diffraction (NPD) patterns of  $\text{NaMnMoO}_3\text{F}_3 \cdot \text{H}_2\text{O}$ ,  $\text{Na}_5\text{V}_3\text{O}_3\text{F}_{11}$  and  $\text{NaMnOF}_2 \cdot x\text{H}_2\text{O}$  samples were collected at room temperature and measured at D2B beamline of Institut Laue Langevin (Grenoble, France, EASY access system) in high flux mode ( $\lambda = 1.594 \text{ \AA}$ ) and Debye Scherrer geometry using ca. 2 g of sample placed inside a ~8 mm diameter vanadium sample-holder.

DICVOL,[117] DAJUST, [118] XLENS,[119] and FullProf\_suite[116] programs were used for indexing the patterns, intensity extraction, resolution of the structure and structure elucidation/refinement respectively.

### 2.2.3. Pauling's second rule: anion distribution in crystals

Distribution of oxygen and fluorine in a crystal structure is difficult to determine with neutron and X-ray diffraction techniques because of their similar scattering lengths of the two anions. Different quantitative approaches as the bond valence method have been developed to determine the position of the anions, but they require a previous knowledge of the crystal coordinates. A qualitative and simpler way to do so consists of Pauling's second crystal rule (PSCR). It has proven to be a valid approach to predict the distribution of anions by considering the coordination number ( $v_i$ ) and formal oxidation state ( $Z_i$ ) of each cation bonded to a given anion in the crystal structure. Bond length sum derived from PSCR is expressed as described in eq. 4:

$$b = \sum_i \frac{Z_i}{v_i} \quad \text{eq.4}$$

Pauling's second crystal rule has been used during this work to propose a plausible O/F distribution in the oxyfluorides prepared as a complement to bond valence sum methods.

### 2.2.4. Selected area electron diffraction (SAED)

Selected Area Electron diffraction studies were performed using a JEOL 1210 transmission electron microscope operating at 120 kV and equipped with a Gatan sample holder allowing  $\pm 60^\circ$  x and  $\pm 30^\circ$  y tilting. Preparation of the samples involved dispersing the powder in heptane (anhydrous, 99%) and depositing a droplet of the dispersion on a holey carbon coated copper grid.

SAED allowed the determination cell parameters and space groups by means of the reconstruction of the reciprocal space through the rotation method. This method consists in rotating the microcrystal around one of the crystallographic axes to identify the planes contained in the angular range evaluated. This allows obtaining 2D projection of the reciprocal space perpendicular to the rotation axis. After rotating around different crystal axis and subsequent indexation of the reflections, cell parameters can be measured directly

from the patterns and systematic extinctions elucidated and hence possible space groups determined.

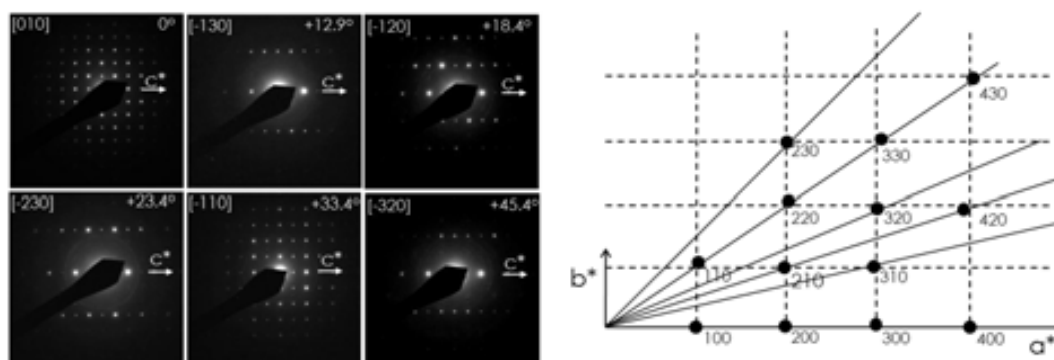


Figure 2.1. ED patterns taken during rotation along a specific crystal axis (left) and the corresponding 2D projection and diffraction spot indexation (right).

## 2.2.5. X-ray absorption

### 2.2.5.1. K- edge of vanadium compounds

K-edge XANES and EXAFS spectra of  $\text{Na}_5\text{V}_3\text{O}_3\text{F}_{11}$  and  $\text{Na}_{3-x}\text{VOF}_5$  were measured in transmission mode at B18 beamline- Diamond synchrotron (Oxfordshire, UK) using a Si(111) double- crystal monochromator of energy resolution  $1.4 \times 10^{-4}$  on pellets containing 5 mg of the sample mixed with 100 mg of cellulose and pressed to 3 Tm.

K-edge XANES spectra of the samples were merged and normalized following standard procedures. Oxidation state of the samples measured was estimated by determining  $E_0$  from the mid- height of the absorption edge and subsequent linear regression from the absorption energy of the references. EXAFS data analysis was performed using the program Artemis[120].

### 2.2.5.2. In situ X-ray absorption experiment

*In situ* XANES and EXAFS measurements at Ti K- edge were carried out at SAMBA beamline at Soleil synchrotron (France). The measurements were carried out in transmission mode using a Si(111) monochromator and gas- filled ion chambers. For the measurements, an *in*

*situ* electrochemical cell was used (described further on in Section 2.3.4.1) during galvanostatic reduction of  $\text{Na}_{2+x}\text{Ti}_3\text{O}_7$ . XAS spectra were recorded on the pristine sample and after full electrochemical reduction. In each case, three spectra were recorded for 5 min of acquisition time every 40 minutes. Titanium K- edge references for  $\text{Ti}^{4+}$  and  $\text{Ti}^{3+}$  used where rutile  $\text{TiO}_2$  and  $\text{Ti}_2\text{O}_3$ . Data analysis was done using *Athena* and *Artemis* software[120].

## 2.3. Electrochemical characterization

### 2.3.1. General setup

Electrochemical tests were carried out in two electrode Swagelok cells (Figure 2.2). The body of the cell and internal pieces are made of stainless steel except for the working electrode plunger made of aluminum. Plungers were covered with Teflon tape to avoid electrical contact with the body cell and with nylon joints allowed to keep the cell hermetic. Sodium cubes slices were used as counter electrode and two Whattman (GF/D) microfiber disks soaked with the electrolyte were used as separator.

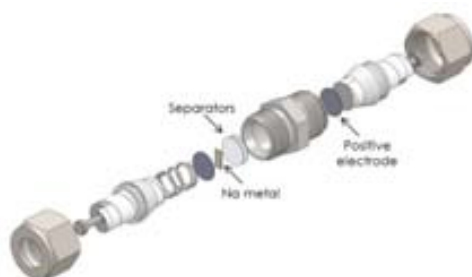


Figure 2.2. Scheme of the Swagelok cell used to perform the electrochemical tests.

The electrolyte selected for preliminary tests was 1M in  $\text{NaClO}_4$  in a 1:1 mixture of ethylene carbonate (EC) and propylene carbonate (PC). Electrochemical tests were in galvanostatic mode were performed using two electrode Swagelok cells with Na as counter electrode. Cyclic voltammetry experiments were carried out at a scanning rate of  $5 \text{ mVs}^{-1}$  using three-electrode Swagelok cells with sodium metal reference electrodes. Aluminum plungers were also used in such experiments to probe a wide potential window and in order to avoid alloying of Na with lead plungers ( $\text{Na}_{15}\text{Pb}_4$ ). Some additional CV experiments were carried

out using 1 M NaClO<sub>4</sub> in a mixture (1:1) of ethyl methanesulfonate (EMS) and PC given the wider stability window of such electrolytes reported (ca. 5.5 V vs Li<sup>+</sup>/Li) [121,122] Figure 2.3 depicts the 5<sup>th</sup> cycle voltammograms for both electrolytes used where oxidation current for EC:PC electrolyte is observed at lower potentials while behavior upon reduction is roughly similar

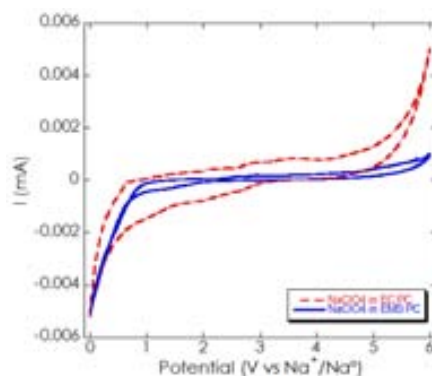


Figure 2.3. Fifth cycle voltammograms for the electrolytes 1 M NaClO<sub>4</sub> in EC:PC and 1 M NaClO<sub>4</sub> in EMS:PC

### 2.3.2. Electrode preparation

In order to get a first indication of the electrochemical activity of the compounds, electrodes consisting of a simple mixture of the material to be tested with carbon were investigated. Working electrodes were prepared by ball-milling the (oxy)fluorides synthesized with 40 % of SP carbon (TIMCAL) to increase the electronic conductivity and contained typically 3-5 mg of active material. Different ball-milling time periods were used, depending on the sample, generally, 05 to 12h. Standard ball-milling conditions were: 350 rpm and intermediate resting periods of 5 minutes every 30 minutes, to avoid overheating of the powder. XRPD patterns were taken after every ball-milling step to ascertain any possible degradation caused by the milling treatment.

For the electrochemical study of Na<sub>2</sub>Ti<sub>3</sub>O<sub>7</sub>, electrodes were prepared using the Bellcore [123] technology from an acetone based slurry containing 70% of NTO, 20 % SP carbon, 10 % of polyvinylidene fluoride (PVDF) and dibutyl phthalate (DBP) as plasticizer. The mixture is stirred for 24 h and casted over a glass surface using the Doctor Blade technique. After drying self-



standing films are peeled off and 1 cm<sup>2</sup> electrode disks cut and washed with diethyl ether to eliminate the plasticizer and enhance porosity of the electrode.

### 2.3.3. Galvanostatic method

Most of the electrochemical studies in the present work were carried out in galvanostatic mode. It consists of applying a constant current and measuring the dependence of the potential during subsequent oxidation (Na<sup>+</sup> deinsertion) and reduction cycles (Na<sup>+</sup> reinsertion) as function on time ( $t$ ) or the amount of charge that passes through the cell. Such experiments were performed using either a McPile (Bio-logic) or an ARBIN potentiostat at different rates, expressed as  $C/n$ , where  $n$  is the number of hours needed to intercalate one mol of Na ions and  $C$  is the specific capacity of the material expressed in mAh/g.[124] usually ranging from  $C/25$  or  $C/10$  at room temperature, unless the opposite noted.

In order to facilitate the interpretation of the electrochemical tests carried out along this work, blank experiments were carried out with working electrodes containing only SP carbon in different potential windows. About 4-5 mg of SP carbon powder was cycled vs Na<sup>0</sup> in 1 M NaClO<sub>4</sub> in EC: PC at  $C/25$ . Figure 2.4 shows the electrochemical curve of SP carbon ball- milled for 12 h between 4.8 and 1.0 V vs. Na<sup>+</sup>/Na starting upon oxidation. A redox process is observed above 4 V with an associated capacity of ca. 70 mAh/g. Although an increase in capacity is achieved after the first four cycles, subsequent fading of the capacity is observed and which is stabilized at 50 mAh/g after ten cycles. Interestingly, great reversibility is observed, as is illustrated in the capacity vs number of cycle profile.

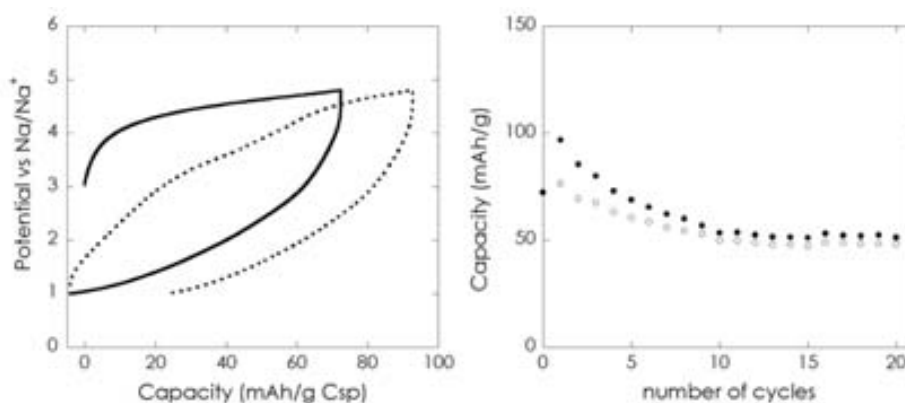


Figure 2.4. (Left) Potential vs capacity profile corresponding to the SP carbon blank experiment carried out between 4.8 and 1.0 V in 1 M NaClO<sub>4</sub> in EC: PC at C/25. (Right) Plot showing the evolution of the electrochemical capacity with cycle number for the blank experiment.

An additional blank experiment carried out towards reduction from the open circuit potential (OCV) to 0.1 V vs Na<sup>+</sup>/Na. A first pseudoplateau is observed at 0.5 V followed by a sloping region. The capacity associated with the first feature is ca. 80 mAh/g, while the total capacity observed is close to 120 mAh/g is achieved. Limited reversibility is observed (ca. 20 mAh/g upon first reoxidation)

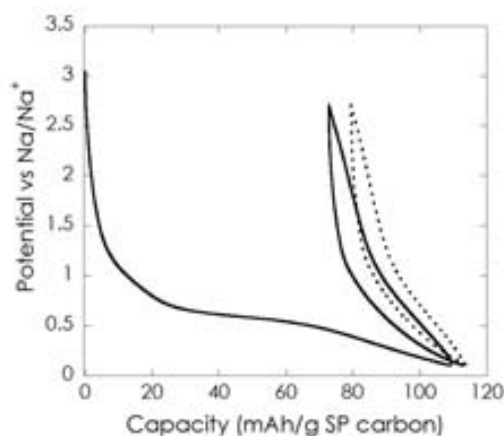


Figure 2.5. Potential vs capacity profile corresponding to the SP carbon blank experiment carried out between OCV and 0.1 V in 1 M NaClO<sub>4</sub> in EC: PC at C/25.3.4. In situ experiments

#### 2.3.4.1. In situ X-ray diffraction experiment

*In situ* X-ray diffraction measurements were carried out using a specifically designed electrochemical cell consisting of a stainless steel body with beryllium windows that allows performing experiments in transmission geometry, as illustrated in Figure 2.6.[125] The battery was cycled off-beam and placed under beam once full reduction was reached, in order to record the evolution of XRPD pattern of the material upon electrochemical Na<sup>+</sup> intercalation/deintercalation into/from the material framework.. XRPD patterns were collected in a 2 $\theta$  range of 15°-55°.



Figure 2.6. Electrochemical cell used for *in situ* X-ray diffraction measurements constituted by three main parts. A) Stainless steel plunger with a Be on the top where Na metal is placed. B) Body of the cell covered with a Mylar to isolate it from the plunger. C) Counter electrode current collector with Be window, where the active material to test is placed in contact with the separator.

Also, *In operando* synchrotron X- ray diffraction experiments were carried out at Beamline MSPD at ALBA synchrotron (wavelength  $\lambda = 0.61988 \text{ \AA}$ ) using the same electrochemical cell described above. The galvanostatic cycling was monitored with a VMP3 potentiostat (Bio-Logic). Synchrotron X- ray diffraction patterns (3 min) were collected every 10 min. During the measurements, the sample cell was continuously rotating  $\pm 20$  degrees to improve statistics.

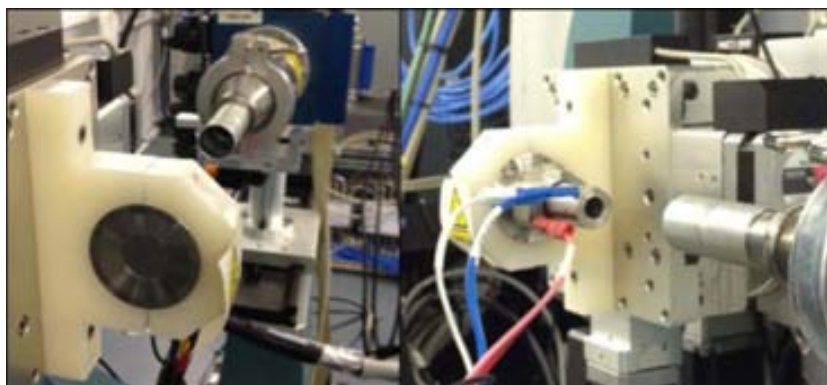


Figure 2.7. Experimental set up for the *in operando* of synchrotron X- ray diffraction experiment.

SXRPD patterns were recorded at different stages of the electrochemical cycling of  $\text{Na}_2\text{Ti}_3\text{O}_7$  and on electrodes with different electrochemical history. An as made electrode was cycled at C/8 from the open circuit potential to the end of reduction and the beginning of sodium plating (in an attempt to ensure completion of reduction). A second electrode previously cycled for full reduction/oxidation cycle in a laboratory two electrode Swagelok cell was also measured in *operando* mode under the same conditions for comparison purposes. Finally, a SXRPD pattern of an electrode after fifty cycles was also collected to try to detect any structural modification in the material induced upon cycling.

# **CHAPTER 3:**

## **Study of the Na-Mn-(Mo)-(O,F) system**

*Synthesis,*

*Characterization,*

*Electrochemical testing of:*

*NaMnF<sub>3</sub>, Na<sub>2</sub>MnF<sub>5</sub>, NaMnOF<sub>2</sub> · xH<sub>2</sub>O, NaMnMoO<sub>3</sub>F<sub>3</sub> · H<sub>2</sub>O*

### 3.1. Synthesis of sodium manganese fluorides.

The fluoroperovskite  $\text{NaMnF}_3$  was precipitated from an aqueous solution at room temperature. Solutions of 3.016 g of  $\text{NaMnO}_4 \cdot \text{H}_2\text{O}$  ( $2 \times 10^{-2}$  mol, ca. 0.8M) and 0.840 g of NaF ( $2 \times 10^{-2}$  mol, ca. 0.8M) were prepared separately and next mixed together with  $0.08 \times 10^{-2}$  mol of HF. The final purple solution was kept under stirring as  $\text{H}_2\text{O}_2$  was added, and resulted in the precipitation of a light pink solid concomitant to discoloration of the solution.  $\text{H}_2\text{O}_2$  addition was stopped when the solution became colorless (ca. 10 ml added). The light pink solid obtained was separated by centrifugation, washed with water /ethanol and dried in air at 70 °C.

Two similar procedures were carried out to prepare  $\text{Na}_2\text{MnF}_5$ . (Route A) 1.5081 g of  $\text{NaMnO}_4 \cdot \text{H}_2\text{O}$  ( $1.0 \times 10^{-2}$  mol) and 0.4377 g of  $\text{NaHF}_2$  ( $7.0 \times 10^{-3}$  mol) were separately dissolved in water and further mixed with 0.3 mL of HF (48 %wt.). Slow addition of 15 mL of ethanol to the solution induced the instantaneous precipitation of a pink solid together with the decrease in the intensity of the characteristic purple color of  $\text{MnO}_4^-$  ion. Once the solution was colorless, the solid was recovered, washed with ethanol and dried in air at 70°C.

The second synthetic procedure used was based on a previous report.[126] (Route B) 0.806 g of  $\text{Mn}_2\text{O}_3$  ( $10 \times 10^{-3}$  mol of Mn) and 0.855 g of NaF ( $20.0 \times 10^{-3}$  mol) were mixed to 10 mL of 0.2 mol of HF (40% wt). Initially, the mixture was stirred vigorously to favor the dissolution of the precursors. Afterwards, the solution was stirred mildly for 6h at room temperature, and a pink solid was gradually observed to precipitate. The solid was repeatedly washed with ethanol and dried in air at 70°C.

## 3.2. NaMnF<sub>3</sub>

### 3.2.1. Chemical analysis and microstructural characterization

Typical SEM images illustrate that the sample is constituted of agglomerates of particles with pseudocubic morphology and average particle size of 8  $\mu\text{m}$ . (see Figure 3.1).

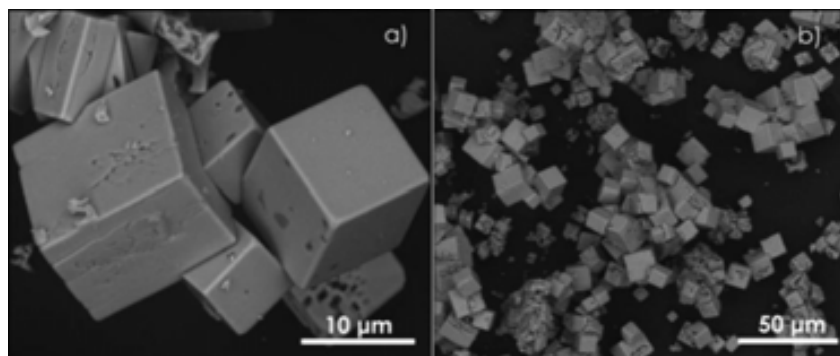


Figure 3.1. SEM images at different magnifications for NaMnF<sub>3</sub>

The presence of adsorbed or crystallization water in the sample was dismissed by infrared measurements. Indeed, the IR spectrum of the as-prepared sample does not exhibit any band in the 1000- 3800  $\text{cm}^{-1}$  range were stretching and bending vibrations of H<sub>2</sub>O nor H<sub>3</sub>O<sup>+</sup> would appear if such species were present in the sample.

The X-ray diffraction pattern corresponds to the orthorhombic perovskite NaMnF<sub>3</sub> of space group *Pnma* (*n*<sup>o</sup> 62) and refined cell parameters are  $a = 5.7458(5) \text{ \AA}$ ,  $b = 7.9982(6) \text{ \AA}$  and  $c = 5.5486(5) \text{ \AA}$ . Small amounts of MnF<sub>2</sub> (ICSD: 24-727) are present as an impurity (see Figure 3.2).

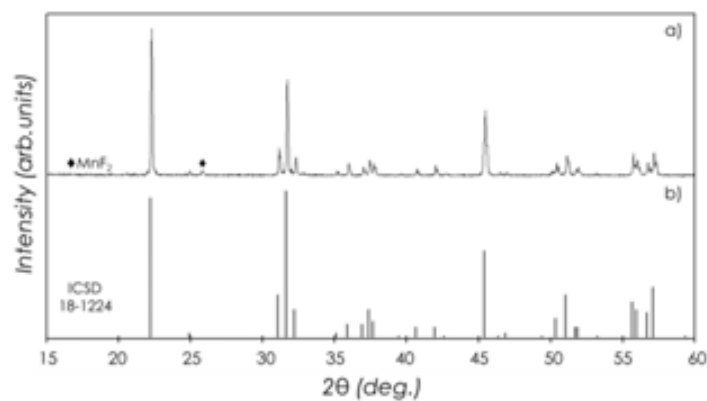


Figure 3.2. XRPD pattern of NaMnF<sub>3</sub> precipitated from a basic aqueous solution. (◆) denotes a peak corresponding to a small amount of MnF<sub>2</sub> impurity present in the sample ( $2\theta = 25.8^\circ$ ).

The oxidation state of manganese was confirmed by magnetic measurements. Figure 3.3 shows the inverse of the susceptibility measured from 5 to 350 K with an applied field of 100 Oe. Antiferromagnetic interactions are present with a  $T_N = 66$  K, in agreement with previous observations.[127,128] Above 100 K, a Curie-Weiss law can be well-fitted resulting and a paramagnetic effective moment of  $5.9 \mu_B/\text{Mn}$  can be calculated which is fully consistent with the presence of Mn (II) in the compound.

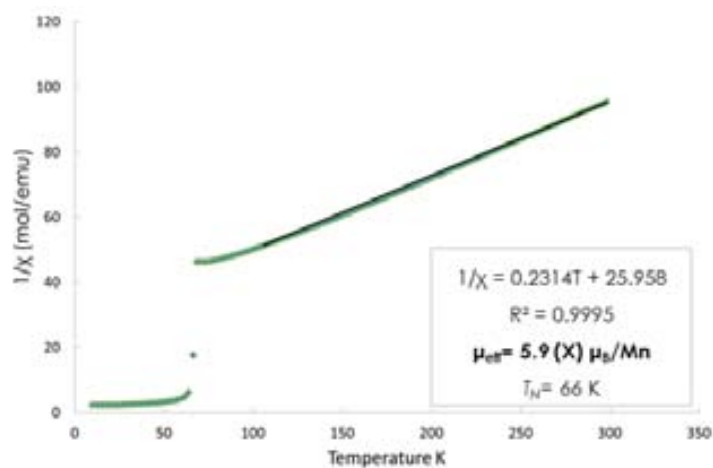


Figure 3.3. Inverse susceptibility vs temperature of NaMnF<sub>3</sub> measured with an applied field of 100 Oe. Observed Neél temperature  $T_N = 66$  K.



### 3.3. Na<sub>2</sub>MnF<sub>5</sub>

#### 3.3.1. Chemical analysis and microstructural characterization

The morphology of the Na<sub>2</sub>MnF<sub>5</sub> particles obtained from synthetic routes A and B can be inferred from SEM micrographs, as depicted in Figure 3.4. While particle size is similar (ca. 10 μm), some differences in morphology are observed: those prepared by Route A exhibit a plate-like shape while prismatic particles were obtained as manganese precursor (Route B). The difference in the aspect ratio Na<sub>2</sub>MnF<sub>5</sub> may be attributed to the use of water and ethanol/ water solvents in the synthesis. The effect of water-alcohol solvents in the crystal growth and morphology has been largely studied.[129–133] The use of alcohols such as methanol, ethanol, 2- propanol and glycols modify the properties of the reaction medium (dielectric constant, interionic attraction, solubility) which have an influence in the crystal growth habit and lead to different crystal shapes and in some cases even to different polymorphs.[134,135]

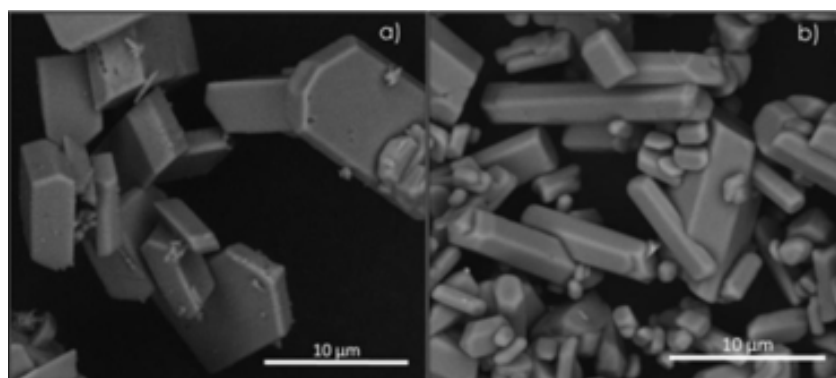


Figure 3.4. SEM images of Na<sub>2</sub>MnF<sub>5</sub> micrometric particles obtained from: a) NaMnO<sub>4</sub> in ethanol/water and b) Mn<sub>2</sub>O<sub>3</sub> in water.

The absence of adsorbed or crystallization water molecules was confirmed for both reaction products by infrared measurements, as no absorption bands were detected from 3600 to 1500cm<sup>-1</sup>, range, where H<sub>2</sub>O or H<sub>3</sub>O<sup>+</sup> bands are expected

The XRPD patterns of the samples prepared through both methods are consistent with pure Na<sub>2</sub>MnF<sub>5</sub> (ICSD 78-331). It crystallizes in a monoclinic symmetry in the space group P12<sub>1</sub>/c1

(n° 14) with cell parameters  $a = 7.7227(6) \text{ \AA}$ ,  $b = 5.2425(5) \text{ \AA}$  and  $c = 10.8719(3) \text{ \AA}$  with  $\beta = 109.00^\circ$ . Significant differences in the relative intensity of the peaks are illustrated in Figure 3.5 indicating preferential orientation effects. The indexing of the pattern evidences that reflection (002) exhibits enhanced intensity in the compound prepared with route A, in agreement with the plate-like morphology of the crystallites.

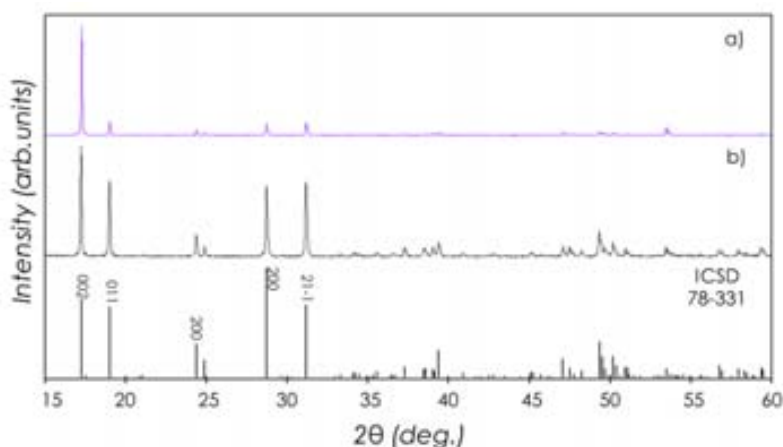


Figure 3.5. XRPD pattern of  $\text{Na}_2\text{MnF}_5$  obtained from aqueous solutions using as manganese precursors: a)  $\text{NaMnO}_4$  (route A) and b)  $\text{Mn}_2\text{O}_3$  (Route B).

Chemical analysis for  $\text{Na}_2\text{MnF}_5$  (Route A) yielded 21.3 ( $\sigma=0.03$ ) and 27.9 ( $\sigma=0.02$ ) as weight % for sodium and manganese, respectively, while Route B yielded 20.4 ( $\sigma=0.22$ ) for sodium and 28.4 ( $\sigma=0.26$ ) for manganese, which are both consistent with the expected values (23.83% Na and 26.95% Mn).

Magnetization of the sample is presented in Figure 3.6. Below  $T_N = 13 \text{ K}$ , this compound presents an antiferromagnetic order, in agreement with previous reports[136]. The Curie-Weiss law fit for the data above 100K allows to calculate an effective paramagnetic of  $5.0 \mu_B/\text{Mn ion}$ , which is in good agreement with the value expected for  $\text{Mn}^{3+}$  ( $4.9 \mu_B/\text{Mn}$ ).

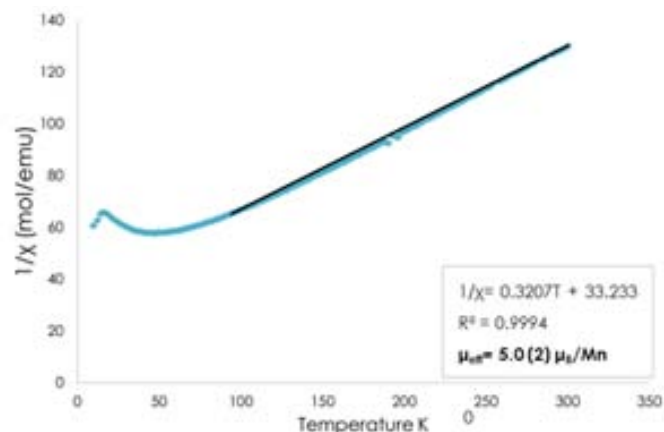


Figure 3.6. Plot of the inverse of susceptibility vs, temperature for Na<sub>2</sub>MnF<sub>5</sub> obtained with an applied field of 100 Oe.

### 3.4. Electrochemical characterization

The feasibility of reversibly de-inserting and re-inserting sodium ions in NaMnF<sub>3</sub> and Na<sub>2</sub>MnF<sub>5</sub> electrochemically was assessed using sodium metal counter electrodes as described in Section 2.3.

#### 3.4.1. Electrode preparation

NaMnF<sub>3</sub> and Na<sub>2</sub>MnF<sub>5</sub> were independently ball-milled with 40% of SP carbon for different time periods at 350 rpm in a planetary ball-mill. XRPD patterns of the milled mixtures were taken in order to detect any possible modification of the electrode materials themselves. In the case of the perovskite, ball-milling does seem to induce neither decomposition nor structural changes, as deduced from the similarity of the corresponding XRPD patterns of mixtures ball-milled for different periods of time between 0.5 and 12h (see Figure 3.7b). However, an increase in peak width with milling time is observed, most likely related to an enhancement in strain and decrease in size for particles. SEM images show that after 2 hours of ball-milling particles size is comparable to that of the pristine sample (ca. 6  $\mu\text{m}$ ) but further

ball-milling up to 12 hours leads to a decrease in particle size to ca.  $0.3\ \mu\text{m}$  and formation of agglomerates of ca.  $13\ \mu\text{m}$  (Figure 3.7a).

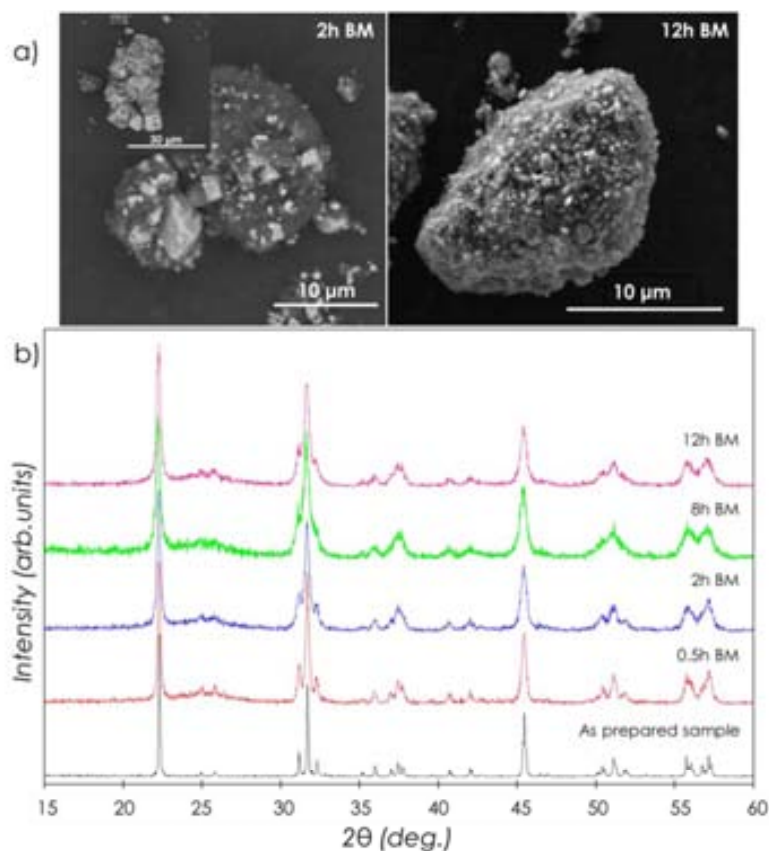


Figure 3.7. a) Typical SEM images corresponding to NaMnF<sub>3</sub> ball-milled for 2 and 12 hours with 40% SP carbon. b) XRPD patterns for mixtures of NaMnF<sub>3</sub> and 40% SP carbon ball-milled for different periods of time (0.5h to 12h) at 350 rpm.

In contrast, in the case of Na<sub>2</sub>MnF<sub>5</sub>, the ball milling induces changes in relative intensities of the peaks even after only 30 minutes, and decomposition of the pentafluoride into perovskite NaMnF<sub>3</sub> is clearly evident after 1 hour of ball-milling, as observed in the corresponding XRPD patterns shown in Figure 3.8. Thus, for this compound, mixtures were simply hand milled for 15 min, which is much less energetic and does not seem to induce any significant modification of the sample, as deduced from the XRPD pattern.

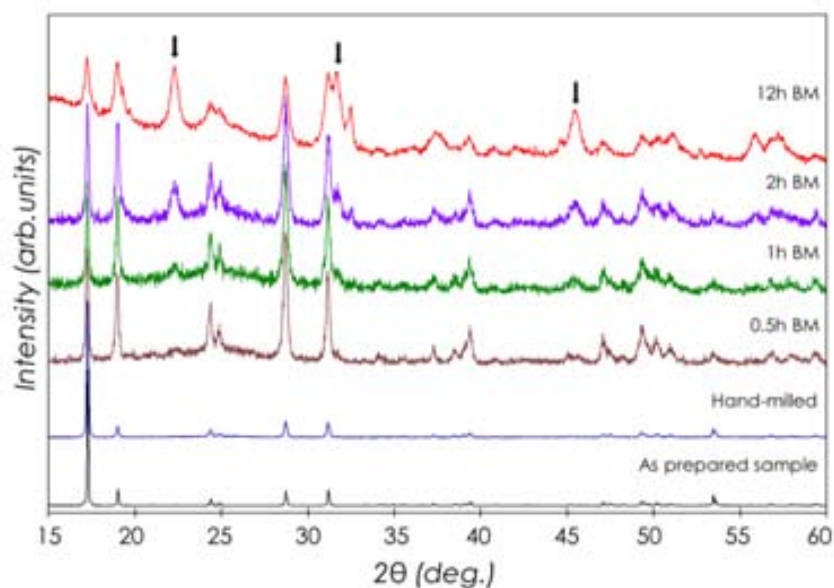


Figure 3.8. XRPD patterns of  $\text{Na}_2\text{MnF}_5$  as prepared and after mixing with 40% of SP carbon by 15 min hand milling (HM) or ball-milling (BM) for different periods of time (0.5 to 12h) at 350 rpm.

Based on these results, the  $\text{Na}_2\text{MnF}_5$  samples HM and 0.5 BM, and the  $\text{NaMnF}_3$  sample ball milled for 12h were selected to perform the electrochemical tests.

### 3.4.2. Electrochemical testing

Electrochemical experiments using sodium metal counter electrodes were carried out at C/25 rate. The electrode containing  $\text{NaMnF}_3$  ball milled for 12 h was tested in the potential window between 1- 4.5V starting upon oxidation (i.e. attempting to remove sodium ions from the structure). Electrochemical activity is only observed above 4V, with a capacity of 165 mAh/g. Upon reversing the sign of the current, a reversible capacity of 128 mAh/g is achieved upon reduction with very large cell polarization (see Figure 3.9). While the latter can be attributed to the highly insulating character of fluorides, [44] the former may be an indication that electrolyte oxidation is the main redox phenomenon taking place instead of sodium removal from  $\text{NaMnF}_3$ . Further cycles resulted in a capacity fading of approximately 10% after 5 cycles. (Chapter 2, Figure 2.4).

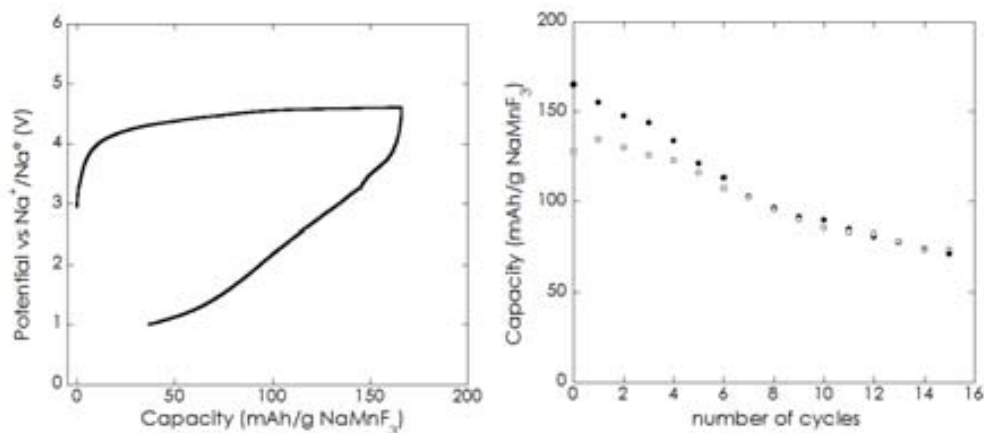


Figure 3.9. a) Electrochemical curve of  $\text{NaMnF}_3$  mixed with 40% SP carbon cycled vs  $\text{Na}^+$ . b) Variation of the capacity as function of the number of cycles. Charge capacity is shown in full circles, discharge capacity in hollow ones.

Electrodes containing  $\text{Na}_2\text{MnF}_5$  were also tested using sodium metal counter electrodes at C/25. The electrochemical profiles observed (see Figure 3.10a) are similar to that described above for  $\text{NaMnF}_3$ . Since electrochemical activity for this compound, if any, was expected at very high potentials where significant decomposition of the electrolyte is expected,  $\text{Na}_2\text{MnF}_5$  ball-milled for 0.5h was electrochemically tested by setting a limitation in the number of electrons transferred to  $x=0.5$  and  $0.8$  (68.5 and 109.6 mAh/g, respectively), as a potential cut off to inverse the sense of the current was considered less appropriate. Figure 3.11 depicts first oxidation-reduction cycle for both experiments along with evolution of the capacity upon reduction for 20 cycles. For the electrochemical cell limited  $x=0.8$ , the average capacity obtained upon reduction was 103 mAh/g, which represents 75% of the total theoretical capacity of the fluoride (137 mAh/g) considering full oxidation of  $\text{Mn}^{3+}$  to  $\text{Mn}^{4+}$ , while the one limited at  $x=0.5$  displayed an average capacity of 58 mAh/g (42% of the expected).

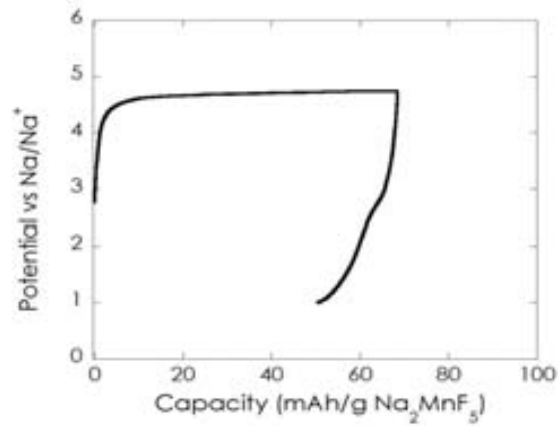


Figure 3.10. Potential vs. capacity profile for  $\text{Na}_2\text{MnF}_5$  (hand- milled) tested at C/25 in 1 M  $\text{NaClO}_4$  in EC: PC.

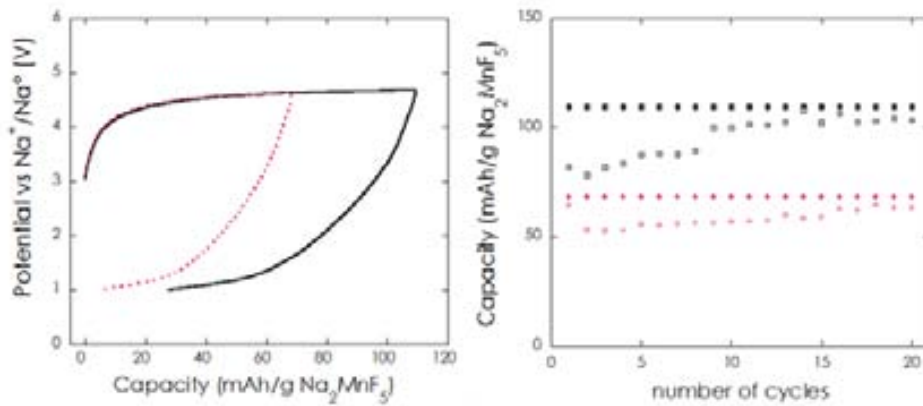


Figure 3.11. a) Potential vs. capacity profile for  $\text{Na}_2\text{MnF}_5$  (0.5 h ball- milled) cycled at C/25 with electron transfer in each half oxidation-reduction cycle limited to  $x=0.5$  (pink dotted line) and  $x=0.8$  (black continuous line). b) Capacity achieved upon oxidation (full symbol) and reduction (hollow symbol) as function of the number of cycles for the experiments with oxidation limited to  $x=0.5$  (pink circles) and  $x=0.8$  (black square).

Additional electrochemical tests were carried out using 1 M  $\text{NaClO}_4$  in EMS: PC as electrolyte,[121] which seems to exhibit larger resilience to oxidation, as described in Section 2.3. However, the change in the electrolyte did not induce any significant changes in the electrochemical profile for any of the two  $\text{NaMnF}_3$  and  $\text{Na}_2\text{MnF}_5$  compounds when compared to those obtained when using 1 M  $\text{NaClO}_4$  in EC: PC.

In order to confirm or dismiss the electrochemical activity of these sodium metal fluorides, *in situ* XRPD measurements were performed at the end of oxidation and compared to those of pristine electrode materials at the cell open circuit potential (see Results corresponding to  $\text{Na}_2\text{MnF}_5$  in Figure 3.11). No changes in the relative intensities or positions of the peaks are evident in the patterns, which confirm that electrochemical de-insertion/re-insertion of sodium is not possible for any of the compounds investigated.

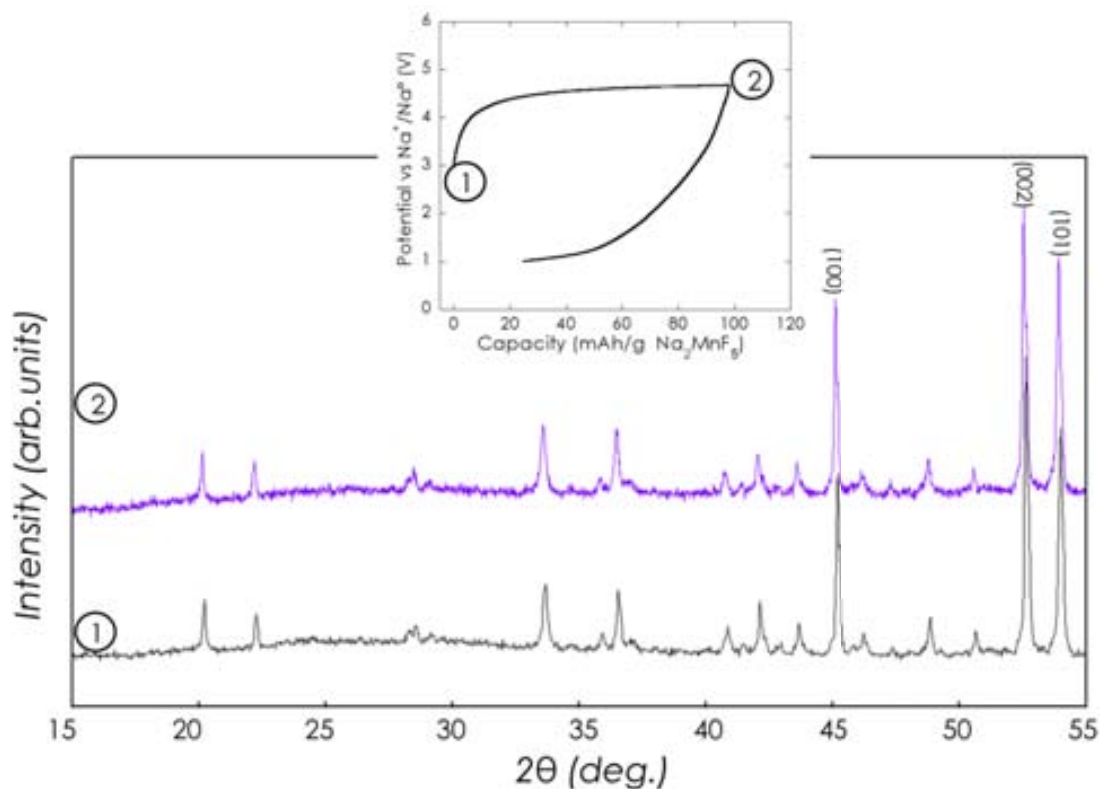


Figure 3.12. XRPD patterns taken *in situ* and corresponding to electrodes containing  $\text{Na}_2\text{MnF}_5$  at open circuit potential (1) and after full oxidation (2). Indexed diffraction peaks correspond to Be metal used in the electrochemical cell. (see Section 2.3)

Such results are in agreement with the most recent work by Okada and coworkers, developed in parallel to the last part of this Thesis. They studied the series  $\text{NaMF}_3$  with  $M = \text{Mn}, \text{Co}$  and  $\text{Ni}$  and did also perform blank experiments with electrodes containing only carbon black. The electrochemical profiles were the same in all experiments and corresponded well both in shape and capacity achieved to that of the blank tests. Thus, they concluded that



none of such compounds did exhibit electrochemical activity in the potential window investigated (from 1.5 to 4.5 vs.  $\text{Na}^+/\text{Na}$ ) in 1M  $\text{NaPF}_6$  in EC: DMC, which was attributed to the strong oxidizing character which would be exhibited by  $\text{MF}_3$  phases with ( $M=\text{Co}, \text{Mn}, \text{Ni}$ ). [92] In our case the electrochemical capacities observed upon first oxidation, translate to values higher than that observed in blank experiments carried out with electrodes containing only SP carbon (see section 2.3.3) but the shape of the electrochemical curve (long endless plateau with very limited reversibility upon reduction) makes us think that the electrochemical activity observed is related to electrolyte oxidation. We presume that such oxidation would take place at a lower potential than in the case of the blank experiment as a result of the catalytic activity of the transition metal containing active materials.

In light of these observations, the feasibility of Na extraction from  $\text{NaMnF}_3$  and  $\text{Na}_2\text{MnF}_5$  was also investigated by first principles methods. Calculations were done within the GGA+U framework using the crystallographic models for phases  $\text{NaMnF}_3$  and  $\text{Na}_2\text{MnF}_5$  that were constructed starting from crystal data previously reported.[137,138] The intercalation potential of the two sodium manganese fluorides were calculated allowing the relaxation of atomic positions, cell parameters, and cell volume, while keeping the symmetry of the initial phase. In the case of  $\text{Na}_2\text{MnF}_5$ , deinsertion of 1 Na ion with concomitant oxidation of  $\text{Mn}^{3+}$  to  $\text{Mn}^{4+}$  to obtain  $\text{NaMnF}_5$  would take place at the average potential of 4.9 V, which cannot be attained with the currently available electrolytes.[139] Similarly, the extraction of 1 mol of  $\text{Na}^+$  from the fluoroperovskite, was considered with concomitant oxidation of  $\text{Mn}^{2+}$  to  $\text{Mn}^{3+}$  to yield  $\text{MnF}_3$ . The calculated deinsertion average potential was 3.8 V, which is within the expected electrolyte electrochemical stability window. Yet, given the insulating character of fluorides, significant cell polarization is to be expected, and thus, this potential may not be practically reached, which would be in agreement with the findings by Okada et al. mentioned above.

In view of the poor electrochemical performance observed for the sodium manganese fluorides studied, if any, and considering the large polarization observed in fluorides used as electrodes in LIB technologies, we decided to broaden the scope of the work to oxyfluorinated materials.

### 3.5. Sodium manganese (oxy)fluorides.

#### 3.5.1. NaMnOF<sub>2</sub> · 2.8H<sub>2</sub>O

The synthesis procedure is similar to that as *Route B* to prepare Na<sub>2</sub>MnF<sub>5</sub> but with a molar Na: Mn ratio of 1 instead of 2. 0.349 g of Mn<sub>2</sub>O<sub>3</sub> (2.2 x10<sup>-3</sup> mol) and 0.185 g of NaF (4.4 x10<sup>-3</sup> mol) were mixed with 10 mL of 40%wt HF (0.2 mol) and stirred vigorously to favor the dissolution of the precursors. After 6 hours of stirring a brown solid precipitated in large amount which was repeatedly washed with ethanol and dried in air at 70°C.

The XRPD pattern of the brownish compound is shown in Figure 3.13a, which does not seem to correspond to any of the known compounds present in the ICSD database. When grinding or pelletizing the sample, great amounts of water losses were observed, resulting in the partial amorphization of the sample, as illustrated in Figure 3.1.3b. Therefore, the sample was dried at 100 °C but XRPD pattern disclosed a complete decomposition of the sample to a mixture consisting mostly of NaMnF<sub>4</sub> (two peaks at 14.42° and 15.10° remain unidentified), as shown in Figure 3.13c.

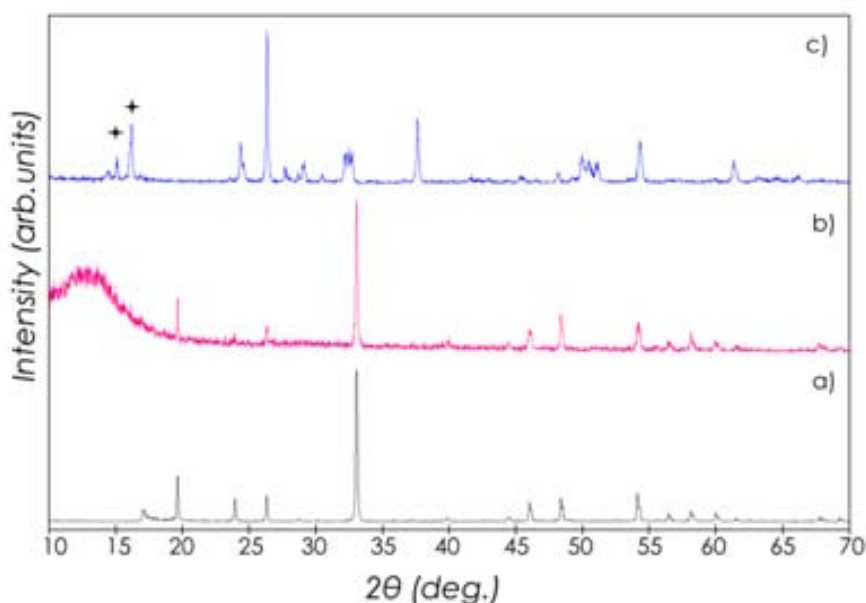


Figure 3.13. XRPD patterns of the as precipitated brownish sample a) before and b) after pelletizing at 2 bar for 50 s, and c) after heating 100 °C, which yields to decomposition to a mixture containing NaMnF<sub>4</sub> and additional unidentified product(s) (peaks marked with stars).

### 3.5.1.1. Chemical analysis and microstructural characterization

The sample consists of micrometric sized particles with high aspect ratio and somewhat irregular shape (Figure 3.14). EDX analysis indicates the presence of Na, Mn, O and F in the sample with rough average Na: Mn and F: O ratios of 1.4 and 2.2 respectively. Chemical mapping of the sample was possible due to decomposition of the sample after long exposure to the electron beam.

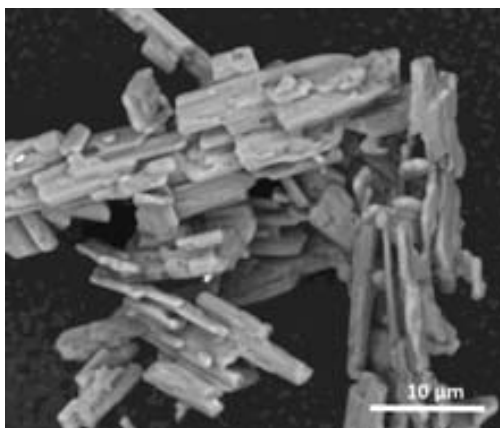


Figure 3.14 Typical SEM image of the as precipitated brown sodium manganese oxyfluoride.

The IR spectrum of the compound (shown in Figure 3.15) exhibits characteristic bands of H<sub>2</sub>O vibration modes at 3286, 1726 cm<sup>-1</sup>, which could correspond to either adsorbed or crystallized water molecules. However, presence of hydronium molecules cannot be excluded as an additional vibration observed at 1061 cm<sup>-1</sup>, which can be attributed to asymmetric bending ( $\nu_4$ ). The bands observed at 766 and 616 cm<sup>-1</sup>, are ascribed to Mn-O and Mn-F vibrations, respectively.

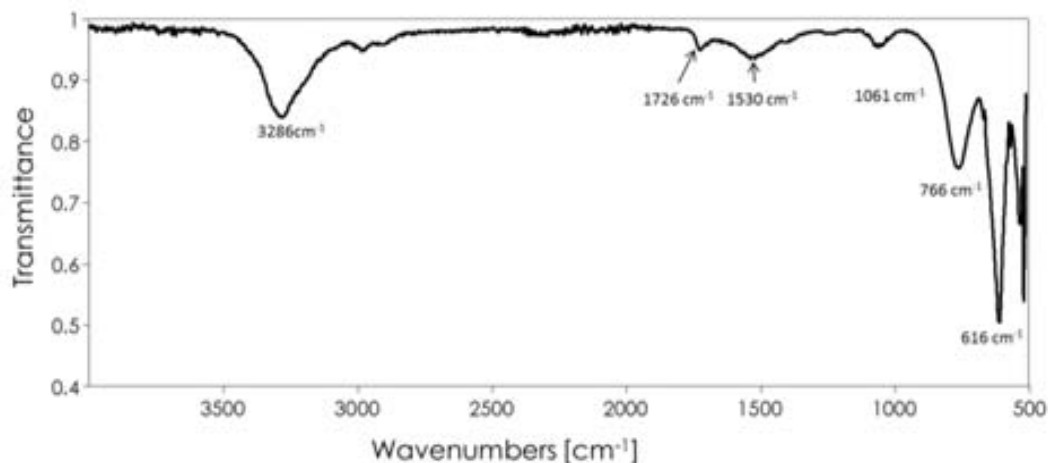


Figure 3.15. ATR-IR spectrum of the as precipitated brown sodium manganese oxyfluoride.

Chemical analysis yielded 11.3 ( $\sigma=0.43$ ) for sodium and 29.3 ( $\sigma=0.02$ ) for manganese, expressed in %wt/wt, which corresponds to an equivalent Na: Mn ratio of 1:1. The total anion and water content can be estimated indirectly from the difference in %wt. Considering F, O and H<sub>2</sub>O have a similar atomic/molecular weight, results are consistent with NaMn(O,F, H<sub>2</sub>O)<sub>x</sub> with  $x=5.8$ . In order to estimate the oxidation state of manganese ions from magnetic measurements, it is compulsory to propose a molecular formula, given the dependence of effective magnetic moment to molecular weight. Therefore, we assumed that Mn oxidation state was Mn<sup>3+</sup>, since the compound is obtained under the same synthetic conditions of Na<sub>2</sub>MnF<sub>5</sub>. Thus, formula NaMnOF<sub>2</sub>·2.8H<sub>2</sub>O was considered.

Magnetization of the sample shows a strong paramagnetic behavior reflected in the linearity of the inverse of susceptibility (Figure 3.16), in agreement with the Curie-Weiss law. The uncertainty in the empirical formula of the compound generates an error in the estimation of the effective moment. However, the paramagnetic effective moment calculated is 5.0  $\mu_B$ /Mn, which is in good agreement with the expected value for Mn<sup>3+</sup> (4.90  $\mu_B$ /Mn). Such results point at an apparent self-consistent formulation.

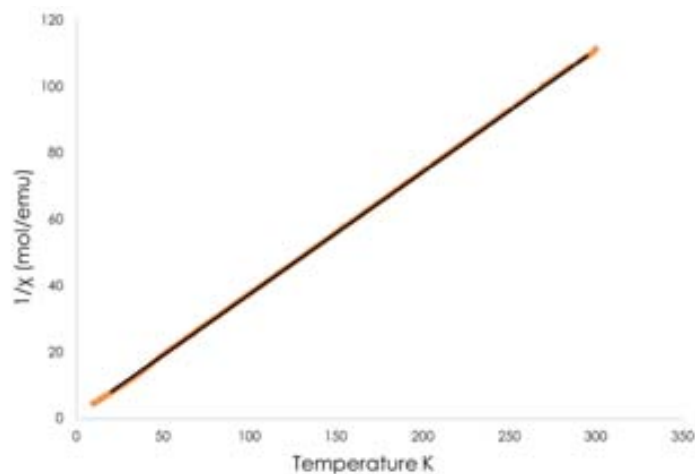


Figure 3.16. Plot of the inverse of magnetic susceptibility vs. temperature for NaMnOF<sub>2</sub>·2.8H<sub>2</sub>O with an applied field of 100 Oe.

Electron diffraction was performed with the aim to identify the cell parameters and space group of the compound. However, the sample decomposed after short periods of exposure to the electron beam and thus the elucidation of the crystal structure was approached with neutron and synchrotron X-ray diffraction data. While elucidation of the crystal structure has not been possible to date despite the attempts carried out (including direct methods), it has been possible to achieve a set of cell parameters which yield satisfactory agreement with the data available. Figure 3.17 depicts the profile matching considering both neutron and SXRPD data with an orthorhombic cell with  $a= 4.07559 \text{ \AA}$ ,  $b= 9.04090 \text{ \AA}$  and  $c= 6.77290 \text{ \AA}$  and *Cccm* space group.

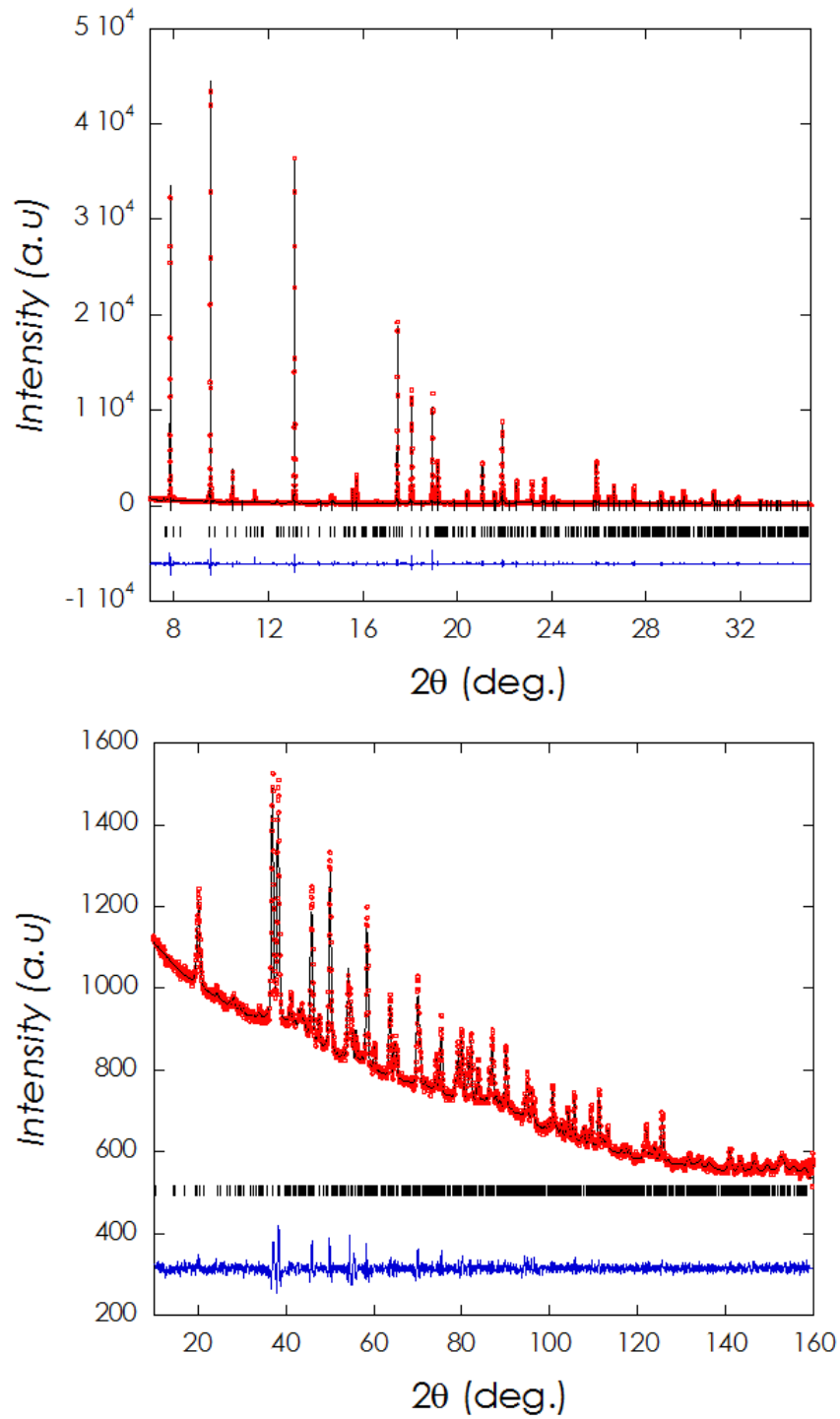


Figure 3.17. Pattern fitting of SXRPD data (above) and Neutron diffraction data (below).

Experimental pattern (red dots), calculated profile (black continuous line) and difference pattern at the bottom (blue). Bragg positions are denoted by vertical bars.

### 3.5.2. NaMnMoO<sub>3</sub>F<sub>3</sub> · H<sub>2</sub>O

Additional efforts were carried out with the aim to obtain sodium manganese oxyfluorides were unsuccessful and yielded to diverse mixtures of binary and ternary fluorides, which is in agreement with the non-existence of any sodium manganese oxyfluoride reported to date. Thus, the publication of first report dealing with the existence of CsMnMoO<sub>3</sub>F<sub>3</sub> appeared in the course of this PhD work [17] prompted us to investigate phases in the Na-Mn-Mo-O-F system. While statistical disorder for Mn(II)/Mo(VI) and also O/F anions was found in the three-dimensional CsMnMoO<sub>3</sub>F<sub>3</sub> structure, the much smaller ionic radius for sodium when compared to cesium[1] let us envision that a different structural type would form with reasonably lower coordination number (CN) for sodium ions.[8] NaMnMoO<sub>3</sub>F<sub>3</sub>·H<sub>2</sub>O was obtained by three slightly different synthetic routes using Na<sub>2</sub>MoO<sub>4</sub>·2H<sub>2</sub>O as molybdenum source. In all cases, precursors were previously dissolved in distilled water and subsequently mixed together and brought to dryness on a hot plate at 80°C. *Route 1* (45% yield) involved the mixing a solution 0.726 g Na<sub>2</sub>MoO<sub>4</sub>·2H<sub>2</sub>O (3.00×10<sup>-3</sup>mol, ca. 0.12M) with a solution 0.496 g NaHF<sub>2</sub> (8.00×10<sup>-3</sup>mol, ca. 0.32) and 0.279 g MnF<sub>2</sub> (3.00×10<sup>-3</sup> mol). Distilled water was added until a final volume of 80 mL was reached. After magnetic stirring and sonication, a small amount of undissolved material was separated by centrifugation and the remaining clear dissolution which was then brought to dryness. The solid thus achieved was repeatedly washed with water and finally dried at 60°C in air. Interestingly, the yield of the reaction was ca. 140% in all the synthesis performed, which was the first indication of the presence of water molecules in the as prepared compound.

The other two routes involved the use of Mn(CH<sub>3</sub>COO)<sub>2</sub>·4H<sub>2</sub>O as manganese precursor and HF, and only differing in the overall sodium concentration in the reacting mixture.

*Route 2* (25% yield) consisted of mixing a solution of 7.26 g of Na<sub>2</sub>MoO<sub>4</sub>·2H<sub>2</sub>O (3.0×10<sup>-2</sup> mol, ca. 0.3 M) with a solution of 7.35 g Mn(CH<sub>3</sub>COO)<sub>2</sub>·4H<sub>2</sub>O (3.0×10<sup>-2</sup>mol, ca. 0.6 M), a solution of 4.62 g of NaF (11.0×10<sup>-2</sup> mol, ca. 4.4 M) and finally 4 ml HF (48% aqueous solution, 9.6×10<sup>-2</sup>mol). The larger sodium concentration resulted in the direct precipitation of NaMnF<sub>3</sub>, which was subsequently separated by decantation. The remaining solution was treated following the procedure described above.

Route 3 (60% yield) allowed to avoid the formation of any by-product in the course of the reaction by starting from a solution 2.41 g  $\text{Na}_2\text{MoO}_4 \cdot 2\text{H}_2\text{O}$  ( $1.00 \times 10^{-2}$  mol, ca. 0.2M) with a solution of 2.45 g of  $\text{Mn}(\text{CH}_3\text{COO})_2 \cdot 4\text{H}_2\text{O}$  ( $1.00 \times 10^{-2}$  mol, ca. 0.2M) and 1.5 mL of HF (48%, aqueous solution,  $4.08 \times 10^{-2}$  mol) which yielded a clear solution after mixing. In this case, the mixture was also heated at  $80^\circ\text{C}$  but not brought to dryness. The precipitated solid was recovered after 10h reaction and washed and dried as in the other two cases. The XRPD pattern was identical for all samples, except for the presence of a tiny amount of unidentified impurities on the large batch prepared for neutron diffraction.

Many attempts to obtain single crystals were carried out at  $150^\circ\text{C}$  under hydrothermal conditions. Unfortunately, the syntheses yielded mixtures of manganese fluoride and molybdenum oxides.

### 3.5.2.1. Chemical analysis and microstructural characterization

Scanning Electron Microscopy revealed that the samples are constituted of very thin crystallites of micrometric size (Figure 3.18). EDX data analysis allowed ascertaining that the elemental composition is homogeneous and normalization with respect to manganese content yielded a Na:Mn:Mo ratio of ca. 0.7:1:0.7. Additionally, the O/F ratio was found to be larger than one.

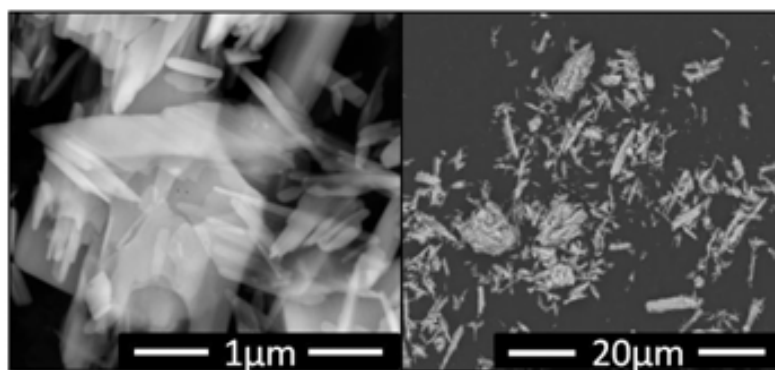


Figure 3.18. SEM images at different magnifications for  $\text{NaMnMoO}_3\text{F}_3 \cdot \text{H}_2\text{O}$

The determination of the relative amounts of sodium, manganese and molybdenum, in weight %, was carried out by chemical analysis that yielded 7.8 ( $\sigma=0.15$ ), 17.4 ( $\sigma=0.05$ ) and



33.2 ( $\sigma=0.05$ ), respectively. Such values are in full agreement with the expected values (7.74, 18.50 and 32.31) for the proposed formula NaMnMoO<sub>3</sub>F<sub>3</sub> · H<sub>2</sub>O.

The presence of water molecules in the crystal lattice was confirmed by IR measurements in ATR mode. Figure 3.19 depicts the IR spectrum with the characteristic bands of H<sub>2</sub>O molecule at 1651 cm<sup>-1</sup>, 3516 cm<sup>-1</sup> and 3563 cm<sup>-1</sup> present in the IR spectrum, which correspond to the HOH bending and O-H antisymmetric and symmetric stretching vibrations, respectively. The doublet observed around 3560 cm<sup>-1</sup>, together with the intense bending band are indications of water molecules in the crystal lattice.[140,141] The absence of other bands in that region excludes the possibility of having major amounts of OH<sup>-</sup> or H<sub>3</sub>O<sup>+</sup> in the crystalline lattice.[142–144] The absorption bands observed at the range 600-1000 cm<sup>-1</sup> may be ascribed to the M-O (M=Mo,Mn) given that stretching vibrations while M-F bands would be expected at lower wavenumbers.[145]

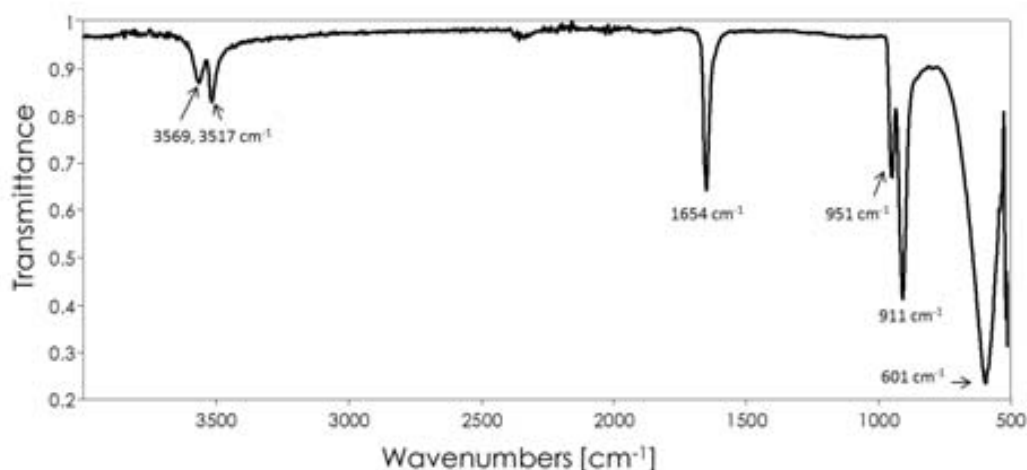


Figure 3.19. ATR-IR spectrum of as-prepared sample showing characteristic vibration bands of the water contained in the crystal lattice at 1651 cm<sup>-1</sup>, 3516 cm<sup>-1</sup> and 3563 cm<sup>-1</sup>.

Magnetization and inverse of the susceptibility versus temperature are shown in Figure 3.20. Antiferromagnetic behavior is observed at 16 K and above that temperature, the validity of the Curie-Weiss law in this compound is clear from the linear behavior of  $\chi^{-1}$ . The effective paramagnetic moment extracted per Mn ion is  $\mu_{\text{eff}}=5.87(2) \mu_{\text{B}}/\text{Mn}$  assuming that the

composition is  $\text{NaMnMoO}_3\text{F}_3 \cdot \text{H}_2\text{O}$ . Such result is fully consistent with the expected value for Mn(II) ( $5.92\mu_B/\text{Mn}$ ) and the presence of diamagnetic Mo(VI).

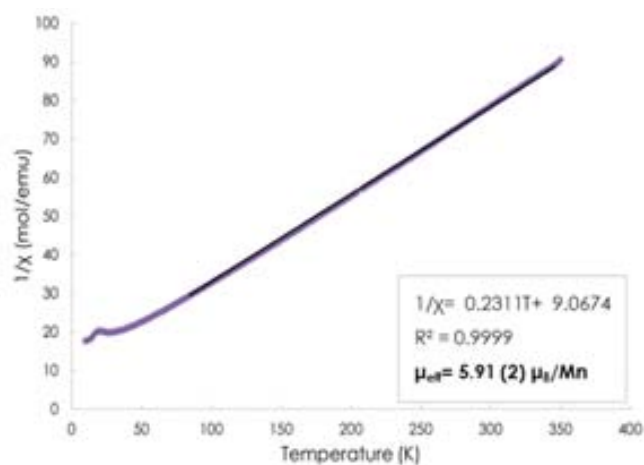


Figure 3.20. Inverse of the magnetic susceptibility as a function of temperature with and applied field of 1000 Oe.

Regardless of the minor differences in the synthetic routes,  $\text{NaMnMoO}_3\text{F}_3 \cdot \text{H}_2\text{O}$  samples were found to have the same crystal shape. Significant preferred orientation has been detected by comparing XRPD patterns obtained using standard and side-loaded sample holders. Changes in the relative intensity of the peaks are observed, as illustrated in Figure 3.21.

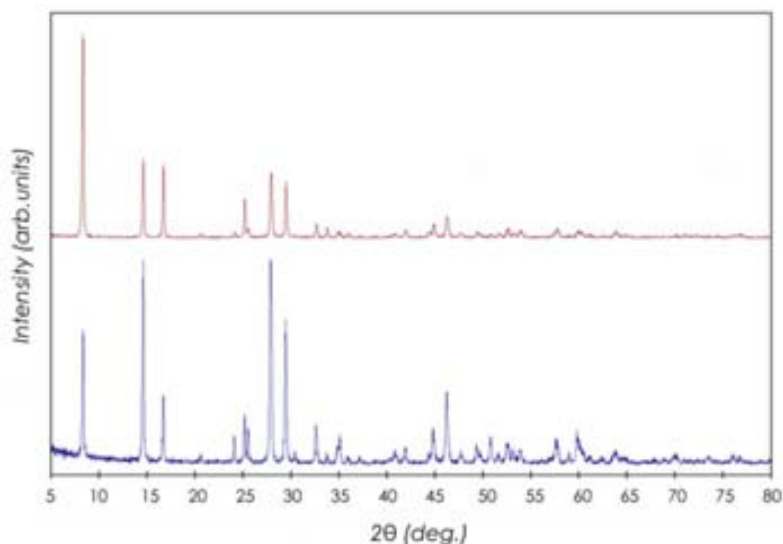


Figure 3.21. Typical XRPD patterns (standard (above) and side loaded (below) sample holders) for  $\text{NaMnMoO}_3\text{F}_3 \cdot \text{H}_2\text{O}$  by Route 2.

The laboratory XRPD pattern of the sample was found to be different from the one exhibited by CsMnMoO<sub>3</sub>F<sub>3</sub> in agreement with a different crystal structure expected due to the smaller size of sodium respected to cesium and also to the presence of crystallization water. The XRPD pattern was successfully indexed with an orthorhombic cell with parameters  $a=3.595 \text{ \AA}$ ,  $b=21.247 \text{ \AA}$  and  $c=7.389 \text{ \AA}$ . Systematic reflection absences in these patterns indicate that the lattice is C-face centered and, according to SGAID tool (DAJUST program), the possible space groups (SG) are *C mcm*, *C mc21* and *C 2cm*. The indexing of the pattern evidences that reflections enhanced due to the preferred orientation correspond to 0k0 type, which is in agreement with the plate-like morphology of the crystallites.

First attempts to solve the crystal structure were conducted assuming a centrosymmetric *C mcm* (no. 63) SG. A peak in the real space electronic density was clearly found at 4c Wyckoff position with  $y=0.31$  and a Na atom was initially placed at this position. Synchrotron XRPD patterns were satisfactorily indexed and refined using the structural model derived from laboratory XRPD thus confirming its validity. NPD pattern shows an odd background noise fully consistent with the presence of hydrogen atoms in the compounds. While the NPD pattern can be indexed with the cell parameters derived from XRPD data, it cannot be successfully fitted with the proposed structural model. To better understand this issue and complete the structural elucidation, we first ran Patterson analyses with the extracted integrated intensities –which are independent of the structural model. Patterson maps show a negative peak at about  $1 \text{ \AA}$  from the origin in agreement with water being crystallized in the structure. Fourier analyses of the NPD patterns with the structure found by X-rays showed two negative peaks ( $bH= -3.74 \text{ fm}$ ) near the 4c Wyckoff position with  $y=0.31$  that must correspond to H nuclei. This drove us to conclude that water molecules are placed at this position.

This model rendered a good refinement of synchrotron XRPD ( $R_B=4.25\%$ ,  $\chi^2=3.2$ ) data. Refinement of the NPD data renders worse agreement parameters due to two facts: the larger preferred orientation owing to the large amount of material needed to fill the sample holder (~8 mm in diameter) which is not rotated during data collection; and most important, the large incoherent scattering introduced by hydrogen atoms in the NPD patterns. Since

the values obtained for the Debye-Waller factors are strongly dependent on the absorption correction considered, we have considered  $U$  of Mo to be the same for SXRPD and NPD to indirectly estimate absorption effects. Agreement factors improve significantly considering anisotropic Debye-Waller factors ( $R_B=6.3\%$ ,  $\chi^2=3.4$ ).

Even if agreement factors derived from the above mentioned refinements are a proof of the reliability of the structural model proposed, a few tiny peaks remain unindexed, with integrated intensities  $< 1\%$  compared to the most intense peak for both SXRPD and NPD. Such reflections can be indexed by doubling  $a$  parameter in the  $Pbca$  space group ( $a=7.1894(2) \text{ \AA}$   $b=21.246(1) \text{ \AA}$   $c= 7.3893(2) \text{ \AA}$ ) (Figure 3.23). Since the peaks are clearly seen in the SXRPD, we could hypothesize that the superstructure is related to small displacement in the position of the heavier atoms. A plausible hypothesis, in agreement with larger  $B$  values obtained for Mn than for Mo (3.7 and 1.6 respectively), is that the superstructure originates from slight distortions within the  $MnX_6$  octahedra.

An electron diffraction study was undertaken with the aim of showing further light on that matter. The sample was found to be rather stable upon irradiation so the reconstruction of the reciprocal lattice was possible. Yet, interpretation of the results is complex due to double diffraction and to the very thin nature of the crystals along the  $b$  direction. This, coupled to the long value  $b$  parameter ( $b=21.2 \text{ \AA}$ ) leads to elongated diffraction rods from upper levels penetrating the diffraction sphere. ([146]) Figure 3.20 exhibits a representative image of a crystallite together with electron diffraction patterns for the [001] and [010] zone axes. Taking into account the above mentioned issues, patterns were indexed with the  $C$ - $c$ - extinction symbol and cell parameters  $a=3.60 \text{ \AA}$ ,  $b= 20.93 \text{ \AA}$ ,  $c= 7.46 \text{ \AA}$ . Still, additional unindexed reflections were observed in all crystals at  $(1/2 k l)$  and  $(3/2 k l)$  (see Figure 3.22b) in agreement with the above mentioned doubling of the  $a$  parameter. Indexation considering such reflections unambiguously points to  $Pbca$  space group. Also, most crystals were found to exhibit very weak additional spots or diffuse lines (figure 3.22c)) which would be consistent with the doubling of the  $b$  and  $c$  parameters, pointing at an even larger unit cell and a more complex superstructure.

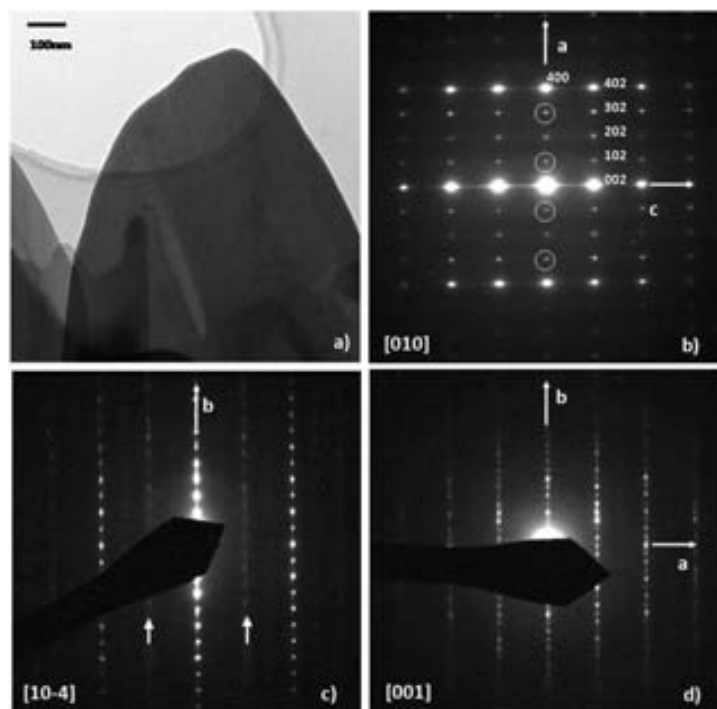


Figure 3.22. Typical TEM image for NaMnMoO<sub>3</sub>F<sub>3</sub>·H<sub>2</sub>O and electron diffraction patterns corresponding to the b) [010], c) [10-4] and d) [001] zone axes. The circles marked in b) correspond to double diffraction spots and the white arrows in c) indicate diffuse extra lines at positions between the 0k0 and h0l reflections.

The crystal structure of NaMnMoO<sub>3</sub>F<sub>3</sub>·H<sub>2</sub>O is depicted in Figure 3.41. It is formed by the stacking –along the *b* axis- of MnX<sub>6</sub> octahedra layers (purple octahedra, X=O, F) that share corners along *c*- and *a*- directions. These MnX<sub>6</sub> layers are connected to MoX<sub>6</sub> (olive green) octahedra while Na ions (yellow) and water molecules are accommodated in the large interlayer space.

Elucidation of plausible F/O ordering was attempted by applying Pauling's second crystal rule.<sup>[6,147]</sup> The bond strength sums (*b*) for each anionic position (X1 to X4) was calculated and found to be 1.78, 0.92, 1.12 and 2 respectively, which would point at X1 and X4 being occupied by O and X2 and X3 by F. The multiplicities of these positions for full occupation are in agreement with the proposed formula unit. Such distribution seems chemically reasonable in the sense that X1(O) is a corner bridging position between three MX<sub>6</sub> octahedra (two MnX<sub>6</sub> and a MoX<sub>6</sub>) and X3(F) is a terminal corner position for a MoX<sub>6</sub>

octahedron. The other remaining positions, X2 and X4 are both corner bridging between two  $\text{MX}_6$  octahedra, with  $\text{M}=\text{Mn}$  for X2(F) and  $\text{M}=\text{Mo}$  for X4(O). Results are also consistent with the more highly charged anion been coordinated to the cation with higher oxidation state.

In order to confirm the above mentioned conclusions, we performed a bond valence sum analysis (using parameters implemented in FullProf Suite of programs) exploring all the cationic distributions compatible with the stoichiometry: (i) X1,X4= O and X2,X3= F; (ii) X1,X4= F and X2,X3= O; or (iii) X1= O; X2,X4= F and X3=O/F. Similar BVS values were obtained in all cases for manganese and sodium (close to 2.0 and 1.0 respectively) while significant differences were observed for molybdenum. The anionic distribution deduced from Pauling's second rule (i) renders a value of 5.9 while (ii) and (iii) yielded respectively 5.5 and 6.4; which are either not consistent with the results of magnetic measurements or unrealistic.

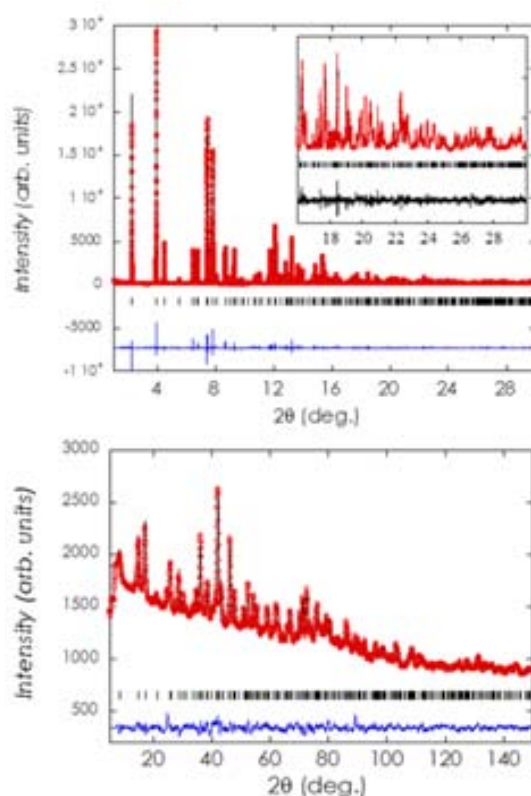


Figure 3.23. Synchrotron XRPD and (b) NPD patterns (small circles) showing the experimental pattern (red dots), the final Rietveld fit (black continuous line) and difference pattern at the bottom (blue). Bragg positions are denoted by vertical bars.

Table 3.1: structural details found by the joint Rietveld refinement of NPD and synchrotron XRPD data.

**NaMnMoO<sub>3</sub>F<sub>3</sub> H<sub>2</sub>O**

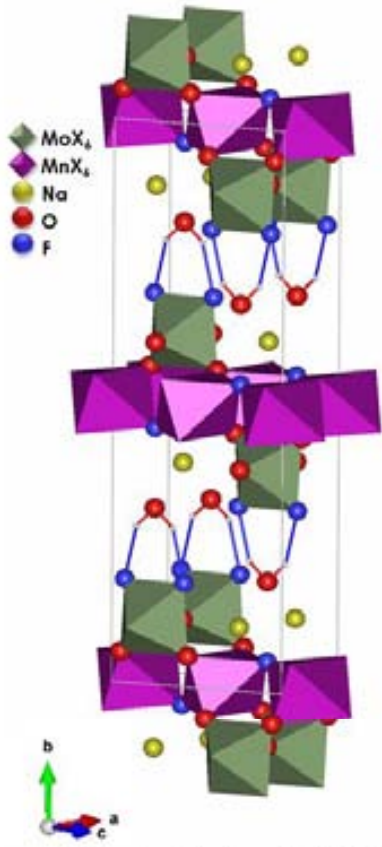
Space group	C mcm (n°63)	Wyckoff positions				
	a= 3.5947(1) Å					
Cell parameters (Å)	b= 21.246(1) Å	4b (0 ½ 0)	Mn			
	b= 7.3893(2) Å					
		4c (0 y ¼)	Na	y	0.885(1)	
			Mo	y	0.135(1)	
			Ow	y	0.312(1)	
			X2	y	0.455(1)	
			X4	y	0.605(1)	
			8f (0 y z)	H	y	0.282(2)
				z	0.354(4)	
			X1	y	0.056(4)	
				z	0.445(1)	
			X3	y	0.188(1)	
			z	0.425(1)		

Figure 3.24. Crystal structure for NaMnMoO<sub>3</sub>F<sub>3</sub> H<sub>2</sub>O

Cell parameters and atomic positions for the average cell considering the O/F ordering scheme deduced above are given in Table I while selected bond distances and angles are reported in Table 3.2.

Table 3.2. Selected bond lengths and angles resulting from the joint Rietveld refinement of NPD and synchrotron XRPD data.

	Length (Å)		Angle (deg.)
<u>Mn</u>			
$d_{\text{Mn-O1}}$	2.192(5)	O1-Mn-O1 (x2)	110.2 (2)
		O1-Mn-O1 (x2)	69.8 (4)
		O1-Mn-O1 (x2)	180.00(-)
$d_{\text{Mn-F2}}$	2.078(6)	O1-Mn-F2 (x4)	94.7(4)
		O1-Mn-F2 (x4)	85.3(3)
		F2-Mn-F2	180.00(-)
<u>Mo</u>			
$d_{\text{Mo-O1}}$	2.207(6)	O1-Mo-O1	81.4(5)
		O1-Mo-O4 (x4)	75.5(4)
		O1-Mo-F3 (x2)	90.6(9)
		O1-Mo-F3 (x2)	172.0(9)
$d_{\text{Mo-O4}}$	1.905(9)	O4-Mo-O4	141.4(2)
		O4-Mo-F3 (x4)	102.6(6)
$d_{\text{Mo-F3}}$	1.716(9)	F3-Mo-F3	97.3(9)

The presence of sodium ions in the structure does certainly contribute to ordering of anions. Indeed, all inorganic solids composed of long-range ordered oxide fluoride transition metal anions contain sodium cations.[148] The coordination environment around sodium ions can be described as a distorted cube with two shortest Na-F2 (2.330(3) Å) and two longest Na-F3 (2.864(4) Å) distances. These values compare well with Na-F distances observed for NaI cubic in  $\text{Na}_2\text{MnMF}_7$  (M= Cr, V) weberites([149,150]) that range from 2.27 Å to 2.49 Å. Similar Na-F distances around 2.3 Å are also reported for layered  $\text{NaNbO}_2\text{F}_2$ ([151]) which exhibits 6+1 coordination around sodium with Na-O distances of 2.58 Å and 3.13 Å. The Na-O distances for  $\text{NaMnMoO}_3\text{F}_3 \cdot \text{H}_2\text{O}$  are 2.579(3) Å for O1 and 2.386(3) Å for Ow. For comparison, Na-O



and Na-Ow distances around 2.33 Å have been reported for six-coordinated sodium ions in NaMoO<sub>3</sub>F<sub>4</sub> and Rb<sub>3</sub>Na(MO<sub>2</sub>F<sub>4</sub>)<sub>2</sub> · H<sub>2</sub>O (M=Mo, W)[148] respectively.

The water molecule performs a dual role in the structure coordinating sodium and enlarging the interlayer distance so that electrostatic repulsion between the layers is lowered. H-O distance is 0.96(7) Å and H-O-H bonding angle of 101(5)° which would indicate a possible hydrogen bonding between H and F(X3). Distances are 2.09 Å for H-F3 above (drawn with blue lines in Figure 3.20) and 2.54 Å for H-F3 in the plane.

The distribution of anions yield distorted octahedral MO<sub>4</sub>F<sub>2</sub> (M=Mo, Mn) units for both transition metals (see values in Table 2 and scheme depicting coordination environments in Figure 3.21). Distorted MX<sub>6</sub> coordination has been reported for O/F anion ordered structures consisting of either discrete [5,113,152,153] or connected Mo(VI)X<sub>6</sub> octahedra.<sup>40,42-44</sup> NaMoO<sub>3</sub>F<sub>3</sub> elpasolites([5,152]) exhibiting discrete Mo(VI)X<sub>6</sub> octahedra and other compounds with bi-octahedral corner-sharing([154]) (Mo<sub>2</sub>O<sub>5</sub>F<sub>6</sub>)<sup>4-</sup> or face-sharing([155]) (Mo<sub>2</sub>O<sub>6</sub>F<sub>3</sub>)<sup>3-</sup> units tend to show three longer and three shorter Mo-X distances. Structures with higher connectivity (i.e. larger number of bridging anions) have been shown to exhibit alternative distortions. MnMoO<sub>4</sub> with corner sharing M(VI)O<sub>6</sub> three dimensional structure([156]) exhibits two short, two medium and two long M-O distances around 1.7 Å, 1.9 Å and 2.1 Å respectively, as is also the case for MoO<sub>2</sub>F<sub>2</sub>([157]) with a triangular columnar framework and NaMoO<sub>3</sub>F([158]) which is built of edge-sharing Mo(VI)X<sub>6</sub> octahedra double chains. In the case of NaMnMoO<sub>3</sub>F<sub>3</sub> · H<sub>2</sub>O distances around Mo (VI) are similar to the latter: Mo-O1= 2.207(6) Å, Mo-F3= 1.716(9) Å and Mo-F4= 1.905(9) Å. The shortest Mo-F3 distances correspond to terminal anions in cis- configuration in full agreement with observations for NaMoO<sub>3</sub>F([158]).

Mn(II)X<sub>6</sub> octahedra are all corner sharing, with the coordination around Mn exhibiting four Mn-O1 2.192(5) Å "equatorial" and two Mn-F2 2.078(6) Å "axial" distances (see Table 3.2 and Figure 3.25). Such values compare well with those reported in the literature for corner sharing Mn(II)O<sub>6</sub> (e.g. 2.08-2.30 Å for MnMoO<sub>4</sub>[156] and Mn(II)F<sub>6</sub> (e.g. 2.04-2.09 Å for NaMnF<sub>3</sub>[137] and Na<sub>2</sub>MnMF<sub>7</sub> weberites.[149,150] While the F2-Mn-F2 angle is 180°, the refinement yields bond angle values in the Mn-O1 "equatorial" which depart significantly

from 90° (69.8° and 110.1°) which could indeed be an indication that the coordination around manganese atoms is not well represented by the average structure and a plausible splitting of manganese positions being at the origin of the observed superstructure.

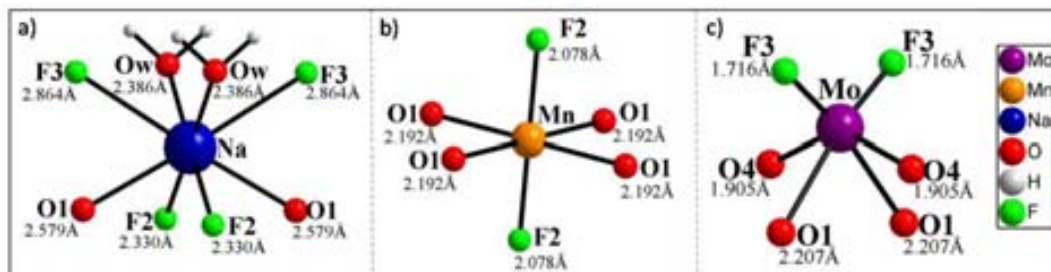


Figure 3.25. Scheme depicting coordination environments around metal atoms.

### 3.8. Electrochemical characterization

The electrochemical performance of NaMnMoO<sub>3</sub>F<sub>3</sub> · H<sub>2</sub>O was tested vs Na<sup>0</sup> in 1M NaClO<sub>4</sub> in EC: PC between 4.6 and 2.8 V. As illustrated in the corresponding potential vs capacity profile (Figure 3.26), oxidation takes place at ca. 4.4 V vs Na<sup>0</sup> and seems to be reversible with a capacity of ca. 80 mAh/g, similar to that observed for the blank experiment containing only SP carbon. *In situ* X-ray diffraction patterns (see Figure 3.26) taken during a whole oxidation/reduction cycle indicate do not exhibit any change and hence confirm the redox process observed is not related to sodium de-insertion and re-insertion in the material but rather due to electrolyte degradation, as previously observed for the fluorides NaMnF<sub>3</sub> and Na<sub>2</sub>MnF<sub>5</sub>.

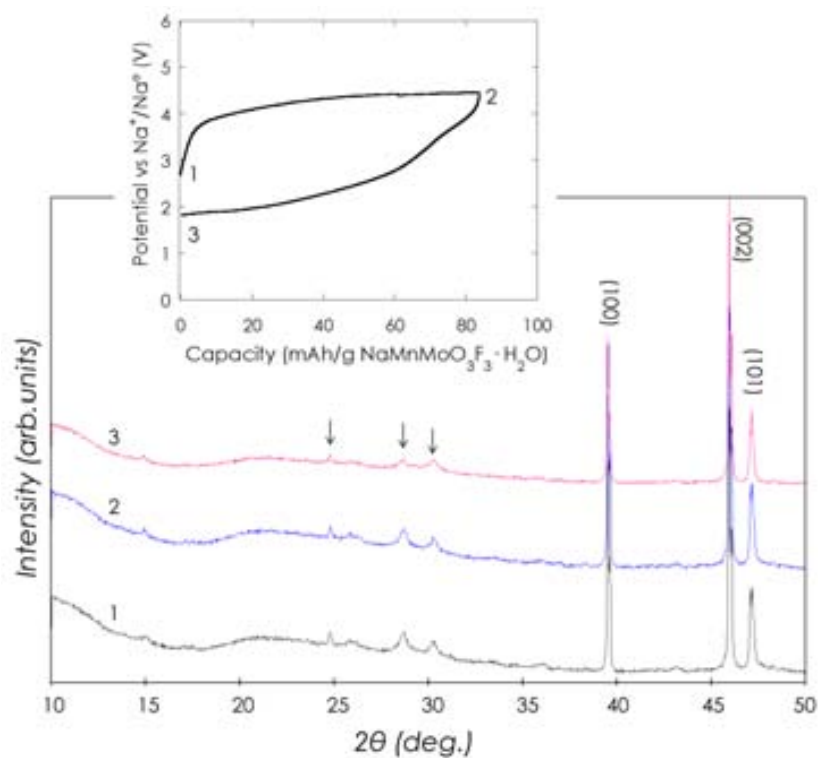


Figure 3.26. *In situ* XRPD patterns corresponding to electrodes containing  $\text{NaMnMoO}_3\text{F}_3 \cdot \text{H}_2\text{O}$  upon electrochemical oxidation and reduction. Indexed diffraction peaks correspond to Be metal used in the electrochemical cell. (see Section 2.3) while arrows identify the diffraction peaks corresponding to  $\text{NaMnMoO}_3\text{F}_3 \cdot \text{H}_2\text{O}$ .

In conclusion, the electrochemical activity of the sodium manganese (oxy)fluorides prepared during this work cannot be fully excluded, but if any, it would take place at potentials which cannot be achieved with standard electrolytes. This is also a major hurdle not only for SIB but also for the development of high potential LIB and a major sub-area of research in that field. Thus, and we are confident that future breakthroughs in that area will lead to new concepts that could enable further development of such “reactive” transition metal fluorinated compounds.

# **CHAPTER 4:**

## **Study of the Na-V-(O,F) system**

*Synthesis,*

*Characterization,*

*Electrochemical testing of:*

*NaVF<sub>4</sub>, Na<sub>3-6</sub>VOF<sub>5</sub>, Na<sub>5</sub>V<sub>3</sub>O<sub>3</sub>F<sub>11</sub>*

#### 4.1. Synthesis of sodium vanadium (oxy)fluorides.

In view of the versatility of hydro- and solvothermal synthesis for vanadium (oxy)fluorides, nicely shown by Lightfoot *et al.*, [56,159], we decided to attempt the preparation of sodium vanadium (oxy)fluorides using these methods. Sodium nitrate, vanadium pentoxide and hydrofluoric acid were used as precursors and ethylene glycol as solvent, either pure or mixed with water. Reactions were carried out at 100 °C for 12h. In order to explore the system and see the type of phases that could be achieved, a Na:V molar ratio of 1 was selected for the tests. The stoichiometric ratio between the precursors was kept constant: 0.170 g of NaNO<sub>3</sub> (2 x10<sup>-3</sup> mol), 0.182 g of V<sub>2</sub>O<sub>5</sub> (1 x10<sup>-3</sup> mol) and 0.5 mL of HF while the amount of ethylene glycol (V<sub>EG</sub>) and water (V<sub>water</sub>) were varied, keeping a total volume of 10ml to avoid introducing significant variations in the concentration of metal ions.  $V_{Total} = 10 \text{ mL} = V_{EG} + V_{water}$  where V<sub>water</sub> took values from 0 to 4 mL. The solids obtained during the syntheses were identified by XRPD. The samples prepared with 0 to 2 mL of water (10 to 8 mL of EG, respectively) were light green and corresponded to a single phase with an XRPD pattern typical of a cryolite- type structure. As the water content was increased to 3 mL, a blue precipitate was achieved in a very small amount that was found to consist of Na<sub>4</sub>V<sub>2</sub>O<sub>2</sub>F<sub>8</sub>, which was previously reported [159] and prepared under similar conditions. Its structure contains VX<sub>6</sub> dimers separated by sodium ions. When the water content was increased to V<sub>water</sub> = 3, 4 mL, a much larger amount of precipitate was achieved (ca. 300mg), which exhibits again the XRPD pattern typical of the cryolite- type compound (see Figure 4.1). Several unsuccessful attempts were made to achieve a larger amount of Na<sub>4</sub>V<sub>2</sub>O<sub>2</sub>F<sub>8</sub> using different synthetic conditions, and thus this phase was not further investigated.

Following the same synthetic protocol but increasing the reaction temperature to 200 °C, the synthesis yielded in all cases NaVF<sub>4</sub> as the major phase. For V<sub>water</sub>= 0-2 mL, minor amounts of a secondary phase were obtained which was further identified to have a chiolite- type structure. For V<sub>water</sub>= 3 mL, pure NaVF<sub>4</sub> was achieved while for V<sub>water</sub>= 4 mL, larger amounts of

the chiolite- type phase were obtained, as can be deduced from Figure 4.1. Syntheses with larger water contents did not allow recovering any precipitate.

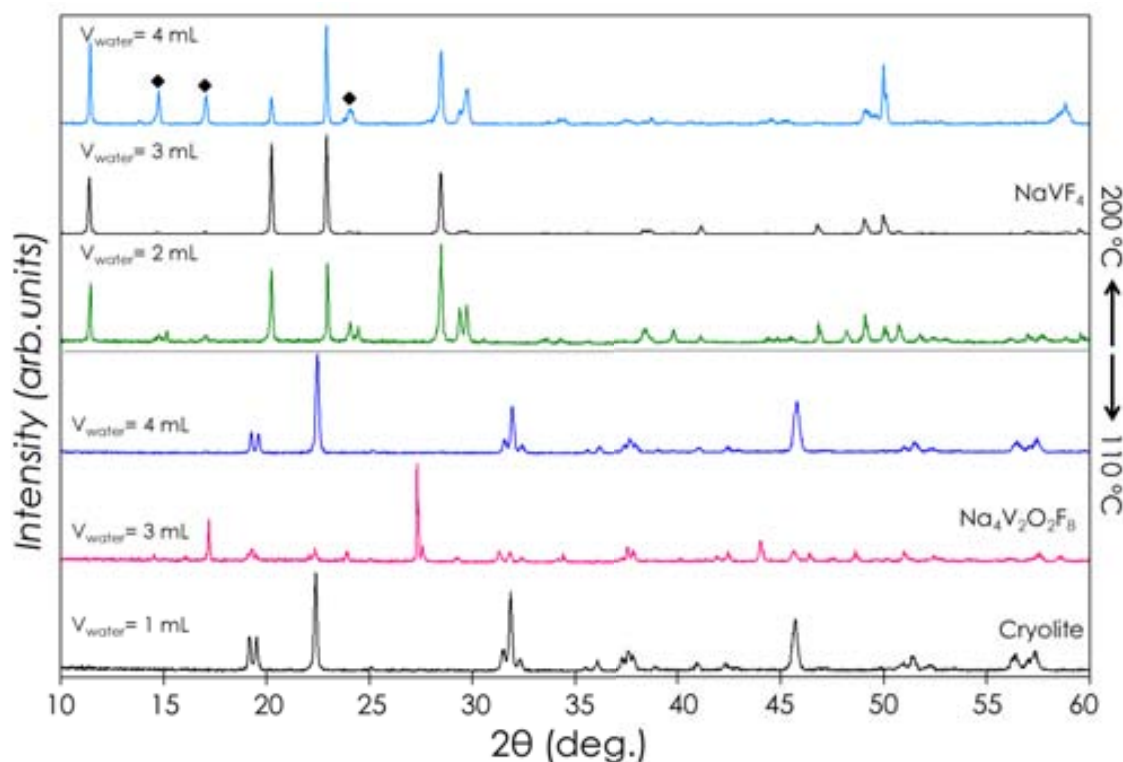


Figure 4.1. Selected XRPD patterns corresponding sodium vanadium (oxy)fluorides prepared with Na:V ratio of 1 at 100 °C and 200 °C. XRPD lines marked (◆) correspond to chiolite- type structure.

Different attempts were made to prepare the chiolite type phase pure, by modifying the synthesis conditions. It was achieved when the Na:V ratio and fluorine concentration were both increased. The pure compound precipitates after 6 hours at 100 °C with all Na:V ratios tried (1.1 to 1.7) and  $F:V \gg 1$ .

A larger batch of pure chiolite type phase was prepared in order to be able to perform NPD measurements. 0.728 g  $V_2O_5$  ( $4 \times 10^{-3}$  mol) were dissolved in 20 mL HF (40 wt. %) and kept under stirring for ca. 5 min. Then 20 mL of ethylene glycol (reducing agent) and further 1.1340 g  $NaNO_3$  ( $13.4 \times 10^{-3}$  mol) were added and the formation of the brownish precipitate observed.

As no previous reports existed on a sodium vanadium chiolite phase prepared under mild conditions, additional attempts to prepare a single crystal were carried out by increasing both the reaction temperature (to 210 °C) and the synthesis time (48h). 0.738 g of NaNO<sub>3</sub> ( $9 \times 10^{-3}$  mol) and 0.815 g of V<sub>2</sub>O<sub>5</sub> ( $4.5 \times 10^{-3}$  mol) were dissolved in 1.2 mL of HF (40 wt.%) and 10 mL of water and 25 mL of ethylene glycol were added to this solution. After cooling to room temperature, the product was washed several times with ethanol and dried at 60 °C. Inspection under the optical microscope allowed detecting that the sample consisted of a mixture of light blue small crystals and larger yellow and darker blue crystals. The latter were micrometric in size and thus, crystal of 0.48 x 0.42 x 0.30 mm<sup>3</sup> size was selected in order to determine its crystal structure. In the following sections, the characterization of the three sodium vanadium (oxy)fluorides prepared will be described while a final section will cover the results of their electrochemical testing.

## 4.2. NaVF<sub>4</sub>

### 4.2.1. Chemical analysis and microstructural characterization

NaVF<sub>4</sub> crystals obtained from synthesis at 200 °C present a needle-like morphology with average width and length of 2 μm to 150 μm, as depicted in Figure 4.3 (inset). The simultaneous presence of Na, V, and F in the crystals was confirmed by EDX analysis and negligible amounts of oxygen were detected. The IR spectrum does not exhibit any band between 4000 and 1000 cm<sup>-1</sup>, the range where bands associated with HOH bending and OH stretching vibration modes are expected, which indicate that no adsorbed or crystallized water molecules are present in the sample.

Figure 4.2 illustrates the XRPD pattern of pure NaVF<sub>4</sub> which crystallizes in the monoclinic symmetry with space group *P21/c* with cell parameters  $a=7.901 \text{ \AA}$   $b=5.313 \text{ \AA}$   $c=7.540 \text{ \AA}$  and  $\beta=101.7^\circ$ .

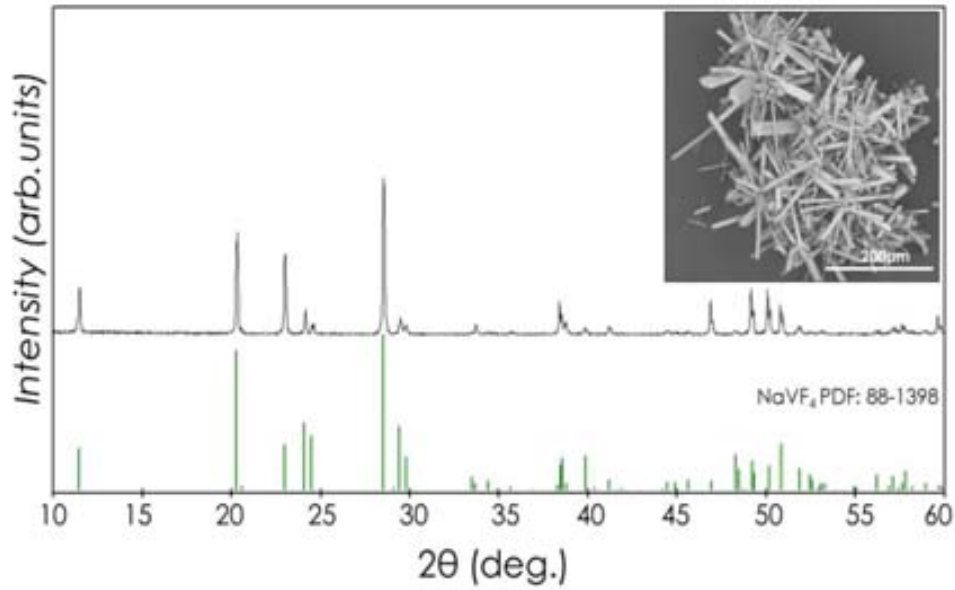


Figure 4.2. XRPD pattern of  $\text{NaVF}_4$  prepared by solvothermal synthesis (black) and reference pattern (green). A typical SEM image of the as prepared sample where the morphology of the crystals can be appreciated is shown as inset.

As solvothermal syntheses have proven to allow the preparation of a large variety of vanadium (oxy)fluorides[56,113] with different oxidation states for vanadium and the method used involved a reducing agent, the magnetic susceptibility was measured to confirm the vanadium oxidation state in  $\text{NaVF}_4$ . Figure 4.4 depicts the plot of the inverse of the susceptibility vs. temperature. Antiferromagnetic behavior is observed below 24 K (Figure 4.3), but the Curie- Weiss law can be fitted above 50K, which allows determining the effective magnetic moment from the angle of slope. The value obtained is  $2.74 \mu_B$ , which is in complete agreement with the expected value for  $\text{V}^{3+}$  ions ( $2.73 \mu_B/\text{f.u.}$ ).



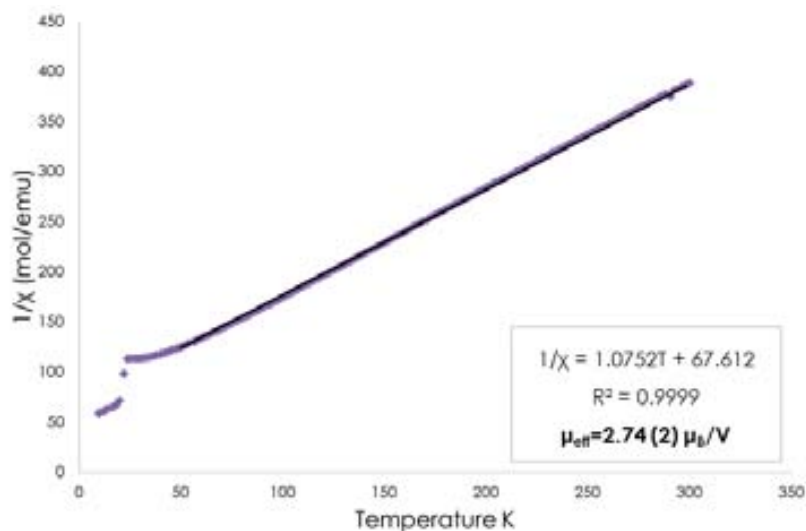


Figure 4.3. Plot of the inverse of the magnetic susceptibility vs the temperature for NaVF<sub>4</sub> measured with an applied field of 5K Oe.

### 4.3. Cryolite-type phase: Na<sub>3-δ</sub>VOF<sub>5</sub>

#### 4.3.1. Chemical analysis and microstructural characterization

The cryolite phase prepared with a ratio of water to ethylene glycol of 1:9 (v/v) was selected for further characterization. The as prepared sample consists of well crystallized cubes of ca. 2 μm in size (see a typical SEM micrograph in Figure 4.4a). Chemical EDX mapping performed on a series of crystals (as seen in Figure 4.5) allowed confirming the simultaneous presence of Na, V, F and O in all of them. This phase constitutes thus the first example of an oxyfluoride with cryolite type structure.

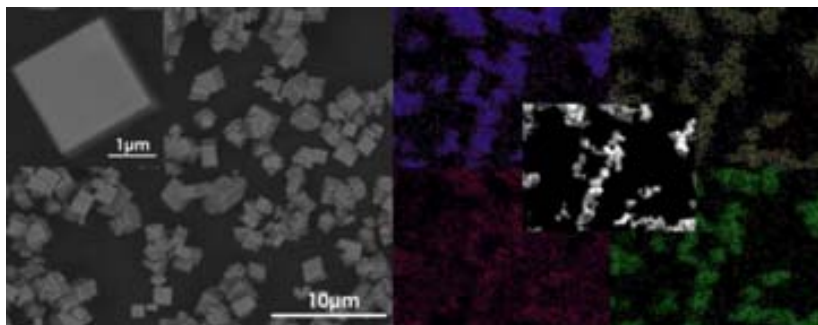


Figure 4.4a. Typical SEM images at two different magnifications of the as prepared cryolite type pure phase together with b) chemical mapping.

As in the case of  $\text{NaVF}_4$ , infrared spectra do not exhibit any band in the  $4000\text{--}1000\text{ cm}^{-1}$  range, confirming the absence of absorbed or crystallized water molecules in the sample.

The presence of oxygen in the cryolite crystal lattice points at the charge compensation mechanism being either the presence of cationic vacancies or/and an oxidation state higher than  $\text{V}^{3+}$ . Thus, magnetic measurements were performed in order to ascertain the latter. Figure 4.5 depicts a plot of the inverse of the magnetic susceptibility as a function of temperature (measured with an applied field of  $10\text{K Oe}$ ). Paramagnetic behavior is observed in the whole temperature range. The effective magnetic moment determined from the fit of the Curie-Weiss laws  $1.88\ \mu_{\text{B}}$ . Such value compares well with the expected one for  $\text{V}^{4+}$  ( $1.73\ \mu_{\text{B}}/\text{V ion}$ ), although the presence of a minor amount of  $\text{V}^{3+}$  cannot be excluded. Therefore, if the assumption is made that no cationic vacancies are present in the structure, the empirical formula  $\text{Na}_3\text{VOF}_5$  can be proposed for the prepared cryolite type phase.

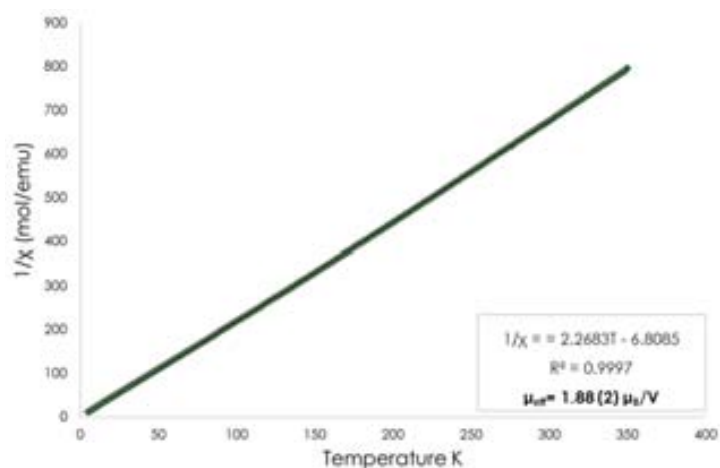


Figure 4.5. Plot of the inverse of the magnetic susceptibility vs the temperature for Na<sub>3-δ</sub>VOF<sub>5</sub> measured with an applied field of 10K Oe.

With the aim to confirm the oxidation state of vanadium, X- ray absorption measurements were performed on its K- edge at Diamond Light Source, and the results were compared to those of the reference compounds V<sub>2</sub>O<sub>5</sub> and VO<sub>2</sub>. Figure 4.6 illustrates the normalized K-edge absorption spectra of the vanadium references and Na<sub>3-δ</sub>VOF<sub>5</sub>. Differences in the absorbing- edge position and pre-edge peak intensity are observed, which disclose information about the oxidation state of V and its coordination, respectively. Pre- edge absorption features correspond to electronic 1s to 3d transition which are allowed for lower symmetries where inversion center is broken and its intensity is related to the symmetry degree of the absorbing atom sphere.[160] When comparing the pre- edge absorption intensity of the two vanadium oxides used as reference, the vanadium pentoxide presents clearly the highest absorption, which correlates to its strongly distorted coordination environment (square pyramidal). On the other hand, the vanadium coordination in VO<sub>2</sub> consists of a 6- fold oxygen array with distorted octahedral coordination where vanadium atoms are displaced from the center of the octahedral. It exhibits smaller pre- edge intensity, in agreement with the higher symmetry of its coordination environment.[161,162] The cryolite Na<sub>3-δ</sub>VOF<sub>5</sub> exhibits intermediate pre- edge intensity when compared to the references (Figure 4.6, inset), which points to the presence of distorted vanadium coordination in the oxyfluoride. This trend is in agreement with highly distorted environments

having been reported for other  $V^{4+}$  oxyfluorides where V-X distances range from 1.6 to 2.0 Å, with the shorter distance corresponding to V-O bonds. [56,159,163,164]

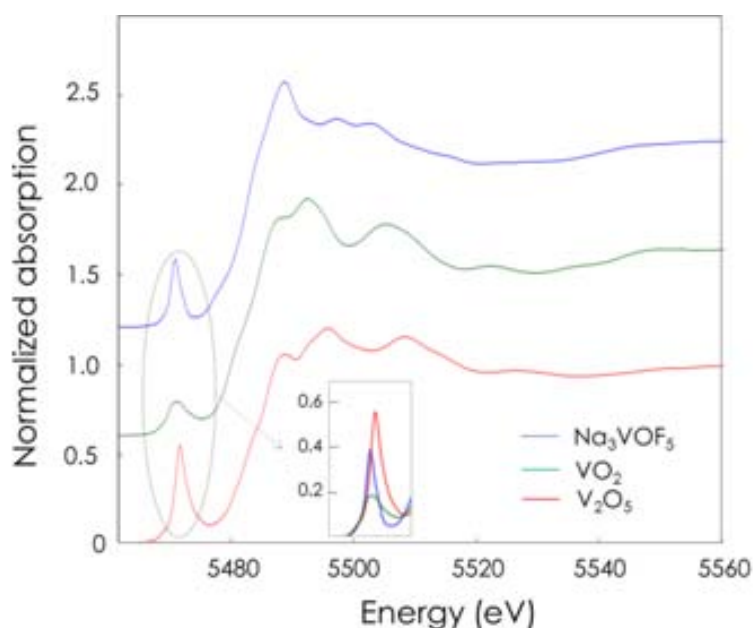


Figure 4.6. Normalized K- edge absorption spectra corresponding to cryolite  $Na_{3-6}VOF_5$  (blue),  $V_2O_5$  (red) and  $VO_2$  (green). The inset depicts superimposed pre- edge features for comparative purposes.

The oxidation state of the absorbing atom can be estimated from the energy position of the main- edge, which is usually taken as the maximum of the first derivative of the XANES spectra. However, pre- edge contributions associated to  $1s$  to  $4p$  transitions in the rising of the absorption curve make difficult the appropriate estimation of the energy position using the derivative methods. Thus, the vanadium oxidation state was estimated considering the mid- height of the normalized absorption edge of references and cryolite phase. A shift towards higher energies is generally attributed to an increase in the oxidation state, [165] as observed when comparing the relative energy position of the white line of  $V^{5+}$  and  $V^{4+}$  references. The energy position of the vanadium in the cryolite phase is also shifted to lower energies when compared to  $V_2O_5$  and is observed at a position similar to that of vanadium  $VO_2$ . A linear fitting was performed based on the energy position of the references and their

oxidation states, resulting in a vanadium oxidation state close to V<sup>4+</sup> in agreement with what was deduced from magnetic measurements.

The V-X bond distances were investigated from the EXAFS data using the software packages *Athena* and *Artemis*.<sup>[120]</sup> The crystal structure of the monoclinic Na<sub>3</sub>VF<sub>6</sub><sup>[166]</sup> was used to generate the theoretical model of the scattering paths. Many efforts were taken in order to fit the first V coordination shell, however, negative Debye- Waller factors were always obtained, which would indicate a shortcoming within the model used. Thus, the structure of VF<sub>4</sub> that also has a monoclinic symmetry (*P121/n* space group) was taken instead and a new model was generated. The fitting was carried out considering single scattering paths for the first coordination shell. The best fit obtained corresponds to a chi-square ( $\chi^2$ ) of 170.67,  $S_0^2=0.74 \pm 0.13$  and a Debye- Waller factor ( $\sigma^2$ ) of  $0.0029 \pm 0.0014$  and involves one short V-X distance of  $1.656 \pm 0.018$  Å five longer distances of  $1.941 \pm 0.018$  Å.

A Rietveld refinement of the crystal structure of Na<sub>3-δ</sub>VOF<sub>5</sub> was carried out using synchrotron X-ray diffraction data and considering a monoclinic cell and *P2<sub>1</sub>/n* (n°14) space group and cell parameters  $a= 5.54034(2)$  Å,  $b= 5.68041(2)$  Å,  $c= 7.95229(3)$  Å and  $\beta= 90.032(7)^\circ$ . Initially, occupation factors were constrained to the nominal values, which led to a large difference of the relative intensity of the main diffraction peak, as illustrated in Figure 4.7 (above). Interestingly, the same discrepancy is observed in the Rietveld refinement reported by He *et al.* <sup>[167]</sup> for the pure fluoride sodium vanadium cryolite although no explanation is given. In the cryolite structure, Na ions occupy two distinct crystallographic positions where Na(1) is 6-coordinated while Na(2) is 8-coordinated. Refinement of the occupancy factors yield 2.82Na ions per formula unit, with vacancies in Na(2) position and thus a value of  $\delta \sim 0.08$ . This makes us think that the sample prepared by He *et al.* may also exhibit sodium vacancies and thus either some fluoride vacancies or a slight amount of V<sup>4+</sup>. The final agreement factors for the Rietveld refinement of Na<sub>3-δ</sub>VOF<sub>5</sub> are  $\chi^2= 1.25$  and  $R_B= 3.99$  %. Selected bond distances and angles obtained from refinement are summarized in Table 1. Vanadium bond distances range from 1.91 to 1.93 Å, describing a regular VX<sub>6</sub> octahedra, in agreement with the obtained values for bond angles. Such coordination environment is unexpected when

considering the results obtained from the XANES study and given the fact that most of the alkali vanadium oxyfluorides reported exhibit highly distorted  $VX_6$  octahedra with  $V^{4+}$ -X distances ranging from 1.6 to 2.22 Å, where the shortest distance is generally assigned to V-O as it is the case for  $A_2VOF_3$  (A=Rb, Cs), [56]  $Na_4V_2O_2F_8$ , [159] and  $Rb_2VOF_4$ . [164] Moreover, V-F distances are larger to those observed for the analogue  $V^{3+}$  cryolite ( $Na_3VF_6$ ), which range from 1.82 to 1.87 Å, also describing a distorted octahedra. [166] Such results can be rationalized if absence of long range O/F ordering is considered as X-ray absorption technique is well suited to characterize the local coordination environment (geometry and bond distances).

Na-X bond distances obtained from SXRPD measurements are listed in Table 4.1: values for Na(1)-X(1-3) are close 2.2 Å while Na(2)-X(1-3) distances range from 2.33 to 2.85 Å, in agreement with the Na-F bond distances reported for diverse sodium metal (oxy)fluorides. [21,159,167,168]

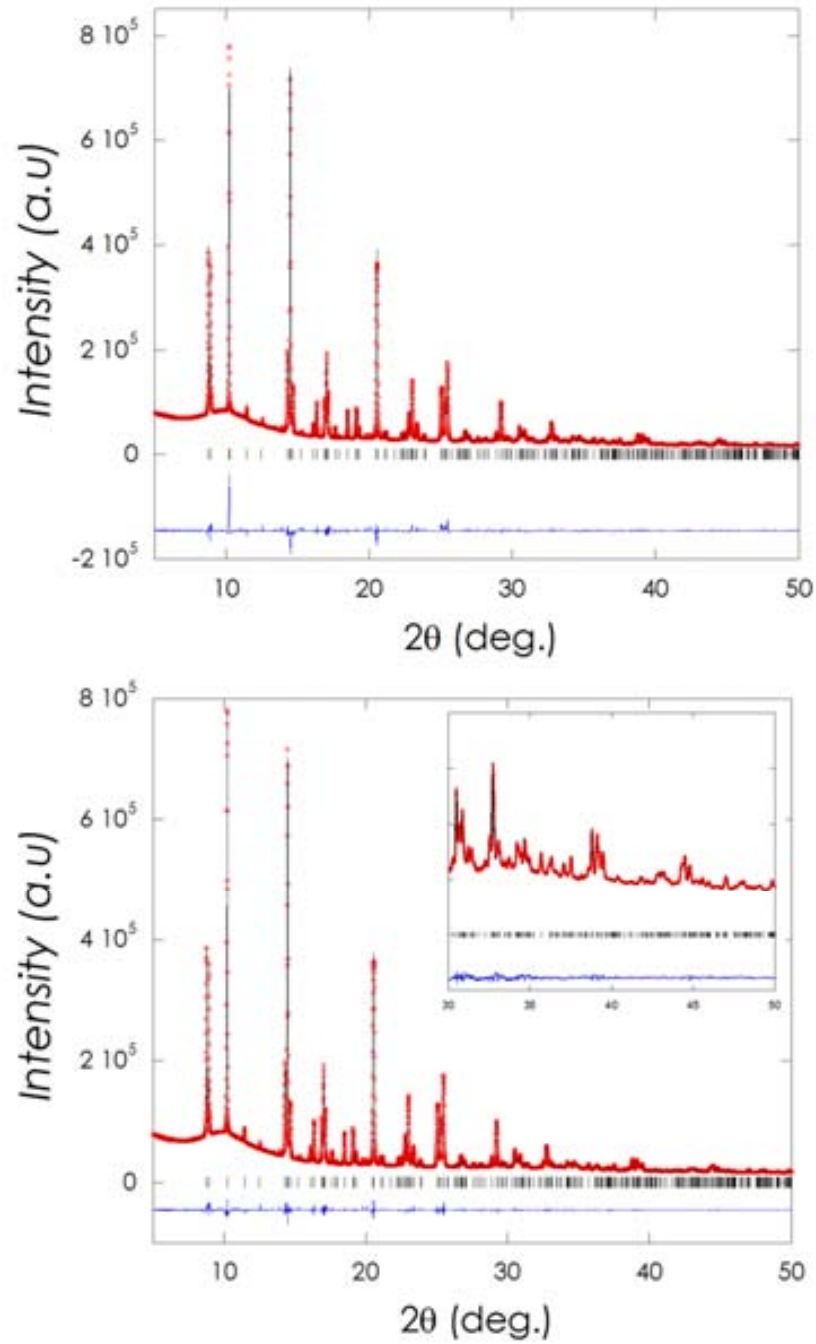


Figure 4.7. Rietveld refinement of Na<sub>3-δ</sub>VOF<sub>5</sub> considering the existence of sodium vacancies in the structure (above) or full occupation for sodium sites (below). Experimental pattern (red dots), calculated profile (black continuous line) and difference pattern at the bottom (blue). Bragg positions are denoted by vertical bars.

Table 4.1. Selected bond distances and angles for  $\text{Na}_{3.6}\text{VOF}_5$  cryolite obtained from Rietveld refinement of SXRPD data.

Bond	Length (Å)	Bond	Length (Å)								
V		Na (2)									
F(1)	1.927(2) (x2)	F(1)	2.336(4) (x1)								
F(2)	1.922(3) (x2)		2.664(4) (x1)								
F(3)	1.912(2) (x2)		2.851(4) (x1)								
		F(2)	2.449(3) (x1)								
Na(1)			2.330(3) (x1)								
F(1)	2.232(2) (x2)	F(3)	2.358(4) (x1)								
F(2)	2.230(3) (x2)		2.717(4) (x1)								
F(3)	2.201(2) (x2)		2.765(5) (x1)								
		<table border="1"> <thead> <tr> <th>Bond</th> <th>Angle (°)</th> </tr> </thead> <tbody> <tr> <td>F(1)-V-F(1)</td> <td>180.0(2)</td> </tr> <tr> <td>F(1)-V-(F2)</td> <td>89.3(2)</td> </tr> <tr> <td>F(1)-V-F(3)</td> <td>90.8(2)</td> </tr> </tbody> </table>		Bond	Angle (°)	F(1)-V-F(1)	180.0(2)	F(1)-V-(F2)	89.3(2)	F(1)-V-F(3)	90.8(2)
Bond	Angle (°)										
F(1)-V-F(1)	180.0(2)										
F(1)-V-(F2)	89.3(2)										
F(1)-V-F(3)	90.8(2)										



#### 4.4. Na<sub>5-δ</sub>V<sub>3</sub>F<sub>14</sub>

##### 4.4.1. Chemical analysis and microstructural characterization

The as prepared solid, exhibits a powder XRPD pattern consistent with a chiolite structural type and consists of crystals with a well- defined morphology and average particle size of ca.13  $\mu\text{m}$ , as illustrated in Figure 4.8. While the simultaneous presence and homogeneous distribution of sodium, vanadium and fluorine was ascertained by EDX, the sample seems to contain very little amount of oxygen, if any (see chemical mapping shown in Figure 4.8b).

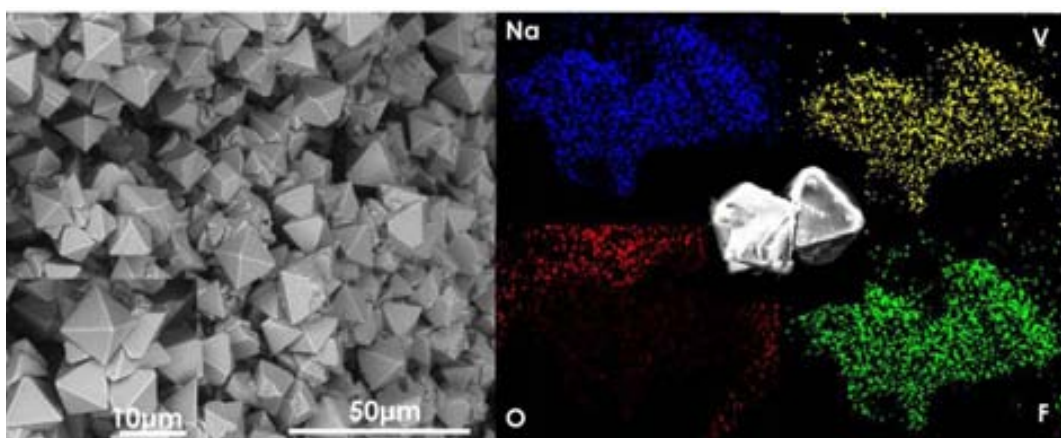


Figure 4.8. a) SEM images at different magnifications together with b) chemical mapping (EDX) for the as prepared chiolite.

The Na:V ratio was determined by chemical analysis, that yielded 28.60% ( $\sigma=0.05$ ) of vanadium, expressed in % wt., in full agreement with the expected value (28.6%) and 19.00% ( $\sigma=0.17$ ) of sodium. The measured sodium content represents a deviation of ca. 2.6% wt. from the expected value (21.5%) and translates into the sodium to vanadium ratio being 4.4 to 3 instead of 5 to 3. The IR spectrum does not exhibit any band in the 1000- 3800  $\text{cm}^{-1}$  and thus absence of adsorbed or crystallization of H<sub>2</sub>O molecules in the sample is inferred. Considering the absence of oxygen in the sample, the following empirical formula can be deduced from chemical analysis assuming that no anion vacancies are present in the sample: Na<sub>5- $\delta$</sub> V<sub>3</sub>F<sub>14</sub> with  $\delta\sim 0.6$  and a tentative oxidation state of 3.2 for vanadium.

Magnetic measurements were performed to estimate vanadium oxidation state and confirm the validity of the above mentioned assumptions. Figure 4.9 depicts the inverse of the susceptibility vs temperature, measured at 100 Oe which points at some type of magnetic ordering being achieved at about 25K, tentatively assigned to ferromagnetic ordering of vanadium ions as reported for  $K_5V_3F_{14}$ . [4] In the paramagnetic region (above the ordering temperature), the susceptibility slightly deviates from the Curie-Weiss behavior and hence the effective paramagnetic moment cannot be clearly determined, as also reported for  $K_5V_3F_{14}$ . [169] The value of the effective paramagnetic moment obtained as a function of the temperature from the point to point slope of the inverse susceptibility curve is also depicted in Figure 4.9. This effective moment varies slightly with temperature but can be estimated to be between 4.55 and 5.05  $\mu_B$ /f.u. (between 2.63 and 2.92  $\mu_B$ /V ion) from the region where the influence of the ferrimagnetic transition disappears. This range is close to the expected value for  $V^{3+}$  (2.83  $\mu_B$ /V ion), while being consistent with a slight amount of  $V^{4+}$  and the proposed  $Na_{5-\delta}V_3F_{14}$  ( $\delta \sim 0.6$ ) empirical formula.

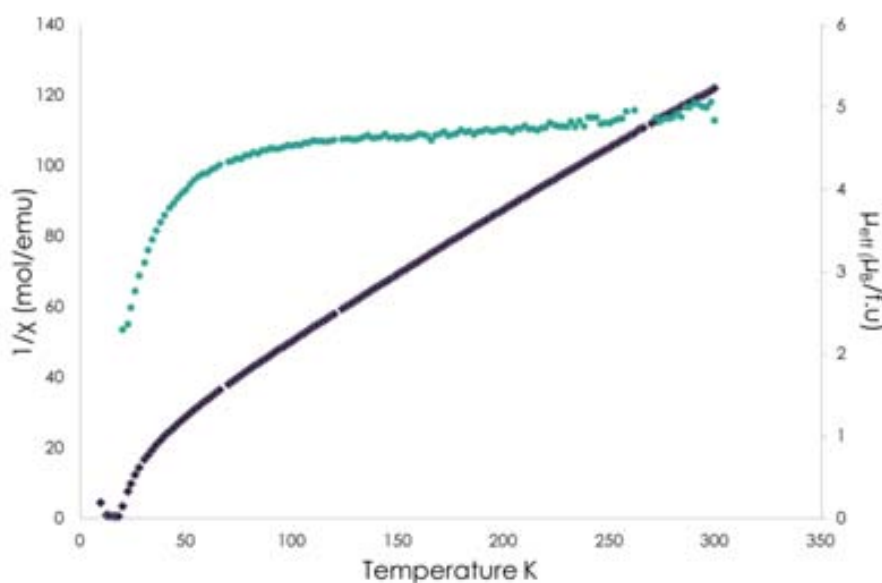


Figure 4.9. (Left axis) Inverse of the DC magnetic susceptibility at 100 Oe. (Right axis) temperature dependent effective paramagnetic moment obtained from the derivative of the inverse susceptibility.

With the aim to get further insight into the oxidation state of vanadium ions, X- ray absorption measurements were performed and compared to the XANES of vanadium references V<sub>2</sub>O<sub>5</sub>, VO<sub>2</sub>. The XANES spectra depicts pre- edge features and the main- absorption edge (while line). As mentioned in the previous section, information of the V coordination and oxidation state can be respectively deduced from the pre- edge and main- edge. In contrast to the high pre- edge intensity observed in V<sub>2</sub>O<sub>5</sub> with pyramidal square coordination and VO<sub>2</sub> with distorted octahedral coordination, the pre- edge intensity of the V chiolite is very small, as depicted in Figure 4.10.

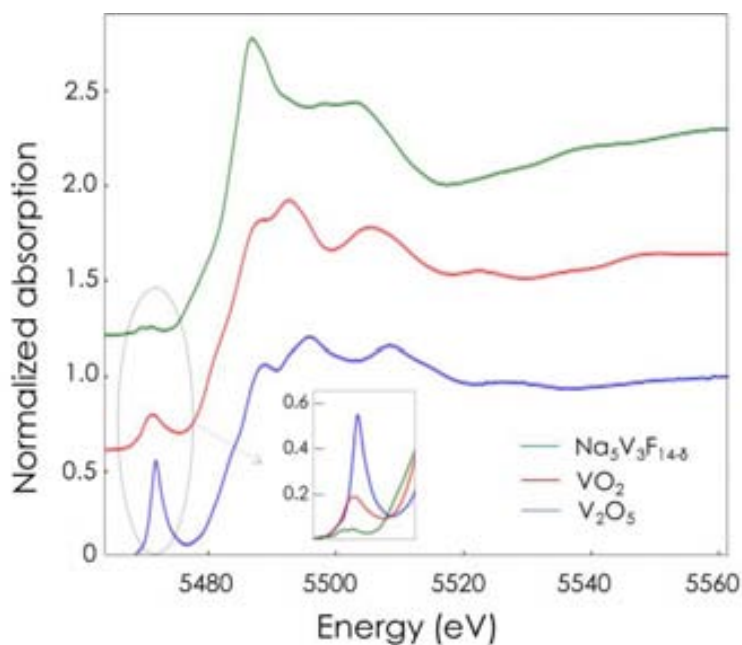


Figure 4.10. Normalized K- edge absorption spectra corresponding to chiolite Na<sub>5-δ</sub>V<sub>3</sub>F<sub>14</sub> (green), V<sub>2</sub>O<sub>5</sub> (blue) and VO<sub>2</sub> (red). The inset depicts superimposed pre- edge features for comparative purposes.

As the intensity of the pre- edge decreases with increasing the coordination symmetry of the absorbing metal, it is expected that the vanadium coordination environment in Na<sub>5-δ</sub>V<sub>3</sub>F<sub>14</sub> will be a regular or only slightly distorted octahedron. This is also in agreement with the similarity on the shape of the pre- edge features with a series of reported V compounds having more regular octahedral V coordination environments such as VO or V<sub>2</sub>O<sub>3</sub>. [161] The pre- edge

position of  $\text{Na}_{5.8}\text{V}_3\text{F}_{14}$  is shifted to lower energies as consequence of the decrease in the oxidation state of the absorbing metal and thus the vanadium oxidation state in  $\text{Na}_{5.8}\text{V}_3\text{F}_{14}$  seems to be lower than  $\text{V}^{4+}$ , which is in good agreement with the value of the effective magnetic moment measured. The vanadium oxidation state was estimated by measuring the mid-height of the normalized absorption edge of the sample and references, as done previously for  $\text{Na}_{3.6}\text{VOF}_5$ . A linear fitting of the energy positions were carried out which yields an approximate oxidation state of  $\text{V}^{3.5+}$ . In addition to the pre-edge contributions to the white line observed in all the vanadium compounds measured, the large amount of V-F bonds in the in the sample, more ionic than V-O bonds, could result in some overestimation in the vanadium oxidation state.[170]

Selected Area Electron Diffraction (SAED) was carried out in order to determine the crystallographic space group for  $\text{Na}_{5.8}\text{V}_3\text{F}_{14}$ . Although crystallites were found to decompose upon long exposure to the electron beam, minimizing the analysis time allowed reconstructing the reciprocal lattice of the compound taking a series of SAED patterns while rotating the crystallite around a selected reciprocal lattice row. Figure 4.11 a-c) exhibit the electron diffraction patterns along the [010], [0-11] and [-110] zone axes, respectively, which are consistent with an orthorhombic symmetry and  $Cc$  extinction symbol, compatible with  $Cmc2_1$  (n°. 36),  $Cmcm$  (n°. 63) and  $C2cm$  (n°. 40) space groups.

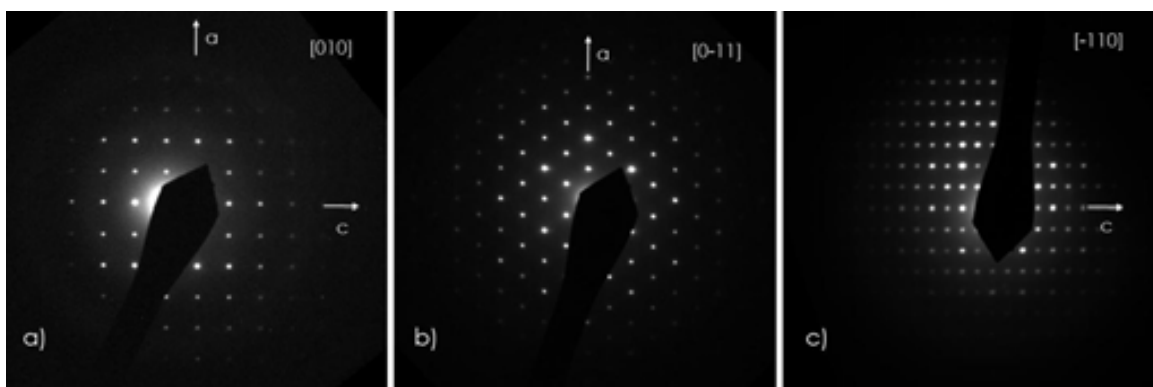


Figure 4.11. Electron diffraction patterns along the a) [010], b) [0-11] and c) [-110] zone axes.

A combined Rietveld refinement was carried out using neutron diffraction and synchrotron X-ray powder diffraction data (Figure 4.12) collected for the larger sample batch prepared.

The three space groups resulting from the electron diffraction study were considered for the refinement. While the attempts using *Cmcm* and *C2cm* were unsuccessful, the *Cmc21* space group rendered satisfactory agreement factors ( $\chi^2= 9.26$   $R_B= 4.70\%$  for synchrotron and  $R_B= 7.14\%$  for neutron data) with cell parameters  $a= 10.5482(2)$  Å,  $b= 10.4887(2)$  Å and  $c= 10.3243(1)$  Å. Bond distances obtained from the refinement are summarized in Table 4.2. Refinement of the occupation factors yields a total sodium content of 4.84(3) per formula unit, and some sodium deficiency in Na(2) and Na(1b) positions, the other sodium sites being fully occupied. Such values would be consistent with Na<sub>5-δ</sub>V<sub>3</sub>F<sub>14</sub> ( $\delta\sim 0.2$ ) and an oxidation state for vanadium of 3.1, which is roughly consistent with the results from chemical analysis. Atomic positions and bond lengths determined from the combined Rietveld refinement are presented in Tables 4.2 and 4.3.

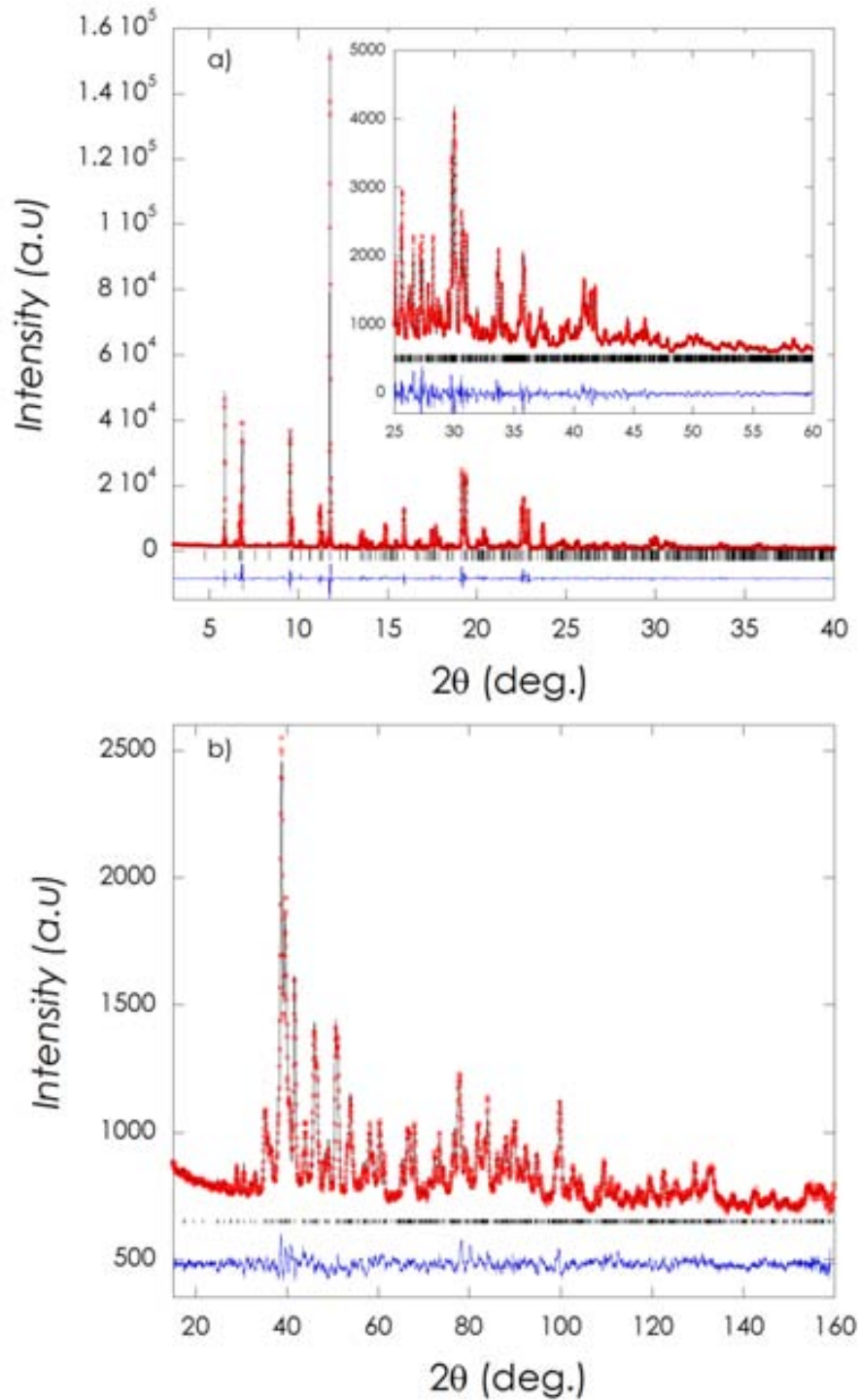


Figure 4.12. Rietveld refinement of  $\text{Na}_{5.8}\text{V}_3\text{F}_{14}$  using (above) synchrotron X-ray diffraction data and (below) neutron diffraction data. Experimental pattern (red dots), calculated profile (black continuous line) and difference pattern at the bottom (blue). Bragg positions are denoted by vertical bars.

Table 4.2. Atomic positions determined by Rietveld refinement.

Atom	Wyckoff Position	X	Y	Z
V1	4a	0	0.249(2)	-0.003(3)
V2	8b	0.250(2)	0.000(1)	0
Na2	8b	0.013(5)	0.761(3)	0.02089(156)
Na1a	4a	½	0.012(3)	0.228(4)
Na1b	4a	½	0.506(3)	0.274(4)
Na3	8b	0.240(2)	0.264(1)	0.252(4)
F1a	8b	0.380(2)	-0.122(2)	0.056(3)
F1b	8b	0.633(2)	0.365(2)	0.443(3)
F2a	8b	0.152(2)	-0.066(2)	0.137(3)
F2b	8b	0.864(2)	0.430(2)	0.370(3)
F3a	8b	0.331(2)	0.122(2)	0.109(3)
F3b	8b	0.659(2)	0.605(2)	0.386(3)
F4a	4a	0	-0.308(3)	0.326(4)
F4b	4a	0	0.199(4)	0.171(4)

Using the results of the refinement using SRXPD data, EXAFS analysis was carried out in order to estimate the V-F bond distances. Coordination shells of the two distinct vanadium ions were studied separately. The results obtained from fitting are given in Table 4.4, and are in good agreement with the values deduced from Rietveld refinements.

Table 4.3. Selected bond lengths resulting from combined Rietveld refinement of NPD and SXRPD data.

Bond		Length (Å)	Bond		Length (Å)
V (1)	V-F1a	1.93(2) (x2)	Na (1b)	Na-F1b	2.56(2) (x2)
	V-F1b	1.93(2) (x2)		Na-F2a	2.24(2) (x2)
	V-F4a	1.86(3) (x1)		Na-F3b	2.31(2) (x2)
	V-F4b	1.89(3) (x1)		Na-F4b	2.29(3) (x1)
				Na-F4a	3.35(3) (x1)
V (2)	V-F1a	1.97(2) (x1)	Na (2)	Na-F2a	2.68(2) (x2)
	V-F1b	1.98(1) (x1)		Na-F3a	2.44(2) (x2)
	V-F2a	1.90(2) (x1)		Na-F3b	2.63(2) (x2)
	V-F2b	1.92(2) (x1)		Na-F2b	2.96(2) (x2)
	V-F3a	1.88(2) (x1)		Na-F4a	3.25(2) (x2)
	V-F3b	1.90(2) (x1)	Na (3)	Na-F1a	2.50(2) (x1)
				Na-F1b	2.78(2) (x1)
				Na-F2a	2.43(2) (x1)
Na (1a)	Na-F1a	2.73(2) (x2)		Na-F2b	2.37(2) (x1)
	Na-F2b	2.25(2) (x2)		Na-F3a	2.34(2) (x1)
	Na-F3a	2.42(2) (x2)		Na-F3b	2.31(2) (x1)
	Na-F4a	2.13(3)(x1)		Na-F4b	2.71(1) (x1)
	Na-F4b	3.33(3)(x1)		Na-F4a	2.99(1) (x1)



Table 4.4. Bond distances and Debye- Waller factor determined with EXAFS analysis for the Na<sub>5-δ</sub>V<sub>3</sub>F<sub>14</sub> chiolite.

1 <sup>st</sup> shell	N	R(Å)	ΔR(Å)	σ <sup>2</sup> (Å <sup>-2</sup> )
V1-F1	2	2.026	0.062	0.003
V1-F2	2	1.936	0.062	0.003
V1-F3	2	1.894	0.062	0.003
V2-F1	2	1.913	0.042	0.0027
V2-F2	2	1.913	0.042	0.0027
V2-F3	2	1.871	0.042	0.0027

The distribution of anions around the two distinct V sites in the structure results in slightly distorted octahedral units with V(1)-F and V(2)-F distances varying from 1.86 to 1.93 Å and 1.88 to 1.98 Å respectively, in agreement with distances reported for different vanadium (oxy)fluorides and oxyfluorides.[27,41,42] Larger bonding distances are observed for fluoride ions in bridging position, as for chiolite K<sub>5</sub>V<sub>3</sub>F<sub>14</sub> and layered NaVF<sub>4</sub>. [7,43] V(1)-X1-V(2) are close to 145°, as typical in chiolite type structures. [2]

As reported above, sodium ions in Na(2) sites are placed in the intralayer positions with 8+2- coordination, with distances to anions ranging from 2.44 to 2.95 Å. Na(1a-b) and Na(3) occupy interlayer positions and are 7+1- and 8- coordinated, respectively, with bond distances ranging from 2.3 to 2.78 Å for Na(3). Na1(a-b) – F distances range from 2.13 to 2.73 Å with an additional longer distance to F(4a-b) (~3.3 Å). All such values are in good agreement with those observed for different sodium vanadium fluorides [27,4,44–46] and sodium transition metal fluoride-chiolites,[2,44,45].

VF<sub>6</sub> octahedra are rotated with respect to each other and non- centrosymmetric. An approximate estimation of octahedra rotation was grasped from a refinement of the structure using the centrosymmetric space group *Cmca*, which yields acceptable agreement parameters ( $\chi^2= 10.15$  R<sub>B</sub>= 5.30% for synchrotron and R<sub>B</sub>= 8.02% for neutron data). The results achieved indicate a rotation of V(1)X<sub>6</sub> octahedra of ca. 18° around (100) direction with the orientation of V(2)X<sub>6</sub> being the result of a first rotation around (1-10) of ~5°.

combined with a rotation of  $17^\circ$  around an axis that is close to (110) direction. Such values are close to those observed in  $\text{Na}_5\text{Al}_3\text{F}_{14}$  chiolite.

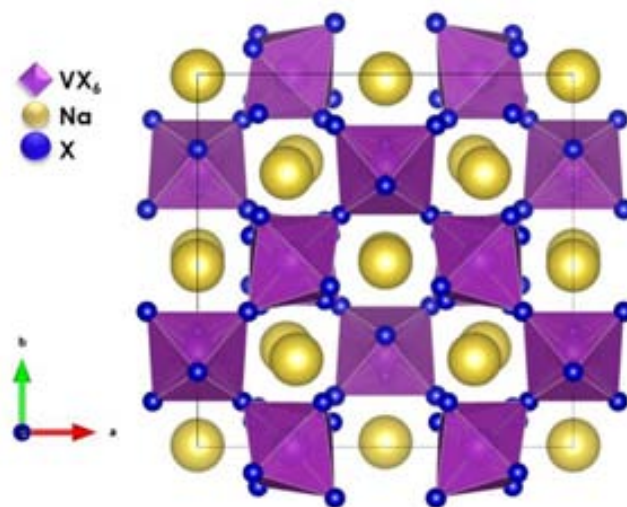


Figure 4.13. Crystal structure of  $\text{Na}_{5-8}\text{V}_3\text{F}_{14}$  along the  $c$ -axis.

As mentioned in Section 4.1, the solvothermal reaction carried out at  $200^\circ\text{C}$  in a water/ethylene glycol mixture yielded a sample consisting of a mixture of phases and containing blue crystals ( $<0.1\text{ mm}$ ) from which a well formed crystal with octahedral crystal habit and average size  $0.48 \times 0.42 \times 0.30\text{ mm}^3$  was selected. Careful inspection of the single crystal indicated that the color of the surface (blue) was somewhat different from that of the interior (yellowish). The crystal structure was deduced from least square refinement using 2536 reflections of single crystal diffraction data that converged to the chiolite structural model ( $R=0.1928$ ). It is worth noticing the high extinction effects shown by this crystal, usually related with a very low mosaicity, which would be reason of a poor final agreement factor.

The unit cell found corresponded to a tetragonal cell with parameters  $a=7.380(3)\text{ \AA}$ ,  $b=7.380(3)\text{ \AA}$  and  $c=10.381(11)\text{ \AA}$  and space group  $P4_22_12$  ( $n^\circ 94$ ) which is isomorphous to  $\gamma\text{-Na}_5\text{Fe}_3\text{F}_{14}$ . [171] Interestingly, this unit cell differs from that found for the orthorhombic chiolite  $\text{Na}_{5-6}\text{V}_3\text{F}_{14-5}$  ( $Cmc2_1$ ) prepared at  $100^\circ\text{C}$  and described above. This is most likely related to a difference in composition, which is easily understood from the different reaction medium and synthesis conditions for both compounds. In particular, the lower HF concentration used

may result in the obtention of an oxyfluoride instead of a fluoride, and thus charge compensation should involve either higher oxidation state of vanadium ions or the presence of a much larger amount of sodium vacancies in the structure. Detailed structural data is given in Table 4.5 while atomic coordinates and equivalent isotropic displacement parameters are shown in Table 4.6.

Selected bond distances obtained from BVS analyses are shown in Table 4.7. Vanadium occupies two distinct crystallographic positions and exhibits octahedral coordination with distances ranging from 1.79 to 1.93 Å for V(1) and 1.78 to 1.91 Å for V(2) and which are similar to that observed in VF<sub>4</sub>. [172] Moreover, such values are somehow (ca. 0.1 Å) shorter than those reported for the V<sup>3+</sup> chiolites K<sub>5</sub>V<sub>3</sub>F<sub>14</sub> [113] (V(1)= 1.903- 2.00 Å and V(2)= 1.920-.955 Å) and Na<sub>5-6</sub>V<sub>3</sub>F<sub>14-6</sub> (V(1)= 1.86- 1.93 Å and V(2)= 1.88- 1.97 Å), which points to a higher oxidation state of vanadium in the structure. Bond valence sum (BVS) analysis carried out using parameters implemented in FullPof\_Suite of programs resulted in an average valence for vanadium of 4.1, which allows to the following empirical formula: Na<sub>5</sub>V<sub>3</sub>O<sub>3</sub>F<sub>11</sub>. Pauling's second rule [1,2] was applied to the anionic positions of the crystal lattice in order to get a hint of the possibility of preferential occupation of some of them by either oxygen or fluorine. The bond strength sum (b) for each position resulted as follows: X1= 1.04, X2= 0.92, X3= 1.58, X4= 1.17. Such values point at the positions X1, X2 and X4 being preferentially occupied by F, and X3, which corresponds to a bridge position, being occupied by O.

Table 4.5. Crystallographic data for Na<sub>5</sub>V<sub>3</sub>O<sub>3</sub>F<sub>11</sub>.

FW (g mol <sup>-1</sup> )	536.36
$\lambda$ (Å)	0.71073
Crystal system	Tetragonal
Space group	P 42 21 2
$a$ (Å)	$a = 7.380(3)$
$b$ (Å)	$b = 7.380(3)$
$c$ (Å)	$c = 10.381(11)$
$V$ (Å <sup>-3</sup> )	565.4(8)
$Z$	8
$\rho_{\text{calc}}$ (g cm <sup>-3</sup> )	3.030
$\mu$ (mm <sup>-1</sup> )	2.755
Data / restraints / parameters	560 / 0 / 54
GOF on F <sup>2</sup>	2.370
R <sub>i</sub> [ $I > 2\sigma(I)$ ]	0.1928
wR <sub>2</sub> (all data)	0.5101
Max, min $\Delta\rho_{\text{electron}}$ (e Å <sup>-3</sup> )	6.318 / -1.288

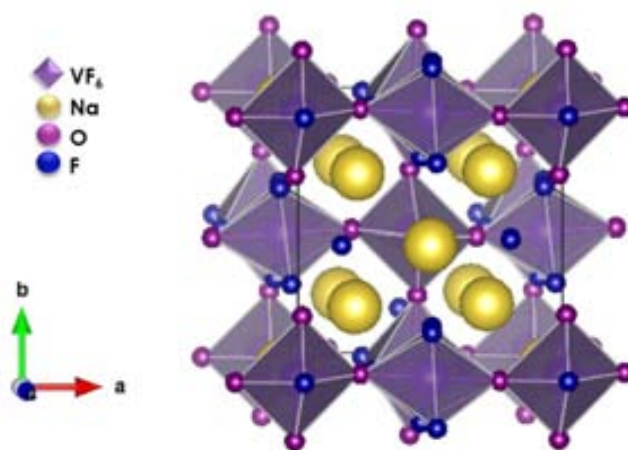
Table 4.6. Atomic coordinates ( $\times 10^4$ ) and equivalent isotropic displacement parameters ( $\text{\AA}^2 \times 10^3$ ) for Na<sub>5</sub>V<sub>3</sub>O<sub>3</sub>F<sub>11</sub>.

Atom	X	Y	Z	U(eq)
V(1)	0	5000	5011(2)	54(4)
V(2)	0	0	0	61(4)
Na(1)	2537(11)	7442(12)	2524(4)	57(6)
Na(2)	0	0	5000	43(6)
X(1)	220(50)	3190(30)	6150(30)	240(19)
X(2)	-100(50)	3180(30)	3760(30)	174(12)
X(3)	- 2600(30)	4840(30)	5100(20)	210(30)
X(4)	0	10000	1840(30)	150(20)

Na(1) is placed in the interlayer position with 8- coordination and bond distances ranging from 2.23 to 3.00 Å, while Na(2) occupies the intra-layer position also having 8- coordination and distances of 2.65 to 2.68 Å, as reported for  $\gamma$ - Na<sub>5</sub>Fe<sub>3</sub>F<sub>14</sub>. [171] Na- X bond distances are in good agreement to the values observed in Na- containing chiolites such as Na<sub>5</sub>Al<sub>3</sub>F<sub>14</sub>, [173] Na<sub>5-6</sub>V<sub>3</sub>F<sub>14-6</sub>. The crystal structure obtained for the single crystal is depicted in Figure 4.14.

Table 4.7. Selected bond distances for  $\text{Na}_5\text{V}_3\text{O}_3\text{F}_{11}$ .

Bond	Length (Å)	Bond	Length (Å)
V (1)		Na (1)	
V-X1	1.792(2) (x2)	Na-X1	2.24(2) (x1)
V-X2	1.872(17) (x2)	Na-X1	2.52(5) (x1)
V-X3	1.93(2) (x1)	Na-X2	2.26(3)(x1)
		Na-X2	2.37(4)(x1)
V (2)		Na-X3	3.00(3) (x1)
V-X3	1.78(3) (x4)	Na-X3	3.15(3) (x1)
V-X4	1.91(3) (x2)	Na-X4	2.644(10) (x1)
		Na-X4	2.752(10)(x1)
		Na (2)	
		Na-X1	2.65(3) (x4)
		Na-X1	2.68(3) (x4)

Figure 4.14. Crystal structure of chiolite  $\text{Na}_5\text{V}_3\text{O}_3\text{F}_{11}$ . (P1212 space group).

#### 4.5. Electrochemical characterization

The electrochemical performance of the above described compounds were tested vs Na<sup>o</sup> counter electrodes at C/25 and using 1M NaClO<sub>4</sub> in EC: PC as electrolyte. The working electrodes consisted of simple mixtures of the corresponding vanadium (oxy)fluoride with 40% of SP carbon after 12h ball-milling.

The potential vs. capacity profile for NaVF<sub>4</sub> is shown in Figure 4.14a, and exhibits close similarities to those obtained when testing the sodium manganese (oxy)fluorides (see Chapter 3). The electrochemical activity, if any, is only observed above 4V, with large polarization and limited reversibility. Reversible capacities observed for NaVF<sub>4</sub> (ca. 100 mAh/g) are ca. 30 mAh/g larger than that of SP carbon. As in the case of the manganese containing compounds, such electrolyte decomposition at lower potentials than observed towards inert working electrodes[67] can be attributed to a possible catalytic effect of the agglomerates of NaVF<sub>4</sub> and SP carbon. Similar results were obtained when testing the electrochemical performance of Na<sub>5-δ</sub>V<sub>3</sub>F<sub>14</sub> chiolite and Na<sub>3-δ</sub>VOF<sub>5</sub> cryolite, for which the intercalation of Na<sup>+</sup> is expected to take place with the concomitant oxidation/reduction of V<sup>3+</sup>/ V<sup>4+</sup> and V<sup>4+</sup>/ V<sup>5+</sup> redox couples, respectively, and thus, a priori different oxidation potentials are expected. Experiments with a potential cut off higher than 4.5V resulted in the observation of a large mostly irreversible plateau around 4.5 V, attributed to the oxidation of the electrolyte. Lowering of the cut off potential resulted in very low capacity values and large cell polarization.

Further attempts were carried out using 1M NaClO<sub>4</sub> in EMS: PC as electrolyte, given the larger operating window potential upon oxidation obtained for the sulfone (see Chapter 2). Nonetheless, similar results were obtained. Overall, and as in the case of manganese fluorides, it should be concluded that the electrochemical activity of the prepared vanadium oxy(fluorides) upon oxidation (sodium de-intercalation) is negligible, if any, in the stability range of the electrolyte. Such conclusion was also confirmed with *in situ* XRPD measurements of Na<sub>3-δ</sub>VOF<sub>5</sub> sample, where no changes in the diffraction patterns were observed upon electrochemical testing, in line with the results achieved for the manganese containing samples (Chapter 3).

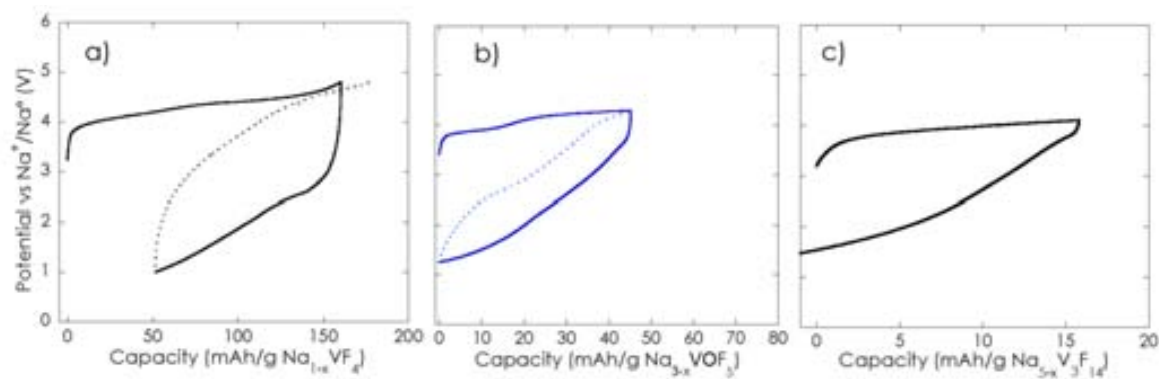


Figure 4.14. Potential vs capacity profile for a)  $\text{NaVF}_4$ , b)  $\text{Na}_{3.6}\text{VOF}_5$  and  $\text{Na}_{5.6}\text{V}_3\text{F}_{14}$  tested V at C/25 in 1M  $\text{NaClO}_4$  in EC: PC, starting upon oxidation.

Since lowering the potential below the initial open circuit potential (OCP) in the above mentioned experiments allowed to recover some capacity, electrochemical tests upon reduction (sodium intercalation) were also carried out. If the absence of electrochemical activity is related to a too high  $\text{V}^{+4}/\text{V}^{+3}$  or  $\text{V}^{+5}/\text{V}^{+4}$  potential, we expected that the  $\text{V}^{+3}/\text{V}^{+2}$  or  $\text{V}^{+3}/\text{V}^{+4}$  may be observed. Although the amount of sodium vacancies in the crystal structures of the compounds under investigation is low, if any, a possible phase transition to another structural type allowing the presence of more sodium atoms could *a priori* not be excluded. Thus, the electrochemical performances of  $\text{NaVF}_4$ ,  $\text{Na}_{5.6}\text{V}_3\text{F}_{14}$  and  $\text{Na}_{3.6}\text{VOF}_5$  were tested upon reduction from open circuit potential (OCP) to 0.1 V using 1M  $\text{NaClO}_4$  in EC: PC as electrolyte at C/25. Typical potential vs. capacity profiles achieved are depicted in Figure 4.15.



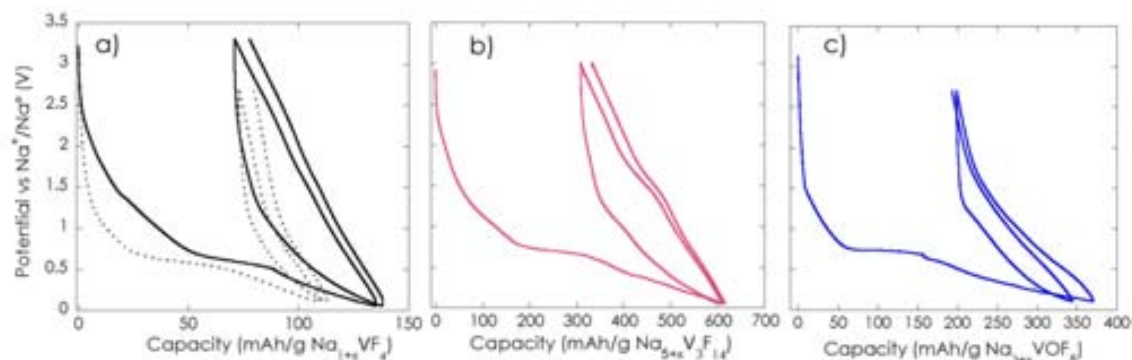


Figure 4.15. Potential vs capacity profile for a)  $\text{NaVF}_4$ , b)  $\text{Na}_{5-6}\text{V}_3\text{F}_{14}$  and c)  $\text{Na}_{3-6}\text{VOF}_5$  cycled upon reduction between OCP to 0.1 V at C/25 in 1M  $\text{NaClO}_4$  in EC: PC.

First, an irreversible pseudoplateau is observed around 0.6 V vs.  $\text{Na}^+/\text{Na}^0$ , which is attributed to parasitic decomposition of the electrolyte on the surface of SP carbon (see dotted line in Figure 4.15 corresponding to a blank experiment with the working electrode containing only carbon). Upon further reduction, a change in the slope of the pseudo-plateau is observed, which could be related to the insertion of  $\text{Na}^+$  into the (oxy)fluoride framework or to a possible conversion reaction with the concomitant reduction of the corresponding V ion. Yet, as the electrochemical profile is in all cases similar to that of SP carbon, and reaction at very similar potential is observed for the three cases even if different redox couples are observed, we are again forced to conclude that there is no significant electrochemical activity of the compounds themselves.

# CHAPTER 5:

## Study of the Na-Ti-(O,F) system

*Synthesis,*

*Crystal chemistry,*

*Electrochemical characterization of:*

*$\text{Na}_5\text{Ti}_3\text{O}_3\text{F}_{11}$ ,  $\text{Na}_2\text{Ti}_2\text{O}_3\text{F}_4$  and  $\text{Na}_2\text{Ti}_3\text{O}_7$*

### 5.1. Chiolite- type: Na<sub>5-δ</sub>Ti<sub>3</sub>O<sub>3-δ</sub>F<sub>11+δ</sub>

The synthesis of sodium titanium oxyfluorides was attempted by microwave- assisted methods, following the recent reports on the preparation of titanium (oxy)fluorides by means of this synthetic route (Section 1.2). A titanium containing phase with chiolite-type structure was obtained as follows: 6.0 g of H<sub>2</sub>TiF<sub>6</sub> (21.6x10<sup>-3</sup>mol) were dissolved in a saturated aqueous solution of sodium acetate prepared at room temperature in a 100 mL PTFE beaker and heated in a domestic microwave oven (LG Intellowave, 2.45GHz) at 800W power for 20 s. This procedure was repeated several times (total reaction time 3 min) with intermediate two-minute resting periods to limit the temperature increase. Due to the high MW absorbing capacity of the used precursors, no susceptor to provide indirect heating was necessary. The white solid formed was centrifuged and washed several times with water and dried in air at 60°C.

#### 5.1.1. Chemical analysis and microstructural characterization

The as prepared compound exhibits an XRD pattern typical of chiolite type compounds and consists of several micron- sized agglomerates of spherical nanoparticles (ca. 380 nm average size). The simultaneous presence of sodium, titanium, oxygen and fluorine in the sample was ascertained by EDX (see Figure 5.1). Chemical mapping indicates a homogeneous distribution of the four elements within the particles with the F: O ratio being roughly 1.4.

The IR spectrum of the sample does not exhibit any band in the 1000- 3800 cm<sup>-1</sup> range where stretching and bending vibrations of H<sub>2</sub>O nor H<sub>3</sub>O<sup>+</sup> would appear, which indicates absence of structural water molecules. Chemical analysis yielded 19.7 (σ=0.13) and 26.1 (σ=0.17) weight % contents for sodium and titanium. Such values are consistent with the expected titanium content and a slight sodium deficiency (22.2%) towards the theoretical value (27.9%). Since titanium is expected to be in Ti(IV) oxidation state (no reduction can be expected from the synthesis route used and the sample is white) the following empirical formula can be deduced from chemical analysis assuming that no anion vacancies are present in the sample: Na<sub>5-δ</sub>Ti<sub>3</sub>O<sub>3-δ</sub>F<sub>11+δ</sub> with δ~0.3.

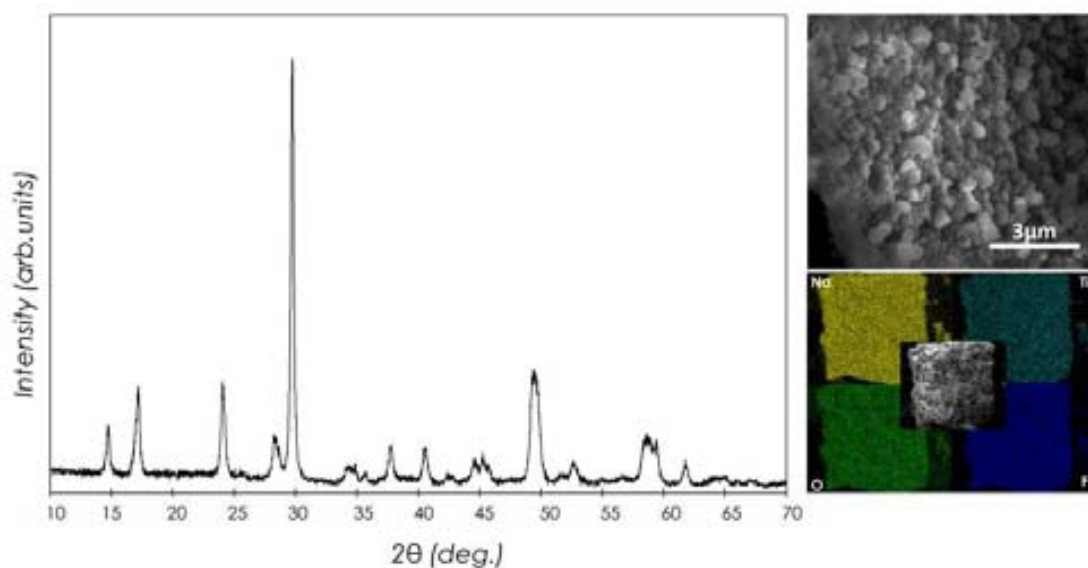


Figure 5.1. a) SEM image and EDX mapping and b) XRPD pattern corresponding to  $\text{Na}_{5.6}\text{Ti}_3\text{O}_3\text{F}_{11}$  prepared by a microwave assisted method.

Elucidation of the space group through electron diffraction was prevented by the too small crystallite size and high agglomeration. A previous report by *Grannec et al.* exists on a sample formulated as  $\text{Na}_5\text{Ti}_3\text{O}_3\text{F}_{11}$  and described with a monoclinic cell (with  $b$  the unique axis) in which  $a$ - and  $c$ - lattice parameters are identical. Nonetheless, from a crystallographic point of view a more symmetric B centered orthorhombic cell should be considered with  $a$ - and  $c$ - as the semi-diagonals of a rectangle. Following the settings previously given for  $\text{BaSr}_4\text{U}_3\text{O}_{14}$  and  $\text{Ca}_5\text{Te}_3\text{O}_{14}$  [28,174], the cell parameters for the structure were renamed to be C centered. Thus, the powder XRD pattern was indexed in the orthorhombic crystal system with cell parameters:  $a = 10.496(2) \text{ \AA}$ ,  $b = 10.398(2) \text{ \AA}$ , and  $c = 10.2914 \text{ \AA}$ . Monoclinic cell parameters are related to our orthorhombic settings by  $a_m = c_m = ((\frac{1}{2}a_o)^2 + (\frac{1}{2}b_o)^2)^{\frac{1}{2}}$ ,  $c_m \approx b_o$ , and  $\beta_m = 2\text{tg}(a_o/b_o)$ . Systematic absences are compatible with  $Cmca$  (n° 64) space group.

A Rietveld refinement was carried out using SXPDP data collected at ALBA synchrotron ( $\lambda = 0.61988 \text{ \AA}$ ). The initial structural model considered was  $\text{Ca}_5\text{Te}_3\text{O}_{14}$ , [174] with sodium and titanium occupying calcium and tellurium sites, respectively, and fluorine and oxygen equally distributed in oxygen positions. The results confirm the validity of the model

(agreement factors  $\chi^2=1.53$  and  $R_b= 5.5\%$ ). As chemical analysis points at a possible sodium deficiency in the sample, the occupation of sodium sites was also refined. Nonetheless, no significant amount of sodium vacancies was detected (Figure 5.2). Thus, we are forced to conclude that the sodium deficiency in the sample may be negligible and that the values resulting by chemical analysis could be affected by some error derived from a slight amount of secondary titanium containing phase not detected by XRD.

Table 5.1 shows the refined atomic parameters while selected bond lengths are shown in Table 5.2. Ti- X and Na-X (X=O,F) bond distances are consistent with values expected from Shannon's radii.[175] Titanium presents 6-coordination with Ti-X distances varying from 1.86 to 2.00 Å that compare well with distances observed in TiOF<sub>2</sub> [176] (Ti-X=1.9 Å) where all the anions are in bridging positions, and with Ti-O distances observed for Ti<sup>4+</sup>oxides with related structures.[177–180] Moreover, Ti(1-2) bond distances to X(2-4) terminal anions oscillate between 1.9 and 2.0 Å while Ti(1-2) bond distances to X(1) bridging positions range between 1.86 and 1.95 Å, in good agreement with values reported for (H<sub>3</sub>O<sup>+</sup>)<sub>2/3</sub>TiO<sub>4/3</sub>F.[51] The Ti(1)-X1-Ti(2) angle is close to 150° in agreement with typical values reported for M(1)-X-M(2) angles in chiolite type structures being close to 150°.[21] Na-X distances range from 2.1 to 2.9 Å, similar to those observed in sodium titanium oxides and fluorides such as Na<sub>2</sub>Ti<sub>3</sub>O<sub>7</sub>, Na<sub>2</sub>Ti<sub>6</sub>O<sub>13</sub>; or Na<sub>2</sub>TiF<sub>6</sub>. [181] Na(2) occupies the intralayer position with 8+2- coordination to four X(2) and four (X3) terminal anions (respective bond distances 2.4 and 2.8 Å) and two X(4) (bond distances 3.28 Å). Na(1) and Na(3) are sitting in the interlayer positions with 7+1- and 8-coordination, respectively. Na(1)-X(1-4) bond distances range from 2.2 to 2.7 Å, with an additional Na(1)-X(4) bond distance of 3.2 Å. The coordination around Na(3) exhibits four shorter distances of ~2.3 Å to (X2-3), two intermediate 2.7Å distances to bridging X(1) and two longer 2.8 Å distances to X(4).

The determined anionic positions allow the calculation of octahedral rotations around different directions in the unit cell, which gives an idea of the distortion degree in the structure. Ti(1)X<sub>6</sub> octahedra is rotated about 15° around (100) direction while Ti(2)X<sub>6</sub> orientation results from a combination of two rotations: a first rotation of about 4° around (1-10) direction and a second of ~15° around an axis that is near (110) direction. Similar

rotations are observed in chiolite  $\text{Na}_5\text{Al}_3\text{F}_{14}$  where Al(1) and Al(2) are rotated about  $14^\circ$  around the (001) direction as well as in  $\text{Na}_{5-\delta}\text{V}_3\text{F}_{14}$  with a rotation of  $17^\circ$  around (110) direction, as reported in Chapter 4. .

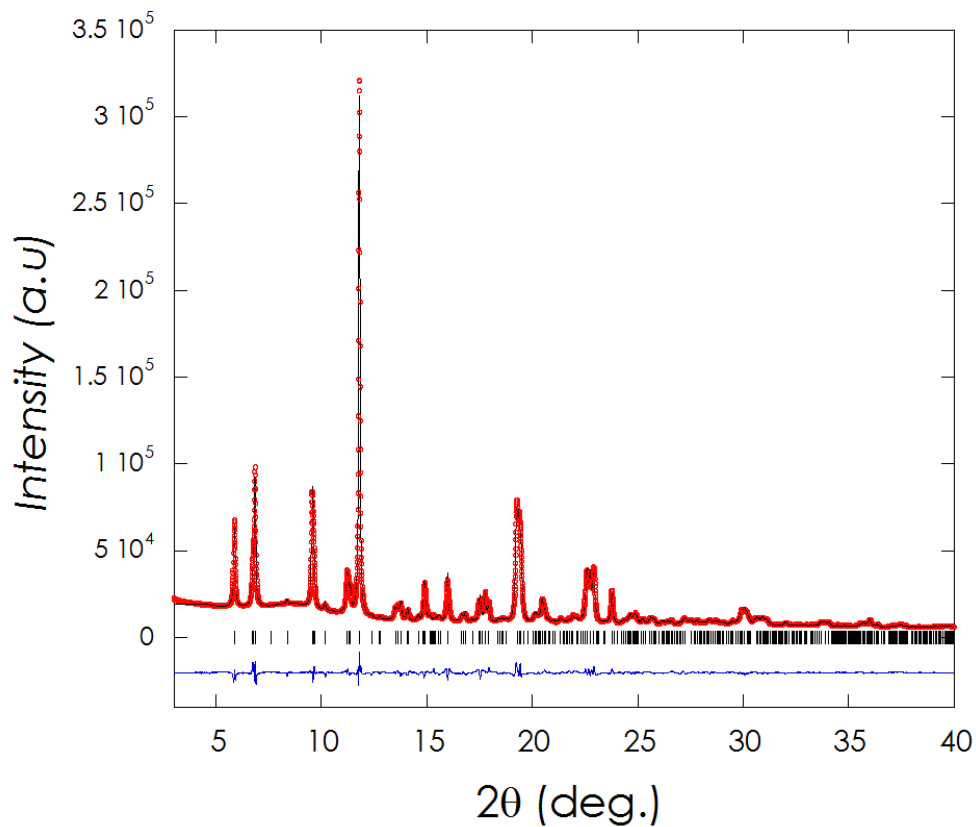


Figure 5.2. Synchrotron XRPD showing the Rietveld refinement of  $\text{Na}_{5-\delta}\text{Ti}_3\text{O}_{3-\delta}\text{F}_{11+\delta}$ . The experimental pattern is shown in red dots, the calculated profile in black continuous line and difference pattern at the bottom in blue. Bragg positions are denoted by vertical bars.

Table 5.1. Atomic positions determined from Rietveld refinement. Anions (F and O) are commonly denoted as X. ( $\chi^2=1.53$  and  $R_B=5.5\%$ ).

Atom	Wyck. Pos.	X	Y	Z
Ti(1)	4b	$\frac{1}{2}$	0	0
Ti(2)	8c	$\frac{1}{4}$	$\frac{1}{4}$	0
Na(2)	4 <sup>a</sup>	0	0	0
Na(1)	8f	$\frac{1}{2}$	0.255(4)	0.223(2)
Na(3)	8e	$\frac{1}{4}$	0.515(4)	$\frac{1}{4}$
X(1)	16g	0.369(4)	0.125(4)	0.047(3)
X(2)	16g	0.147(3)	0.178(2)	0.136(3)
X(3)	16g	0.341(2)	0.374(3)	0.113(2)
X(4)	8f	0	-0.053(3)	0.314(4)

Table 5.2. Selected bond lengths obtained from Rietveld refinement of XRPD data. ( $\chi^2=1.53$  and  $R_B=5.5\%$ ).

Bond	Length (Å)	Bond	Length (Å)
<i>Ti(1)</i>		<i>Na (2)</i>	
Ti-X1	1.95(2) (x4)	Na-X2	2.42(2) (x4)
Ti-X4	1.99(2) (x2)	Na-X3	2.78(2) (x4)
<i>Ti(2)</i>		Na-X4	3.28(2) (x2)
Ti-X1	1.86(2) (x2)	<i>Na (3)</i>	
Ti-X2	1.92(2) (x2)	Na-X1	2.69(2) (x2)
Ti-X3	1.98(2) (x2)	Na-X2	2.33(2) (x2)
<i>Na (1)</i>		Na-X3	2.25(2) (x2)
Na-X1	2.65(2) (x2)	Na-X4	2.80(3) (x2)
Na-X2	2.27(2) (x2)		
Na-X3	2.37(2) (x2)		
Na-X4	2.20(2) (x1)		
Na-X4	3.22(2) (x1)		



In order to estimate the probability of an ordered distribution of oxygen and fluorine in the structure, Pauling's second rule was considered.[6,147] X1 occupies a bridging position coordinated to two Ti (1-2), one Na (3) and one Na (1) which results in a bond strength sum of  $b = 1.6$  that points to this position tending to be preferentially occupied by oxygen. In contrast, X2 to X4 terminal positions would tend to be preferentially occupied by fluorine ( $b = 1.1$ ), as depicted in Figure 5.3.

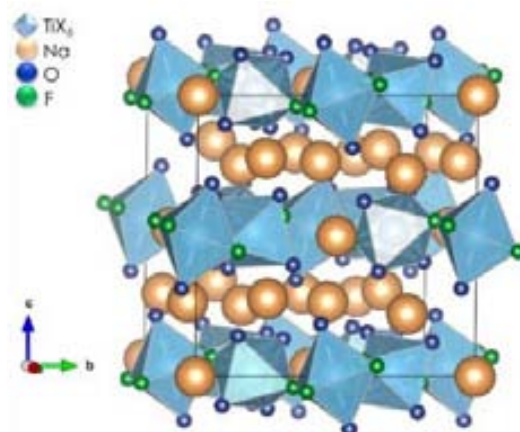


Figure 5.3. Structure of Na<sub>5-8</sub>Ti<sub>3</sub>O<sub>3-8</sub>F<sub>11+8</sub> along c- axis with tentative distribution of O and F as deduced from Pauling's second rule.

### 5.2.2. Electrochemical characterization

As titanium cannot be oxidized beyond Ti<sup>4+</sup>, electrochemical testing of Na<sub>5-8</sub>Ti<sub>3</sub>O<sub>3-8</sub>F<sub>11+8</sub> was carried out only upon reduction and thus attempting possible intercalation of additional sodium ions in the interlayer space, as previously reported for Na<sub>2</sub>Ti<sub>3</sub>O<sub>7</sub>. [107] While the first reduction with a capacity close to 270 mAhg<sup>-1</sup>, the reversible capacity after the first oxidation is only 60 mAhg<sup>-1</sup> and an electrochemical profile similar to that achieved for the SP carbon blank electrode is observed. The larger capacity observed upon the first reduction may be attributed to either an irreversible conversion reaction (it has been reported to take place for TiF<sub>3</sub> at ca. 1V vs. Li<sup>+</sup>/Li) [182] or to reactivity of the electrode with the electrolyte. Such results seem to indicate that no additional sodium intercalation in the phase takes place, most likely due to the absence of vacant suitable crystal sites and that the electrochemical activity of Na<sub>5-8</sub>Ti<sub>3</sub>O<sub>3-8</sub>F<sub>11+8</sub>, if any, does not involve any reversible processes.

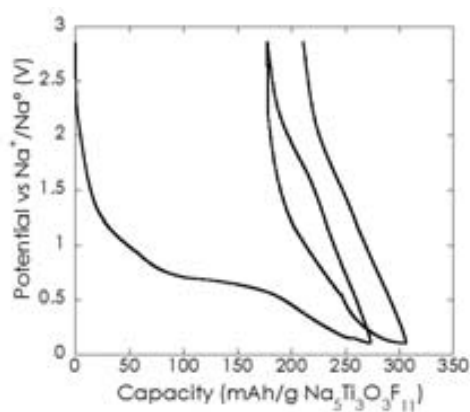


Figure 5.4. Potential vs capacity profile of  $\text{Na}_{5-\delta}\text{Ti}_3\text{O}_{3-\delta}\text{F}_{11+\delta}$  cycled vs  $\text{Na}^+$  at C/25 in 1 M  $\text{NaClO}_4$  in EC: PC.

## 5.2. Studies on stability and redox mechanism $\text{Na}_2\text{Ti}_3\text{O}_7$

### 5.2.1. Synthesis of $\text{Na}_2\text{Ti}_3\text{O}_7$

The synthesis of  $\text{Na}_2\text{Ti}_3\text{O}_7$  was carried out via solid state reaction at 800 °C for 40h using anatase  $\text{TiO}_2$  and anhydrous  $\text{Na}_2\text{CO}_3$  (in 10% excess) as precursors. The resulting sample was found to be pure and consisted of irregularly shaped particles of 1-3  $\mu\text{m}$  size. Figure 5.5 depicts the XRPD pattern of the as prepared sample.

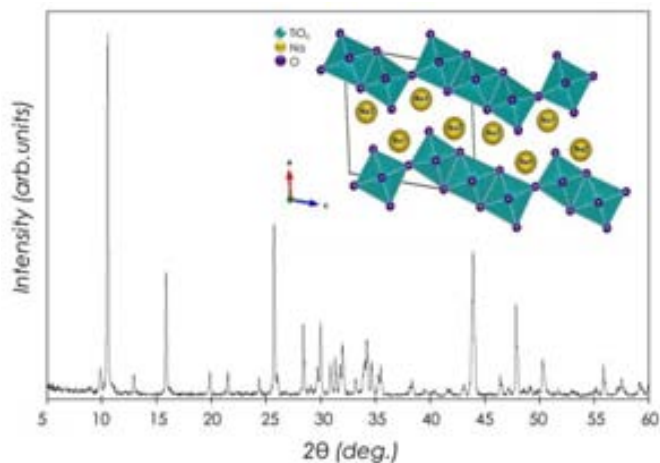


Figure. 5.5. XRPD pattern of  $\text{Na}_2\text{Ti}_3\text{O}_7$  prepared by solid state reaction. Its crystal structure is shown as an inset.

$\text{Na}_2\text{Ti}_3\text{O}_7$  crystallizes in the monoclinic system with  $P2_1/m$  space group and cell parameters  $a = 8.5642(3)$  Å,  $b = 3.8012(1)$  Å and  $c = 9.1265(3)$  Å, and  $\beta = 101.598(2)^\circ$ . Its crystal framework consists of  $\text{TiO}_6$  octahedra linked by edges, forming zig-zag  $3 \times 2 \times \infty$  ribbons.[180] These ribbons are connected via vertices and stacked to form a layered structure. Sodium ions are located between the layers occupying two different crystallographic positions Na(1) and Na(2) (2e Wyckoff positions) that are 9- and 7-coordinated to oxygen atoms, respectively. A scheme of the crystal structure is depicted in Figure 5.5 (inset). This compound can reversibly intercalate-deintercalate 2 mol of sodium ions (177 mAh/g) at a surprisingly low average potential (0.3 V vs  $\text{Na}^+/\text{Na}$ ) concomitant to the reduction of 2/3 of  $\text{Ti}^{+4}$  to  $\text{Ti}^{+3}$ . [107] Even if this electrochemical capacity is by no means low, it is smaller than that exhibited by other negative electrode materials such as hard carbon or alloy based materials. [78,183,184]

A plausible approach to enhance the electrochemical capacity would be to generate sodium vacancies in the crystal lattice through substitution of oxygen by fluorine to yield  $\text{Na}_{2-x}\text{Ti}_3\text{O}_{7-x}\text{F}_x$ . Indeed, for  $x=1$ , the full reduction of  $\text{Ti}^{+4}$  to  $\text{Ti}^{+3}$  could be envisaged, concomitant to intercalation of 3 mol of sodium atoms in the structure, which would result in an electrochemical capacity of 266 mAh/g.

Different attempts to prepare  $\text{Na}_{2-x}\text{Ti}_3\text{O}_{7-x}\text{F}_x$  by direct synthesis were unsuccessful and thus, thermal treatment of  $\text{Na}_2\text{Ti}_3\text{O}_7$  with a fluorinating agent (polyvinylidene fluoride (PVDF)) was attempted. This method has allowed the preparation of a variety of oxyfluorides such as  $\text{Sr}_2\text{TiO}_3\text{F}_2$ , [185]  $\text{CaCuO}_2\text{F}_2$  [185] and  $\text{Sr}_x\text{Ba}_{1-x}\text{FeO}_2\text{F}$  [186–188] by calcination of the alkali earth-containing oxide with stoichiometric amounts of PVDF (in 5% excess) at 400 °C for 12h.

$\text{Na}_2\text{Ti}_3\text{O}_7$  and PVDF with the suitable stoichiometric ratio to yield  $\text{NaTi}_3\text{O}_6\text{F}$  with an additional 10% excess of PVDF were ball-milled at 350 rpm for 0.5 h, and further treated at 350 °C for different time periods between 8 and 12 h under air flow. Unfortunately all such attempts led to the formation of a mixture of phases containing  $\text{Na}_2\text{Ti}_3\text{O}_7$ ,  $\text{Na}_2\text{Ti}_6\text{O}_{13}$  and  $\text{Na}_3\text{TiOF}_5$ , as deduced from XRPD (Figure 5.6).

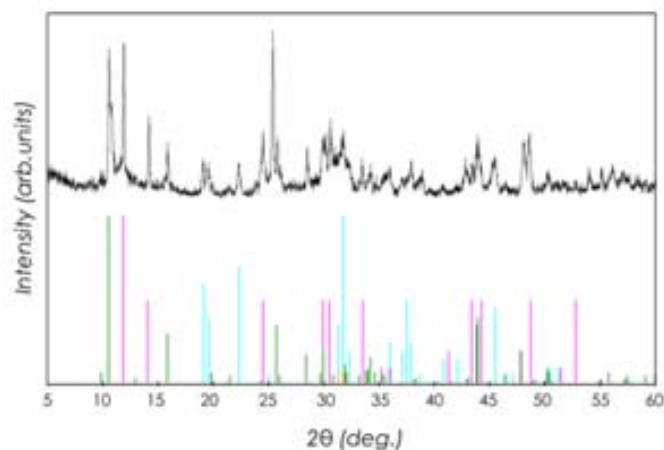


Figure 5.6. XRPD pattern corresponding to a mixture of  $\text{Na}_2\text{Ti}_3\text{O}_7$  with PDVF in 1:0.5 ratio after thermal treatment at 350 °C under air flow. Peaks corresponding to the identified compounds are denoted with colored vertical bars:  $\text{Na}_2\text{Ti}_3\text{O}_7$  (green, PDF # 31-1329),  $\text{Na}_2\text{Ti}_6\text{O}_{13}$  (pink, PDF# 37-951) and  $\text{Na}_3\text{TiOF}_5$  (blue, PDF# 24-1146).

### 5.2.2. Electrochemical performance of $\text{Na}_2\text{Ti}_3\text{O}_7$

Given the fact that enhancing the electrochemical capacity of  $\text{Na}_2\text{Ti}_3\text{O}_7$  through fluorination and concomitant introduction of sodium vacancies in the structure was not achieved, efforts were redirected to try to better understand the electrochemical mechanism of this compound. Reduction of  $\text{Na}_2\text{Ti}_3\text{O}_7$  involves formation of a phase with composition  $\text{Na}_4\text{Ti}_3\text{O}_7$  which could not be prepared by chemical means or isolated after electrochemical synthesis despite all the efforts made.[106,107,109] Moreover, all the studies reporting on the performance of  $\text{Na}_2\text{Ti}_3\text{O}_7$  upon cycling evidence significant capacity fading (~25% from first cycle) over 10 to 25 cycles. Such reports include samples prepared by diverse routes (solid state reaction or reverse microemulsion method) exhibiting particles with different morphologies and sizes, that are used to prepare electrodes with different technologies tested in various electrolytes. For example,  $\text{Na}_2\text{Ti}_3\text{O}_7$  micrometric rods [108] tested using 1 M  $\text{NaClO}_4$  in PC as electrolyte at C/10, showed a capacity fading of ~35 % after the 10<sup>th</sup> cycle and a discharge capacity of ca. 103mAh/g maintained after 20 cycles while  $\text{Na}_2\text{Ti}_3\text{O}_7$  prepared by solid state with further ball- milling exhibited a capacity of 125 mAh/g after 25 cycles (~30% fading).[110] A study on the performance of  $\text{Na}_2\text{Ti}_3\text{O}_7$  using

different electrolytes (PC and EC:PC with 1 M  $\text{NaClO}_4$  or NaTFSI salts), and electrode technologies was carried out by our group[109] which is also in line with the above mentioned reports. High capacity retention was only observed when increasing cycling rate: 95 % capacity retention was observed at C rate upon 10 cycles (~95 mAh/g) while it was only of 65% at C/25. Carbon coating on the  $\text{Na}_2\text{Ti}_3\text{O}_7$  particles has also been attempted as a strategy to enhance the electrochemical performance of the material which did not bring significant improvements either.[109,189] Such poor capacity retention does unfortunately prevent any consideration for the practical application of  $\text{Na}_2\text{Ti}_3\text{O}_7$  as electrode material.

Therefore, as part of this PhD, different experiments were carried out in order to shed more light into the matter by trying to ascertain whether structural degradation of  $\text{Na}_2\text{Ti}_3\text{O}_7$  and/or reactivity with the electrolyte do have an influence to that respect. Self-standing electrodes (SSE) prepared using the Bellcore technology[123] were fabricated, which were expected to exhibit a more homogeneous distribution of the active material while not containing any metal current collector (i.e. copper) which could interfere in *in situ* measurements.

The electrochemical profiles exhibited by such electrodes were compared to those of powdered electrodes (prepared by mixing 70% of  $\text{Na}_2\text{Ti}_3\text{O}_7$  and with 30% of SP carbon.) previously used by our group for *in situ* experiments in order to ensure that the electrode preparation method did not interfere with the results. EC:PC were selected as electrolytes due to the higher reported stability of the SEI layer on negative electrodes when EC is used as electrolyte co-solvent.[67] Tests were carried out using 1 M  $\text{NaPF}_6$  or 1 M  $\text{NaClO}_4$  as electrolyte salt. The electrochemical behavior of both electrodes is similar and the first reduction involves a pseudo- plateau around 0.6 V, previously attributed to parasitic reactions between the electrolyte and SP carbon followed by the plateau at ca. 0.3V related to the electrochemical activity of  $\text{Na}_2\text{Ti}_3\text{O}_7$  itself. The capacity delivered on that plateau upon the first reduction is in both cases similar (only slightly higher for SSE, 167mAh/g compared to 154mAh/g) and fades by ca. 25% after 10 cycles. Such results are also fully comparable with both electrolyte salts (see Figure 5.9) in line with what has been observed for other electrode materials.[64] The only difference between both types of electrodes is

the presence of a pseudo-plateau at 1.2 V, which does always appear for SSE and is not observed for powdered electrodes.

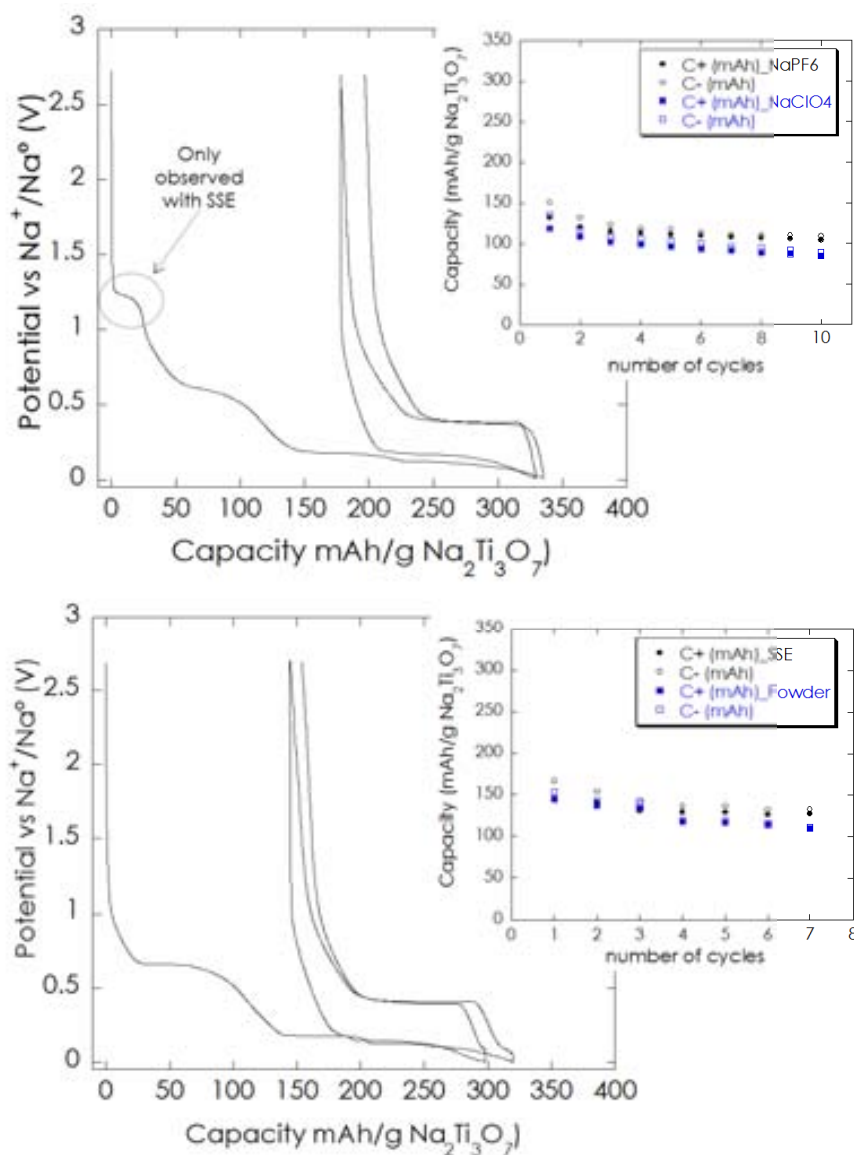


Figure 5.9. Potential vs capacity profile at C/15 for electrochemical tests carried out with Na<sub>2</sub>Ti<sub>3</sub>O<sub>7</sub> using powdered (below) and self-standing (above) electrodes. Plots of the capacity vs. cycle number in for the two electrolyte salts employed are also shown (inset).

An XRPD study was carried out in order to ascertain whether the electrode preparation procedure has an effect towards the electrode performance. Figure 5.8 shows the XRPD pattern of pristine Na<sub>2</sub>Ti<sub>3</sub>O<sub>7</sub> powder (pink pattern) and that of the prepared SSE (black pattern). Aside changes in the width of the peaks due to the modifications in particle size

and crystallinity that may be induced the ball- milling process, significant unexpected modification of the pattern is observed as intensities and positions of the peaks are also altered with respect to the pristine sample. The pattern bears some similarities with that of  $\text{H}_2\text{Ti}_3\text{O}_7$  which exhibits a structure related to that of  $\text{Na}_2\text{Ti}_3\text{O}_7$  but with a shift of  $[\text{Ti}_3\text{O}_7]^{2-}$  layers by  $b/2$  along the b-direction and a C-centered cell (C2/m space group) with cell parameters  $a = 16.02(1) \text{ \AA}$ ,  $b = 3.746(1) \text{ \AA}$ ,  $c = 9.1828 \text{ \AA}$  and  $\beta = 101.51 (1)^\circ$ . [109,190] Additionally, a very intense reflection is observed at  $43.91^\circ$  which is shifted about  $0.5^\circ$  from the position of the intense peak in this region for both  $\text{Na}_2\text{Ti}_3\text{O}_7$  and  $\text{H}_2\text{Ti}_3\text{O}_7$ . Such findings can be tentatively attributed to a partial exchange between  $\text{Na}^+$  and  $\text{H}^+$  during the preparation of the electrode, due to the presence of traces of water in the acetone used. This could either result in a mixture of  $\text{Na}_2\text{Ti}_3\text{O}_7$  and  $\text{H}_2\text{Ti}_3\text{O}_7$  or to  $\text{Na}_{2-x}\text{H}_x\text{Ti}_3\text{O}_7$ , which seems more plausible in view of the SRPD patterns.

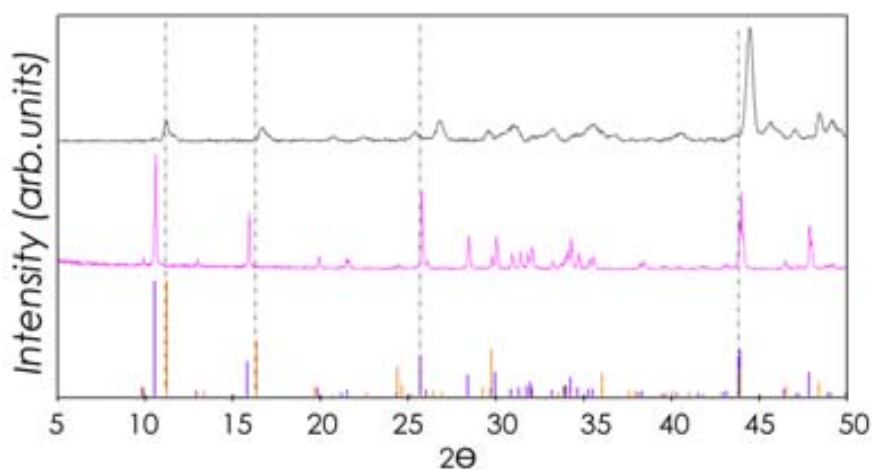


Figure 5.8. XRPD pattern of pristine  $\text{Na}_2\text{Ti}_3\text{O}_7$  (pink) and a self- standing electrode fabricated with  $\text{Na}_2\text{Ti}_3\text{O}_7$  (black). Peak positions and intensities for  $\text{Na}_2\text{Ti}_3\text{O}_7$  (purple, PDF#31-1329) and  $\text{H}_2\text{Ti}_3\text{O}_7$  (orange PDF#47-561)) are shown in the lower part of the graph.

Although the preparation of  $\text{H}_2\text{Ti}_3\text{O}_7$  is generally done by proton exchange in HCl, partial substitution of sodium ions with protons in a medium containing only minor amount of water impurities is not surprising considering that titanates have been largely used as adsorbents for water treatment [191–193]. Indeed, a very recent publication on the investigation of related lepidocrocite-type titanates as electrode materials does also report on water

uptake during electrode preparation, in that case using NMP (N-methylpyrrolidone) as solvent.[191] Moreover, the redox feature observed at 1.2V is in agreement with such hypothesis, as it has been previously observed when testing  $\text{H}_2\text{Ti}_3\text{O}_7$  in sodium cells.[109] However, even if the electrode preparation process does induce a partial exchange between sodium ions and protons, this does not seem to be related to the capacity fading observed. Indeed, on one hand, exchange of protons with sodium ions from the electrolyte has been observed in tests using  $\text{H}_2\text{Ti}_3\text{O}_7$  as electrode material in sodium cells as proved by *in situ* XRD measurements[109] and on the other, very similar capacity retention is observed for SSE and powdered electrodes. Thus, we believe that  $\text{Na}_{2-x}\text{H}_x\text{Ti}_3\text{O}_7$  gradually exchanges protons by sodium ions from the electrolyte and then exhibit the same electrochemical behavior as  $\text{Na}_2\text{Ti}_3\text{O}_7$ .

### **5.2.3. Studies on the redox mechanism of $\text{Na}_2\text{Ti}_3\text{O}_7$**

#### **5.2.3.1. *In situ* X-ray absorption measurements**

As mentioned above, all attempts to isolate pure  $\text{Na}_4\text{Ti}_3\text{O}_7$  either from fully reduced electrochemical cells or after chemical reduction of  $\text{Na}_2\text{Ti}_3\text{O}_7$  by different means, proved unsuccessful and yielded a mixture of  $\text{Na}_4\text{Ti}_3\text{O}_7$  and  $\text{Na}_2\text{Ti}_3\text{O}_7$ . [106] Thus, Density Functional Theory (DFT) calculations [106] were carried out that allowed to a structural models for this phase which was observed redox operation potential. Two models were found, which converged to the same crystal framework after full optimization. In the structure proposed for  $\text{Na}_4\text{Ti}_3\text{O}_7$ , the Ti-O framework is maintained as compared to  $\text{Na}_2\text{Ti}_3\text{O}_7$ , but the sodium distribution within the unit cell differs. In order to accommodate the two additional sodium ions, the pristine two sodium ions in  $\text{Na}_2\text{Ti}_3\text{O}_7$  move from their initial position ca. 0.7 Å for Na(2), and ca. 2.3 Å for Na(1), in consequence, the insertion of the two additional sodium ions induces a collective rearrangement of the sodium sublattice so that sodium ions in  $\text{Na}_4\text{Ti}_3\text{O}_7$  exhibit distorted octahedral coordination with Na-O distances ranging from 2.16 to 2.8 Å while they were occupying nine and seven coordination sites in pristine  $\text{Na}_2\text{Ti}_3\text{O}_7$ . Thus, a rearrangement of sodium ions within the layers takes place with migration from some of the initial positions (Na(3) and Na(6)) to more stable sites, allowing larger Na- Na distances



that seem to stabilize the structure. In  $\text{Na}_4\text{Ti}_3\text{O}_7$ , sodium ions lie in the middle of edge-sharing distorted octahedra with Na–O distances ranging from 2.16 to 2.8 Å. Such structure presents similarities to the rocksalt structure, which is commonly adopted by many binary systems, as there are an equal number of cations and anions in the formula unit (seven A/Ti and seven oxygen atoms). This model was found to be consistent when confronted with the *in situ* XRPD pattern data available. [106]

In light of the mechanism proposed, *in situ* XAS experiments were carried out to ascertain the oxidation state and local coordination environment for  $\text{Na}_4\text{Ti}_3\text{O}_7$  electrochemically prepared *in situ* from  $\text{Na}_2\text{Ti}_3\text{O}_7$  using the electrochemical cell described in Section 2.3.4.1. Measurements were carried out at Soleil synchrotron (SAMBA) and data was collected on the Ti- K edge, where rutile (*r*- $\text{TiO}_2$ ) and  $\text{Ti}_2\text{O}_3$  were used as  $\text{Ti}^{4+}$  and  $\text{Ti}^{3+}$  references, respectively. Figure 5.10 illustrates the normalized Ti- K XANES of the titanium references together with the spectrum of pristine  $\text{Na}_2\text{Ti}_3\text{O}_7$  and fully reduced  $\text{Na}_4\text{Ti}_3\text{O}_7$ . All spectra present pre- edge features that can be attributed to different electronic transitions, mainly from Ti 1s energy levels to Ti 3d (or O 2p), and 4p levels. As the coordination number of Ti increases, the normalized height of the pre- edge peak decreases and the peak position shifts to higher energies. Farges *et al* [194] established a correlation between the intensity of the pre-edge absorption and Ti coordination, with the intensity of a 6- coordinated Ti expected to lay below 0.4. Figure 5.10 (inset) shows an expanded view of the pre- edge peaks for all the measured samples. The spectrum of *r*-  $\text{TiO}_2$  presents three characteristic pre- edge peaks (red line), which are also observed in  $\text{Na}_2\text{Ti}_3\text{O}_7$ , with an increase in the intensity of the second pre- edge peak, which has been attributed to the hybridization of the central Ti 4p orbital with 3d orbitals of second shell Ti neighbors.

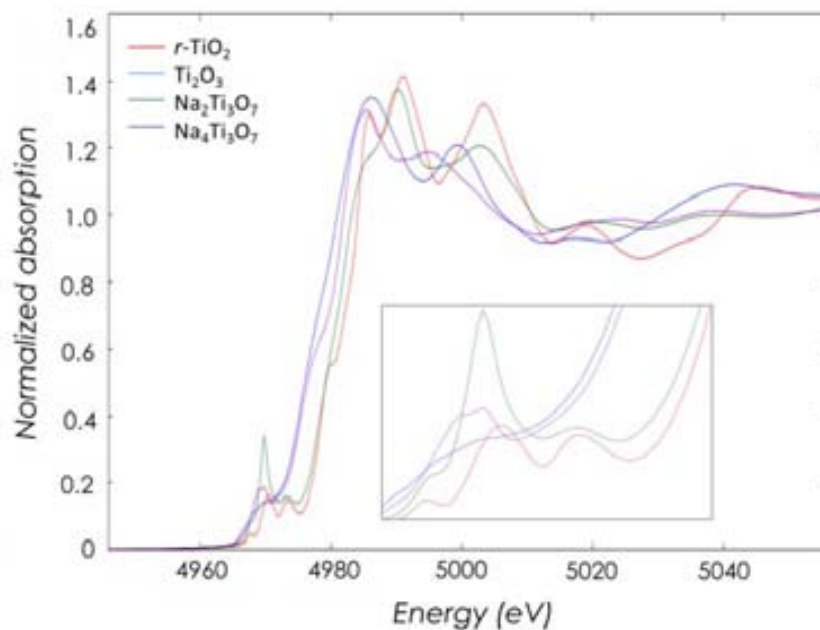


Figure 5.10. Ti- K edge absorption spectra taken using the *in situ* electrochemical cell for pristine  $\text{Na}_2\text{Ti}_3\text{O}_7$  and fully reduced  $\text{Na}_4\text{Ti}_3\text{O}_7$ . Spectra from reference  $r\text{-TiO}_2$  and  $\text{Ti}_2\text{O}_3$  are also shown.

The intensity of the the pre- edge features can be correlated to the degree of symmetry present in the coordination sphere of the absorbing atom. In  $\text{Na}_2\text{Ti}_3\text{O}_7$ , Ti occupies 3 different crystallographic octahedral positions with Ti-O distances that range from 1.75 Å to 2.27 Å, which describe a more distorted octahedra when compared to  $r\text{-TiO}_2$ , which exhibits Ti- O distances ranging between 1.958 and 1.966 Å. Interestingly, the intensity of the pre- edge features for  $\text{Na}_4\text{Ti}_3\text{O}_7$  is lower than for  $\text{Na}_2\text{Ti}_3\text{O}_7$ , which points to a slightly more regular Ti coordination environment, which is consistent with DFT calculations. The pre- edge position of  $\text{Na}_4\text{Ti}_3\text{O}_7$  is located at lower energies when compared with  $r\text{-TiO}_2$  and  $\text{Na}_2\text{Ti}_3\text{O}_7$ , in agreement with the decrease in the titanium oxidation state upon sodium insertion. A shift of the Ti absorption white line to lower energies for  $\text{Na}_4\text{Ti}_3\text{O}_7$  when compared to  $\text{Na}_2\text{Ti}_3\text{O}_7$  is also observed, again in agreement with the reduction of Ti atoms concomitant to intercalation of sodium ions in the structure. The oxidation states of titanium in the samples were determined considering the mid- height of the absorption edge. Main- edge energy positions for all samples measured and estimated oxidation states for the sodium titanates are given in Table 5.3.

Table 5.3. Pre- edge and main – absorption edge energy positions and oxidation states for reference samples, Na<sub>2</sub>Ti<sub>3</sub>O<sub>7</sub> and Na<sub>4</sub>Ti<sub>3</sub>O<sub>7</sub>.

Sample	Pre- edge position (eV)	Normalized Height	Main- edge position (eV)	Oxidation State
r-TiO <sub>2</sub>	4970.44	0.16	4979.36	4
Ti <sub>2</sub> O <sub>3</sub>	4969.69	0.14	4976.01	3
Na <sub>2</sub> Ti <sub>3</sub> O <sub>7</sub>	4969.81	0.34	4979.16	3.9 (est)
Na <sub>4</sub> Ti <sub>3</sub> O <sub>7</sub>	4969.39	0.19	4976.44	3.1 (est)

Linear fitting estimations disclose that the oxidation state of Ti in Na<sub>2</sub>Ti<sub>3</sub>O<sub>7</sub> is close to Ti<sup>4+</sup> and, once fully reduction to Na<sub>4</sub>Ti<sub>3</sub>O<sub>7</sub> is achieved, the Ti atoms are reduced to approximately Ti<sup>3.1+</sup>, which is somewhat lower than what would be expected from the expected Na<sub>4</sub>Ti<sub>3</sub>O<sub>7</sub> formula (Ti<sup>3.3+</sup>).

### 5.2.3.2. In operando XRPD measurements

The evolution of the diffraction pattern Na<sub>2</sub>Ti<sub>3</sub>O<sub>7</sub> upon full electrochemical reduction was also followed by *in operando* SXRPD at ALBA synchrotron ( $\lambda=0.61988$  Å) using the *in situ* electrochemical cell described in Section 2.3.4.2. SSE electrodes containing ca. 9 mg of active materials were used as working electrodes and cells were assembled with sodium metal counter electrodes and 1 M NaClO<sub>4</sub> in EC: PC as electrolyte and tested at C/8, which was chosen to prevent excessive duration of the experiment. SXRPD data were collected every 10 min (3 minute acquisition time) all along the reduction process. The complete evolution of the SXRPD patterns collected during the full reduction as function of time is presented in Figure 5.11 together with a 2D projection which illustrates the changes in intensity and position shifting of the main diffraction peaks.

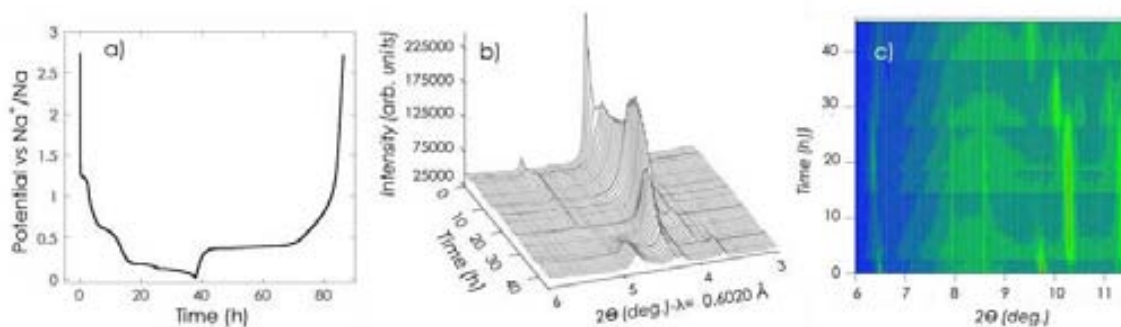


Figure 5.11. a) Potential vs time profile for Na<sub>2</sub>Ti<sub>3</sub>O<sub>7</sub> SSE cycled vs Na<sup>0</sup> at C/8. b) 3-D plot showing the evolution of the SXRDP patterns collected during electrochemical reduction as a function of time. c) 2-D projection of SXRDP data depicting the changes in intensity and position of the main diffraction peaks as reduction proceeds and sodium intercalation takes place.

The initial SXRDP pattern corresponds to the protonated Na<sub>2-x</sub>H<sub>x</sub>Ti<sub>3</sub>O<sub>7</sub> phase and can be fitted with the H<sub>2</sub>Ti<sub>3</sub>O<sub>7</sub> structure, with cell parameters ( $a= 16.336(9) \text{ \AA}$ ,  $b= 3.7242(7) \text{ \AA}$ ,  $c= 9.202(2) \text{ \AA}$  and  $\beta=102.10(2)^\circ$ ) very close to those reported for the pure phase, which make us conclude that the amount of sodium ions present in the electrode is almost negligible ( $x \sim 1$ ) (see Figure 5.12b). As the reduction starts, changes in the intensity and position of the main two diffraction peaks are observed up to 1.25 V ( $t=3h$ ) which can be attributed to the intercalation of sodium ions in the protonated phase. In addition, concomitant exchange of protons present in the sample with sodium ions from the electrolyte can also be expected, as previously reported for H<sub>2</sub>Ti<sub>3</sub>O<sub>7</sub> and also Li<sub>2</sub>Ti<sub>3</sub>O<sub>7</sub> when reduced in electrochemical cells using sodium containing electrolytes.[106] Further reduction proceeds with a pseudo plateau centered at ca. 0.6 V which does not seem to induce any change in the SXRDP patterns, in agreement with this phenomenon being attributed to the parasitic reaction of the electrolyte with SP carbon, as previously suggested. When reduction is pursued to potentials lower than 0.18 V ( $t= 25h$ ), the evolution of a new set of diffraction peaks is observed that correspond to the reduced phase Na<sub>4</sub>Ti<sub>3</sub>O<sub>7</sub> which gradually grow to the expense of those corresponding to the pristine Na<sub>2</sub>Ti<sub>3</sub>O<sub>7</sub> phase.

At the end of reduction, the SXRD patterns exhibit  $\text{Na}_4\text{Ti}_3\text{O}_7$  as a major phase, with refined cell parameters  $a=7.4260(13)$ ,  $b=4.3345(8)$ ,  $c=9.688(3)$  and  $\beta=97.86(3)^\circ$ , in good agreement with those predicted from DFT calculations. Unfortunately, some  $\text{H}_2\text{Ti}_3\text{O}_7$  and  $\text{Na}_2\text{Ti}_3\text{O}_7$  were still present in the electrode, which precluded the obtaining of further structural information from the data available.

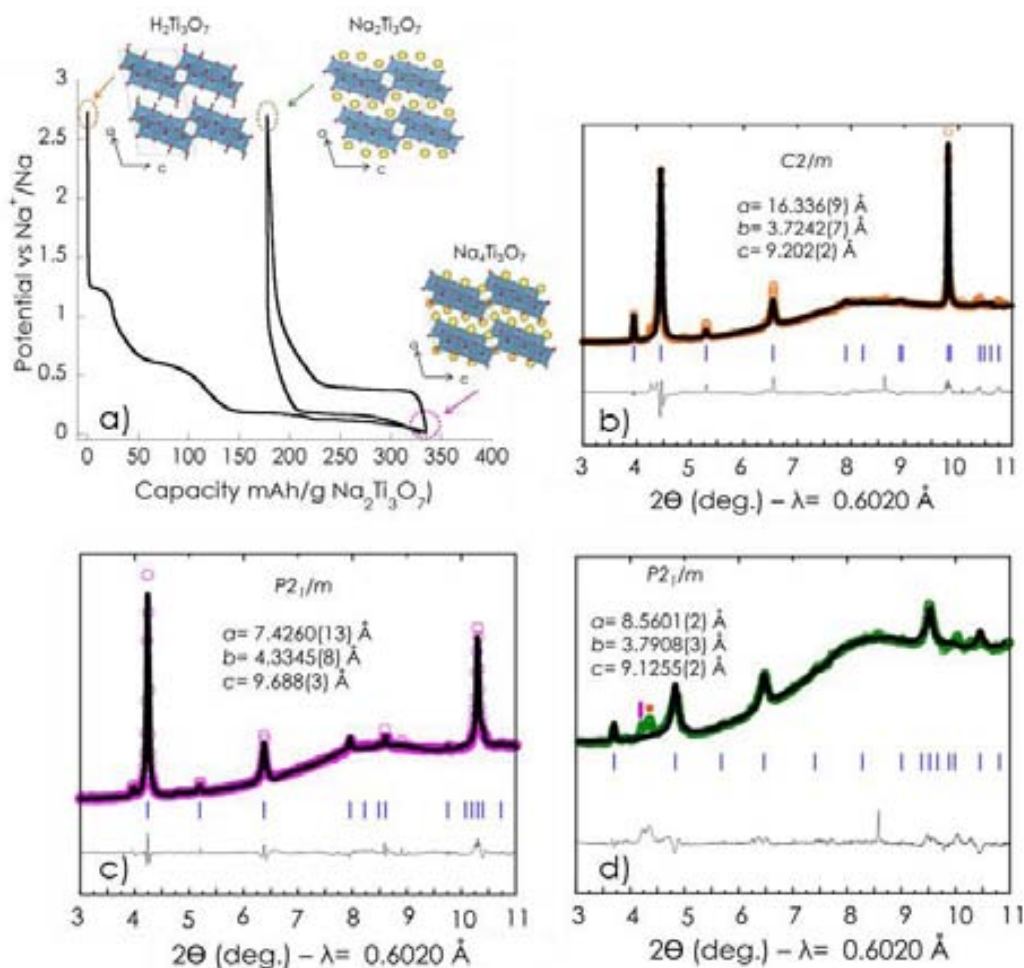


Figure 5.12. a) Potential vs time profile for  $\text{Na}_2\text{Ti}_3\text{O}_7$  SSE tested at C/8 vs  $\text{Na}^+$  using an *in situ* cell. Rietveld refinement of the SXRD patterns taken at b) the beginning of reduction ( $\text{H}_2\text{Ti}_3\text{O}_7$ ), c) the end of reduction ( $\text{Na}_4\text{Ti}_3\text{O}_7$ ), d) the end of reoxidation ( $\text{Na}_2\text{Ti}_3\text{O}_7$ ).

Further on, the working electrode was reoxidized and an SXRPD pattern was taken at the end of oxidation, which is typical of  $\text{Na}_2\text{Ti}_3\text{O}_7$ , with cell parameters in full agreement with expected values:  $a=8.5601(2)$  Å,  $b=3.7908(3)$  Å,  $c=9.1255(1)$  Å and  $\beta=101.70(2)^\circ$ . Such results confirm that even if the initial phase in the electrode was  $\text{H}_2\text{Ti}_3\text{O}_7$ , proton exchange

with sodium ions present in the electrolyte takes place so that the active phase present in the electrode during subsequent cycling is  $\text{Na}_2\text{Ti}_3\text{O}_7$ . This is in agreement with the very similar electrochemical behavior reported above for powdered and SSE electrodes prepared with  $\text{Na}_2\text{Ti}_3\text{O}_7$ , the latter found to contain  $\text{H}_2\text{Ti}_3\text{O}_7$  instead.

In order to evaluate whether the capacity fading may be related to degradation of  $\text{Na}_2\text{Ti}_3\text{O}_7$  upon cycling, SXRPD was taken on a SSE electrode after 50 cycles at C/15 (see Figure 5.13a). The pattern is very similar to that of the electrode after one cycle (Figure 5.13b) with peaks becoming somewhat more lorentzian, which is in agreement with an enhancement in strains as typically observed for battery materials upon cycling. The refined cell parameters ( $a=8.5001(3)$ ,  $b=3.8018(4)$ ,  $c=9.1293(19)$  and  $\beta=101.378(10)^\circ$ ) do not significantly differ from that of the electrode after one cycle which prompts us to conclude that capacity fading in  $\text{Na}_2\text{Ti}_3\text{O}_7$  is not related to structural degradation of the phase upon cycling.

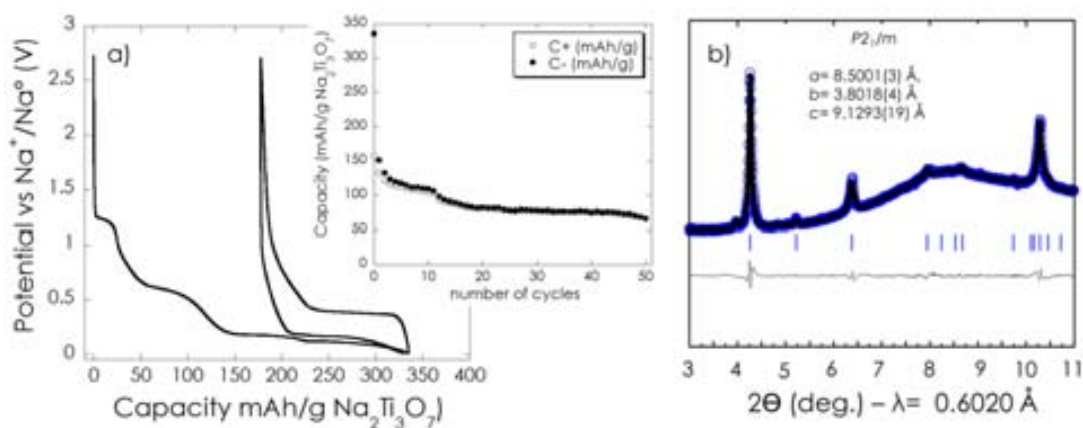


Figure 5.13. (Right) SXRD pattern collected at ALBA synchrotron ( $\lambda=0.602 \text{ \AA}$ ) for SSE after after 50 cycles and corresponding cell parameters. The first cycle and the capacity vs. cycle number are also shown (left and center respectively).

At this point, two hypotheses were considered to explain the poor capacity retention of  $\text{Na}_2\text{Ti}_3\text{O}_7$ : first, a possible intrinsic low stability of the  $\text{Na}_4\text{Ti}_3\text{O}_7$  phase formed upon reduction (which would explain why its isolation is so elusive), and second, enhanced reactivity of the active material with the electrolyte.

The stability of  $\text{Na}_4\text{Ti}_3\text{O}_7$  was thus studied by DFT. The total energy of the phase was calculated using ab initio methods implemented in the Vienna *ab initio* simulation package (VASP)- The projector augmented wave (PAW) potential set was used with the exchange and correlation energies approximated in the generalized gradient approximation with the Hubbard parameter correction (GGA + U), following the rotationally invariant form. An effective U value of 4 eV ( $J = 1$  eV) was used for the d states of Ti ions. The entropy ( $\Delta S$ ) of  $\text{Na}_2\text{Ti}_3\text{O}_7$  and the reduced phase  $\text{Na}_4\text{Ti}_3\text{O}_7$  were calculated, and the intercalation of two sodium ions was found to increase the entropy difference with temperatures expected. Meanwhile, free energy of the sodiated phase was found to remain approximately constant even at 500 K, as can be observed in Figure 5.14. With such small free energy differences and considering only thermodynamic arguments, there is no reason to infer that the stability of  $\text{Na}_2\text{Ti}_3\text{O}_7$  and  $\text{Na}_4\text{Ti}_3\text{O}_7$  is significantly different and thus, reactivity with the electrolyte emerged as the most plausible hypothesis to account for the observed capacity fading.

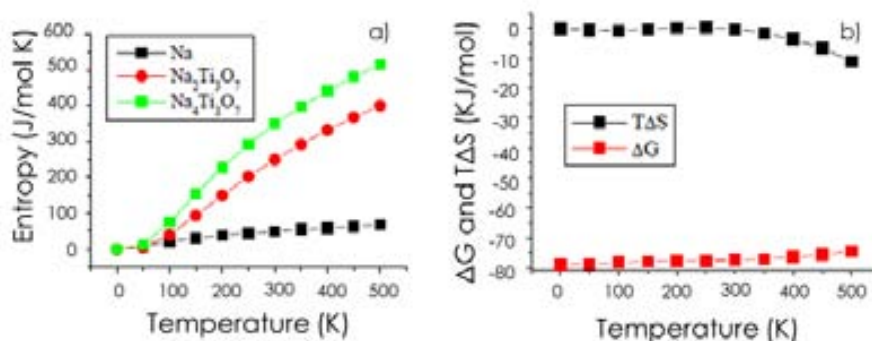


Figure 5.15. a) Calculated entropy variation of Na metal (black squares),  $\text{Na}_2\text{Ti}_3\text{O}_7$  (red dots) and  $\text{Na}_4\text{Ti}_3\text{O}_7$  (green squares) as function of temperature. b) Calculated variation of free energy as function of temperature.

### 5.2.3.3. Stability of $\text{Na}_2\text{Ti}_3\text{O}_7$ in different electrolytes.

Given the above mentioned results and the surprising recently reports on the reactivity of  $\text{Li}_4\text{Ti}_5\text{O}_{12}$  with LIB electrolyte solvents even in absence of any applied current,[195] we decided to check for the possibility of similar reactivity in the case of  $\text{Na}_2\text{Ti}_3\text{O}_7$ . About 100 mg

of sample were kept for 8 months at room temperature inside the glove box in closed vials with ca. 2 ml of common electrolytes and electrolyte solvents used for SIB a) ethylene carbonate (EC), b) 50% ethylene carbonate: 50% propylene carbonate (EC: PC) c) 1 M NaClO<sub>4</sub> in EC: PC and c) 1 M NaPF<sub>6</sub> in EC: PC. The experiments were duplicated, with the second batch being kept at 60 °C for the last two weeks. Once the storage tests were finished, the powders were recovered and washed once with dimethyl carbonate (DMC) that was left to evaporate at room temperature with subsequent drying at 60 °C for 2 hours.

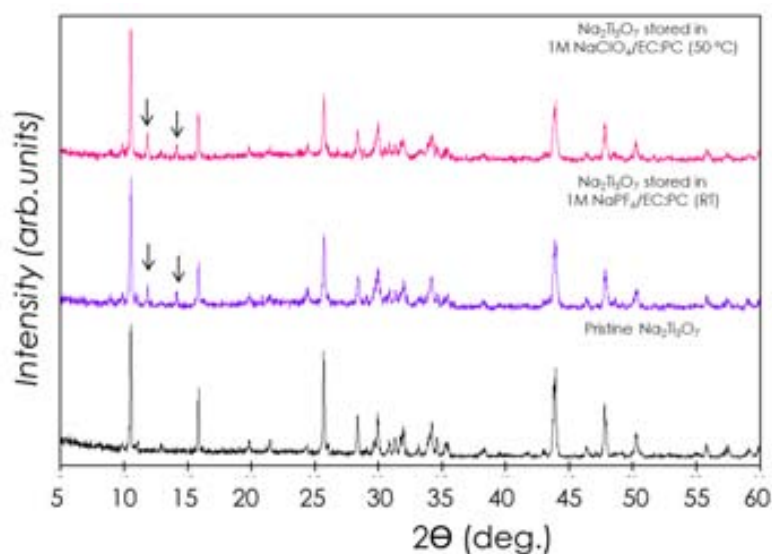


Figure 5.7. Evolution of XRPD patterns of Na<sub>2</sub>Ti<sub>3</sub>O<sub>7</sub> after 8 months stored in different electrolytes/electrolyte solvents.

The XRPD patterns of all the samples left to interact with the electrolytes at room temperature and 50 °C depict a small decrease of the relative intensity of the diffraction peak at 2 $\theta$ : 25.7° and the appearance of small intensity additional peaks which were found to correspond to Na<sub>2</sub>Ti<sub>6</sub>O<sub>13</sub> (2 $\theta$ : 11.85°, 14.06° and 24.49°). The nature of the salt or solvent used in the electrolyte does not seem to have a significant effect in such evolution, given that almost identical patterns are achieved for the samples stored in EC:PC and PC for both types of experiments. Selected XRPD patterns are shown in Figure 5.7, where the arrows denote peaks corresponding to Na<sub>2</sub>Ti<sub>6</sub>O<sub>13</sub>. Such transformation from Na<sub>2</sub>Ti<sub>3</sub>O<sub>7</sub> to Na<sub>2</sub>Ti<sub>6</sub>O<sub>13</sub> involves a condensation reaction and is unexpected at such low temperatures, as it has



been previously been achieved only through thermal treatment of  $\text{Na}_2\text{Ti}_3\text{O}_7$  at temperatures ranging from 300 to 800 °C.[196,197] The mechanism of such reaction at room temperature is currently unclear, but such unexpected results prove that there is interaction of  $\text{Na}_2\text{Ti}_3\text{O}_7$  with the electrolyte and make us suspect that some reactivity may also exist between the electrolyte and the reduced  $\text{Na}_4\text{Ti}_3\text{O}_7$  which may be even more reactive, since it contains titanium in mixed oxidation state. Thus, such preliminary results point at degradation of the active material due to reactivity with the electrolyte as one of the plausible causes contributing to capacity fading. This would be in agreement with the capacity retention being higher at higher testing rate, with the lack of cell potential stabilization upon cell relaxation observed in previous studies and also consistent with a very recent work published during the writing of this dissertation [189] reporting on a full solid- state SIB containing  $\text{P}_2\text{-Na}_{2/3}[\text{Fe}_{1/2}\text{Mn}_{1/2}]\text{O}_2$  as positive electrode, a composite mixture of  $\text{Na}_2\text{Ti}_3\text{O}_7/\text{La}_{0.8}\text{Sr}_{0.2}\text{MnO}_3$  as the negative electrode and  $\text{Na-}\beta''\text{-Al}_2\text{O}_3$  solid electrolyte, which is tested at 350 °C and exhibits a specific capacity of 152 mAh/g (referred to the positive electrode) which is retained (>90%) both at C/20 and 1C after 100 cycles. Such findings would thus confirm the intrinsic stability of the reduced phase even at high temperatures and also point at the parasitic reactions with liquid electrolytes being at the origin of the capacity fading observed. Nonetheless, further efforts in this direction should be pursued in order to fully confirm the above mentioned assumptions and fully assess the practical prospects of  $\text{Na}_2\text{Ti}_3\text{O}_7$  as negative electrode material for SIB.

## **General conclusions**

Along the course of this dissertation, the synthesis and structural characterization of Na-M- (O,F) with M= Ti, V, Mn and Mo have been described, together with their electrochemical behavior and possibility of application as electrode materials for Na- ion batteries. The most significant conclusions resulting from this work are described below:

1. Na<sub>2</sub>MnF<sub>5</sub> and NaMnF<sub>3</sub> have been prepared from aqueous solutions containing hydrofluoric acid and different sodium and manganese precursors at room temperature. The electrochemical tests of these materials do not indicate significant electrochemical activity. DFT calculations allow to predict that deinsertion of one mol of Na ions from the Na<sub>2</sub>MnF<sub>5</sub> and NaMnF<sub>3</sub> respectively involving the Mn<sup>+3</sup>/Mn<sup>+4</sup> and Mn<sup>+2</sup>/Mn<sup>+3</sup> redox couples take place at 4.9 V and 3.8 V. While the former falls above the stability region of the electrolytes used, this is not the case for the later. The highly insulating character of fluorides inducing large cell polarization is thus most probably at the origin of the electrochemical behavior observed.
2. Attempts to prepare a mixed sodium manganese oxyfluoride failed but the resulted in the synthesis of the novel molybdenum containing compound NaMnMoO<sub>3</sub>F<sub>3</sub>·H<sub>2</sub>O, which was characterized by neutron and SXRPD. It presents a layered orthorhombic structure with cell parameters  $a = 3.5947(1) \text{ \AA}$ ,  $b = 21.246(1) \text{ \AA}$  and  $c = 7.3893(2) \text{ \AA}$  and space group *Cmcm* (n° 63) where sodium ions and water molecules are located in the interlayer space. .

3. The study of the Na-V-(O,F) system resulted in the solvothermal precipitation of a variety of compounds depending on the water/ethylene glycol ratio, HF concentration and temperature. A new oxyfluoride with cryolite structure ( $\text{Na}_{3-5}\text{VOF}_5$ ) was characterized by SXRPD, which exhibits monoclinic symmetry with  $a=5.54034(2)$  Å,  $b=5.68041(2)$  Å,  $c=7.95229(3)$  Å cell parameters,  $\beta=90.032(7)^\circ$  and space group  $P21/n$  (n° 14).
4. The chiolite  $\text{Na}_{5-5}\text{V}_3\text{F}_{14}$  was prepared from a reaction medium with high HF concentration at 100 °C and characterized by means of neutron and SXRPD. It exhibits orthorhombic symmetry with cell parameters  $a=10.5482(2)$  Å,  $b=10.4887(1)$  Å and  $c=10.3243(1)$  Å and  $Cmc2_1$  space group, and constitutes the first sodium vanadium chiolite prepared under mild synthetic conditions. A single crystal recovered from a reaction carried out at 200 °C, did also exhibit chiolite structure but with tetragonal symmetry ( $a=7.380(3)$  Å,  $b=7.380(3)$  Å and  $c=10.381(11)$  Å and space group  $P4_22_12$  (n° 94)). Bond valence sum indicates that it contains  $\text{V}^{4+}$  and therefore can be formulated as  $\text{Na}_5\text{V}_3\text{O}_3\text{F}_{11}$ . None of the vanadium containing phases prepared did exhibit significant electrochemical activity in sodium cells.
5. The  $\text{Na}_5\text{Ti}_3\text{O}_3\text{F}_{11}$  chiolite was prepared by a microwave-assisted method. It crystallizes with orthorhombic symmetry (space group  $Cmca$  (n° 64)) and cell parameters  $a=10.496(2)$  Å,  $b=10.398(1)$  Å and  $c=10.291(1)$  Å.
6. Attempts to prepare  $\text{Na}_{2-x}\text{Ti}_3\text{O}_{7-x}\text{F}_x$  by either direct synthesis or fluorination of  $\text{Na}_2\text{Ti}_3\text{O}_7$  failed and thus efforts were re-directed to shed some light on the causes of capacity fading in  $\text{Na}_2\text{Ti}_3\text{O}_7$ . The preparation of self-standing electrodes (SSE) with this compound was found to induce partial exchange of sodium ions with protons, which did induce a redox feature at 1.2V vs.  $\text{Na}^+/\text{Na}$  but does not seem to have any effect on capacity retention.

7. The reduction of SSE was followed by XAS and *in situ* diffraction which confirm the formation of  $\text{Na}_4\text{Ti}_3\text{O}_7$  ( $a=7.309(3)$ ,  $b=4.381(2)$ ,  $c=9.664(5)$  and  $\beta=97.32(2)^\circ$ ) upon reduction. SXRD patterns on SSE after 50 cycles indicate that no degradation of  $\text{Na}_2\text{Ti}_3\text{O}_7$  takes place and indicate that capacity fading is not related to structural degradation of the phase upon cycling.
  
8. Long term exposure of  $\text{Na}_2\text{Ti}_3\text{O}_7$  powder to electrolytes (either containing  $\text{NaClO}_4$  or  $\text{NaPF}_6$ ) or electrolyte solvents was found to induce the formation  $\text{Na}_2\text{Ti}_6\text{O}_{13}$ . Such reactivity is not yet fully understood but it is most likely contributing to capacity fading for  $\text{Na}_2\text{Ti}_3\text{O}_7$ .

## **REFERENCES**

- [1] R.D. Shannon, *Acta Crystallogr. Sect. A* 32 (1976) 751.
- [2] B.L. CHAMBERLAND, in: *Inorg. Solid Fluorides*, 1985, pp. 205–258.
- [3] A. Simon, J. Ravez, *Ferroelectrics* 24 (1980) 305.
- [4] A.M. Fry, H.A. Seibel, I.N. Lokuhewa, P.M. Woodward, *J. Am. Chem. Soc.* 134 (2012) 2621.
- [5] F.J. Brink, L. Norén, D.J. Goossens, R.L. Withers, Y. Liu, C.-N. Xu, *J. Solid State Chem.* 174 (2003) 450.
- [6] A. Fuertes, *Inorg. Chem.* 45 (2006) 9640.
- [7] D. BABEL, A. TRESSAUD, in: *Inorg. Solid Fluorides*, 1985, pp. 77–203.
- [8] W. Massa, D. Babel, *Chem. Rev.* 88 (1988) 275.
- [9] I.N. Flerov, M.V. Gorev, K.S. Aleksandrov, A. Tressaud, J. Grannec, M. Couzi, *Mater. Sci. Eng. R Reports* 24 (1998) 81.
- [10] J. Ravez, G. Peraudeau, H. Arend, S.C. Abrahams, P. Hagenmuller, *Ferroelectrics* 26 (1980) 767.
- [11] V.D. Fokina, I.N. Flerov, M. V. Gorev, M.S. Molokeev, A.D. Vasiliev, N.M. Laptash, *Ferroelectrics* 347 (2007) 60.
- [12] M.S. Molokeev, S. V. Misyul', V.D. Fokina, A.G. Kocharova, K.S. Aleksandrov, *Phys. Solid State* 53 (2011) 834.
- [13] F.J. Brink, L. Norén, R.L. Withers, *J. Solid State Chem.* 174 (2003) 44.
- [14] M.S. Molokeev, A.D. Vasiliev, A.G. Kocharova, *Powder Diffr.* 22 (2012) 227.
- [15] M.R. Marvel, J. Lesage, J. Baek, P.S. Halasyamani, C.L. Stern, K.R. Poeppelmeier, *J. Am. Chem. Soc.* 129 (2007) 13963.
- [16] J.P. Chaminade, M. Cervera-Marzal, J. Ravez, *Mater. Sci. Eng. B* 3 (1989) 497.
- [17] V. V. Atuchin, M.S. Molokeev, G.Y. Yurkin, T.A. Gavrilova, V.G. Kesler, N.M. Laptash, I.N. Flerov, G.S. Patrin, *J. Phys. Chem. C* 116 (2012) 10162.
- [18] M. Vlasse, G. Matejka, A. Tressaud, B.M. Wanklyn, *Acta Crystallogr. Sect. B Struct. Crystallogr. Cryst. Chem.* 33 (1977) 3377.
- [19] P. Núñez, T. Roisnel, A. Tressaud, *Solid State Commun.* 92 (1994) 601.
- [20] C. Brosset, *Zeitschrift Für Anorg. Und Allg. Chemie* 238 (1938) 201.
- [21] C. Jacoboni, A. Leble, J.J. Rousseau, *J. Solid State Chem.* 36 (1981) 297.
- [22] J. Yacoubi, A. Ravez, J. Grannec, *Chem. Scr.* 27 (1987) 429.
- [23] B.M. Wanklyn, B.J. Garrard, F. Wondre, W. Davison, *J. Cryst. Growth* 33 (1976) 165.
- [24] a. Le Bail, a.-M. Mercier, *Powder Diffr.* 18 (2012) 128.

- [25] H. McKinzie, J.M. Dance, A. Tressaud, J. Portier, P. Hagenmuller, *Mater. Res. Bull.* 7 (1972) 673.
- [26] C. Cros, J.-M. Dance, J.-C. Grenier, B.M. Wanklyn, B.J. Garrard, *Mater. Res. Bull.* 12 (1977) 415.
- [27] J. Ravez, M. Elaatmani, M. Cervera-Marzal, J.-P. Chaminade, M. Pouchard, *Mater. Res. Bull.* 16 (1981) 1167.
- [28] E.H.P. Cordfunke, M.E. Huntelaar, D.J.W. IJdo, *J. Solid State Chem.* 146 (1999) 144.
- [29] A.M. Glazer, *Acta Crystallogr. Sect. B Struct. Sci.* 58 (2002) 1075.
- [30] M. Al-Mamouri, P.P. Edwards, C. Greaves, M. Slaski, *Nature* 369 (1994) 382.
- [31] W. Rüdorff, D. Krug, *Zeitschrift Für Anorg. Und Allg. Chemie* 329 (1964) 211.
- [32] B.L. Chamberland, *Mater. Res. Bull.* 6 (1971) 311.
- [33] I.D. Gocheva, I. Tanaka, T. Doi, S. Okada, J. Yamaki, *Electrochem. Commun.* 11 (2009) 1583.
- [34] S.L. Cresswell, S.J. Haswell, *J. Chem. Educ.* 78 (2001) 900.
- [35] K.J. Rao, B. Vaidhyanathan, M. Ganguli, P. a. Ramakrishnan, *Chem. Mater.* 11 (1999) 882.
- [36] D. Series, *C.R. Data*, (n.d.) 112.
- [37] A. Tressaud, ed., *Functionalized Inorganic Fluorides*, John Wiley & Sons, Ltd, Chichester, UK, 2010.
- [38] J. Zhao, W. Yan, *Modern Inorganic Synthetic Chemistry*, Elsevier, 2011.
- [39] M. Estruga, M. Casas-Cabanas, D. Gutiérrez-Tauste, C. Domingo, J. a. Ayllón, *Mater. Chem. Phys.* 124 (2010) 904.
- [40] M. Pietrowski, M. Wojciechowska, *J. Fluor. Chem.* 128 (2007) 219.
- [41] P. Parhi, J. Kramer, V. Manivannan, *J. Mater. Sci.* 43 (2008) 5540.
- [42] L. Di Carlo, D.E. Conte, E. Kemnitz, N. Pinna, *Chem. Commun. (Camb)*. 50 (2014) 460.
- [43] G. Scholz, O. Korup, *Solid State Sci.* 8 (2006) 678.
- [44] I.D. Gocheva, M. Nishijima, T. Doi, S. Okada, J. Yamaki, T. Nishida, *J. Power Sources* 187 (2009) 247.
- [45] N. Dimov, A. Nishimura, K. Chihara, A. Kitajou, I.D. Gocheva, S. Okada, *Electrochim. Acta* 110 (2013) 214.
- [46] J. Lee, H. Shin, J. Lee, H. Chung, Q. Zhang, F. Saito, 44 (2003) 1457.
- [47] J. Lee, Q. Zhang, F. Saito, *Chem. Lett.* (2001) 700.
- [48] J. Lee, Q. Zhang, F. Saito, *J. Am. Ceram. Soc.* 84 (2001) 863.
- [49] A. Basa, E. Gonzalo, A. Kuhn, F. García-Alvarado, *J. Power Sources* 207 (2012) 160.



- [50] E. Gonzalo, A. Kuhn, F. García-Alvarado, *J. Power Sources* 195 (2010) 4990.
- [51] M. Estruga, M. Casas-Cabanas, D. Gutiérrez-Tauste, C. Domingo, J.A. Ayllón, *Mater. Chem. Phys.* 124 (2010) 904.
- [52] I. Moriguchi, K. Sonoda, K. Matsuo, S. Kagawa, Y. Teraoka, *Chem. Commun.* (2001) 1344.
- [53] W.A. Publishing, N. York, *HANDBOOK OF HYDROTHERMAL TECHNOLOGY A Technology for Crystal Growth and Materials Processing*, n.d.
- [54] S. Feng, R. Xu, *Acc. Chem. Res.* 34 (2001) 239.
- [55] D.W. Aldous, P. Lightfoot, *J. Fluor. Chem.* 144 (2012) 108.
- [56] D.W. Aldous, R.J. Goff, J.P. Atfield, P. Lightfoot, *Inorg. Chem.* 46 (2007) 1277.
- [57] A.C.A. Jayasundera, R.J. Goff, Y. Li, A.A. Finch, P. Lightfoot, *J. Solid State Chem.* 183 (2010) 356.
- [58] J. Sheng, K. Tang, W. Cheng, J. Wang, Y. Nie, Q. Yang, *J. Hazard. Mater.* 171 (2009) 279.
- [59] C. Zhao, S. Feng, Z. Chao, C. Shi, R. Xu, J. Ni, *Chem. Commun.* (1996) 1641.
- [60] J.M. Tarascon, M. Armand, *Nature* 414 (2001) 359.
- [61] J.B. Goodenough, K.-S. Park, *J. Am. Chem. Soc.* 135 (2013) 1167.
- [62] D. Linden, T.B. Reddy, *HANDBOOK OF BATTERIES*, n.d.
- [63] M.R. Palacín, *Chem. Soc. Rev.* 38 (2009) 2565.
- [64] A. Ponrouch, E. Marchante, M. Courty, J.-M. Tarascon, M.R. Palacín, *Energy Environ. Sci.* 5 (2012) 8572.
- [65] X. Xia, J.R. Dahn, *J. Electrochem. Soc.* 159 (2012) A515.
- [66] K. Kubota, N. Yabuuchi, H. Yoshida, M. Dahbi, S. Komaba, *MRS Bull.* 39 (2014) 416.
- [67] A. Ponrouch, E. Marchante, M. Courty, J.-M. Tarascon, M.R. Palacín, *Energy Environ. Sci.* 5 (2012) 8572.
- [68] J.B. Goodenough, Y. Kim, *Chem. Mater.* 22 (2010) 587.
- [69] J.B. Goodenough, *J. Solid State Electrochem.* 16 (2012) 2019.
- [70] U.S. Geological Survey: *Mineral Commodity Summaries*, 2013.
- [71] V. Palomares, P. Serras, I. Villaluenga, K.B. Hueso, J. Carretero-González, T. Rojo, *Energy Environ. Sci.* 5 (2012) 5884.
- [72] S.P. Ong, V.L. Chevrier, G. Hautier, A. Jain, C. Moore, S. Kim, X. Ma, G. Ceder, *Energy Environ. Sci.* 4 (2011) 3680.
- [73] T. Oshima, M. Kajita, A. Okuno, *Int. J. Appl. Ceram. Technol.* 1 (2005) 269.
- [74] R.J. Bones, *J. Electrochem. Soc.* 136 (1989) 1274.

- [75] C. DELMAS, J. BRACONNIER, C. FOUASSIER, P. HAGENMULLER, *Solid State Ionics* 3-4 (1981) 165.
- [76] B.L. Ellis, L.F. Nazar, *Curr. Opin. Solid State Mater. Sci.* 16 (2012) 168.
- [77] S.-W. Kim, D.-H. Seo, X. Ma, G. Ceder, K. Kang, *Adv. Energy Mater.* 2 (2012) 710.
- [78] V. Palomares, M. Casas-Cabanas, E. Castillo-Martínez, M.H. Han, T. Rojo, *Energy Environ. Sci.* 6 (2013) 2312.
- [79] J. Xu, D.H. Lee, Y.S. Meng, *Funct. Mater. Lett.* 06 (2013) 1330001.
- [80] J. Barker, M.Y. Saidi, J.L. Swoyer, *Electrochem. Solid-State Lett.* 6 (2003) A1.
- [81] K. Chihara, A. Kitajou, I.D. Gocheva, S. Okada, J. Yamaki, *J. Power Sources* 227 (2013) 80.
- [82] J. MOLENDÁ, C. DELMAS, P. HAGENMULLER, *Solid State Ionics* 9-10 (1983) 431.
- [83] J.J. Braconnier, C. Delmas, P. Hagenmuller, *Mater. Res. Bull.* 17 (1982) 993.
- [84] Y. Takeda, K. Nakahara, M. Nishijima, N. Imanishi, O. Yamamoto, M. Takano, R. Kanno, *Mater. Res. Bull.* 29 (1994) 659.
- [85] A. Mendiboure, C. Delmas, P. Hagenmuller, *J. Solid State Chem.* 57 (1985) 323.
- [86] N. Yabuuchi, M. Kajiyama, J. Iwatate, H. Nishikawa, S. Hitomi, R. Okuyama, R. Usui, Y. Yamada, S. Komaba, *Nat. Mater.* 11 (2012) 512.
- [87] M. Sathiya, K. Hemalatha, K. Ramesha, J.-M. Tarascon, A.S. Prakash, *Chem. Mater.* 24 (2012) 1846.
- [88] P. Serras, V. Palomares, A. Goñi, I. Gil de Muro, P. Kubiak, L. Lezama, T. Rojo, *J. Mater. Chem.* 22 (2012) 22301.
- [89] A. Ponrouch, A.R. Goni, M.T. Sougrati, M. Ati, J.-M. Tarascon, J. Nava-Avendano, M.R. Palacin, *Energy Environ. Sci.* (2013).
- [90] A. Kitajou, H. Komatsu, K. Chihara, I.D. Gocheva, S. Okada, J. Yamaki, *J. Power Sources* 198 (2012) 389.
- [91] A. Kitajou, H. Komatsu, K. Chihara, I.D. Gocheva, S. Okada, J. Yamaki, *J. Power Sources* 198 (2012) 389.
- [92] N. Dimov, A. Nishimura, K. Chihara, A. Kitajou, I.D. Gocheva, S. Okada, *Electrochim. Acta* 110 (2013) 214.
- [93] A. Basa, E. Gonzalo, A. Kuhn, F. García-Alvarado, *J. Power Sources* 197 (2012) 260.
- [94] R. a. Shakoór, S.Y. Lim, H. Kim, K.-W. Nam, J.K. Kang, K. Kang, J.W. Choi, *Solid State Ionics* 218 (2012) 35.
- [95] G. Pascal, M. Fouletier, *Solid State Ionics* 28-30 (1988) 1172.
- [96] D.A. Stevens, J.R. Dahn, *J. Electrochem. Soc.* 148 (2001) A803.
- [97] M.M. Doeff, *J. Electrochem. Soc.* 140 (1993) L169.

- [98] J.R. Dahn, W. Xing, Y. Gao, Carbon N. Y. 35 (1997) 825.
- [99] D.A. Stevens, J.R. Dahn, J. Electrochem. Soc. 147 (2000) 1271.
- [100] J. Zhao, L. Zhao, K. Chihara, S. Okada, J. Yamaki, S. Matsumoto, S. Kuze, K. Nakane, J. Power Sources 244 (2013) 752.
- [101] A. Ponrouch, A.R. Goñi, M.R. Palacín, Electrochem. Commun. 27 (2013) 85.
- [102] V.L. Chevrier, G. Ceder, J. Electrochem. Soc. 158 (2011) A1011.
- [103] S. Komaba, Y. Matsuura, T. Ishikawa, N. Yabuuchi, W. Murata, S. Kuze, Electrochem. Commun. 21 (2012) 65.
- [104] A. Darwiche, C. Marino, M.T. Sougrati, B. Fraisse, L. Stievano, L. Monconduit, J. Am. Chem. Soc. 134 (2012) 20805.
- [105] A. Maazaz, C. Delmas, P. Hagenmuller, J. Incl. Phenom 1 (1983) 45.
- [106] G. Rousse, M.E. Arroyo-de Dompablo, P. Senguttuvan, A. Ponrouch, J.-M. Tarascon, M.R. Palacín, Chem. Mater. 25 (2013) 4946.
- [107] P. Senguttuvan, M.R. Palacín, (2011) 3.
- [108] W. Wang, C. Yu, Y. Liu, J. Hou, H. Zhu, S. Jiao, RSC Adv. 3 (2013) 1041.
- [109] P. Senguttuvan, Hunting for New Ti- Based Negative Electrodes for the Emerging Na- Ion Technology, Université de Picardie Jules Verne, 2013.
- [110] A. Rudola, K. Saravanan, C.W. Mason, P. Balaya, J. Mater. Chem. A 1 (2013) 2653.
- [111] J. Xu, C. Ma, M. Balasubramanian, Y.S. Meng, Chem. Commun. (Camb). (2014).
- [112] W. Wang, C. Yu, Z. Lin, J. Hou, H. Zhu, S. Jiao, Nanoscale 5 (2013) 594.
- [113] D.W. Aldous, P. Lightfoot, Solid State Sci. 11 (2009) 315.
- [114] D.B. Williams, C.B. Carter, Transmission Electron Microscopy, Springer US, Boston, MA, 2009.
- [115] V. Primo, Powder Diffr. 14 (1999) 70.
- [116] J. Rodríguez-Carvajal, Phys. B Condens. Matter 192 (1993) 55.
- [117] A. Boulfif, D. Louër, J. Appl. Crystallogr. 37 (2004) 724.
- [118] O. Vallcorba, J. Rius, C. Frontera, I. Peral, C. Miravittles, J. Appl. Crystallogr. 45 (2012) 844.
- [119] J. Rius, Acta Crystallogr. A. 67 (2011) 63.
- [120] B. Ravel, M. Newville, J. Synchrotron Radiat. 12 (2005) 537.
- [121] X.-G. Sun, C.A. Angell, Electrochem. Commun. 7 (2005) 261.
- [122] a. Abouimrane, I. Belharouak, K. Amine, Electrochem. Commun. 11 (2009) 1073.

- [123] J.-M. Tarascon, A.S. Gozdz, C. Schmutz, F. Shokoohi, P.C. Warren, *Solid State Ionics* 86-88 (1996) 49.
- [124] R.A. Huggins, *Advanced Batteries*, Springer US, Boston, MA, 2009.
- [125] J.B. Leriche, S. Hamelet, J. Shu, M. Morcrette, C. Masquelier, G. Ouvrard, M. Zerrouki, P. Soudan, S. Belin, E. Elkaïm, F. Baudalet, *J. Electrochem. Soc.* 157 (2010) A606.
- [126] W. Massa, *Acta Crystallogr. Sect. C Cryst. Struct. Commun.* 42 (1986) 644.
- [127] Y.-P. Du, Y.-W. Zhang, Z.-G. Yan, L.-D. Sun, S. Gao, C.-H. Yan, *Chem. Asian J.* 2 (2007) 965.
- [128] J.R. Shane, *J. Appl. Phys.* 38 (1967) 1280.
- [129] K.K. Sand, J.D. Rodriguez-Blanco, E. Makovicky, L.G. Benning, S.L.S. Stipp, *Cryst. Growth Des.* 12 (2012) 842.
- [130] J. Yin, F. Gao, C. Wei, Q. Lu, *Sci. Rep.* 4 (2014) 3736.
- [131] F. Manoli, E. Dalas, *J. Cryst. Growth* 218 (2000) 359.
- [132] M.S. Tung, T.J. O'Farrell, *Colloids Surfaces A Physicochem. Eng. Asp.* 110 (1996) 191.
- [133] E.L. Bustamante, J.L. Fernández, J.M. Zamaro, *J. Colloid Interface Sci.* 424 (2014) 37.
- [134] W.S. Sheldrick, M. Wachhold, *Angew. Chemie Int. Ed. English* 36 (1997) 206.
- [135] E. Hawlicka, D. Swiatla-Wojcik, *J. Phys. Chem. A* 106 (2002) 1336.
- [136] P. Núñez, T. Roisnel, A. Tressaud, *Solid State Commun.* 92 (1994) 601.
- [137] a. Ratuszna, K. Majewska, T. Lis, *Acta Crystallogr. Sect. C Cryst. Struct. Commun.* 45 (1989) 548.
- [138] W. Massa, *Acta Crystallogr. Sect. C Cryst. Struct. Commun.* 42 (1986) 644.
- [139] M.R.P. A.Ponrouch, D. Monti, A. Boschini, B. Steen. P. Johansson, *Submitt. Publ.* (n.d.).
- [140] F. Rosi, A. Daveri, B. Doherty, S. Nazzareni, B.G. Brunetti, A. Sgamellotti, C. Miliani, *Appl. Spectrosc.* 64 (2010) 956.
- [141] P.K. Mandal, T.K. Mandal, 32 (2002) 313.
- [142] K. Nakamoto, *Infrared and Raman Spectra of Inorganic and Coordination Compounds*, 6th ed., Wiley, 2009.
- [143] A. Vimont, J.-C. Lavalley, L. Francke, A. Demourgues, A. Tressaud, M. Daturi, *J. Phys. Chem. B* 108 (2004) 3246.
- [144] A. Demourgues, N. Penin, D. Dambournet, R. Clarenc, A. Tressaud, E. Durand, *J. Fluor. Chem.* 134 (2012) 35.
- [145] J. Sheng, K. Tang, W. Cheng, J. Wang, Y. Nie, Q. Yang, *J. Hazard. Mater.* 171 (2009) 279.
- [146] C.L. Ross, M. Christ, *Am. Mineral.* 43 (1958) 1157.
- [147] L. Pauling, *J. Am. Chem. Soc.* 51 (1929) 1010.

- [148] M.R. Marvel, R.A.F. Pinlac, J. Lesage, C.L. Stern, K.R. Poeppelmeier, *Z. Anorg. Allg. Chem.* 635 (2009) 869.
- [149] D. Pesche, B. Babel, *Z. Anorg. Allg. Chem.* 623 (1997) 1614.
- [150] D. Courbion, G. Férey, G. Holler, H. Babel, *Eur. J. Solid State Inorg. Chem.* 25(4) (1988) 435.
- [151] J. Andersson, S. Galy, *Acta Crystallogr. B* 25 (1969) 847.
- [152] P. a Maggard, T.S. Nault, C.L. Stern, K.R. Poeppelmeier, *J. Solid State Chem.* 175 (2003) 27.
- [153] J.M. Chamberlain, T.A. Albrecht, J. Lesage, F. Sauvage, C.L. Stern, K.R. Poeppelmeier, *Cryst. Growth Des.* 10 (2010) 4868.
- [154] J.L. Fourquet, H. Duroy, M.P. Crosnier-Lopez, *Zeitschrift Für Anorg. Und Allg. Chemie* 623 (1997) 439.
- [155] J.E. Kirsch, H.K. Izumi, C.L. Stern, K.R. Poeppelmeier, *Inorg. Chem.* 44 (2005) 4586.
- [156] A. Clearfield, A. Moini, P.R. Rudolf, *Inorg. Chem.* 24 (1985) 4606.
- [157] H. Shorafa, H. Ficioglu, F. Tamadon, F. Girgsdies, K. Seppelt, *Inorg. Chem.* 49 (2010) 4263.
- [158] P. Moutou, J-M. Chaminade, J-P. Pouchard, M. Hagenmuller, *Rev. Chim. Minérale.* 23 (1986) 27.
- [159] D.W. Aldous, P. Lightfoot, *Solid State Sci.* 11 (2009) 315.
- [160] G. Silversmit, J. a. van Bokhoven, H. Poelman, A.M.J. van der Eerden, G.B. Marin, M.-F. Reyniers, R. De Gryse, *Appl. Catal. A Gen.* 285 (2005) 151.
- [161] J. Wong, F. Lytle, R. Messmer, D. Maylotte, *Phys. Rev. B* 30 (1984).
- [162] W. Avansi, L.J.Q. Maia, C. Ribeiro, E.R. Leite, V.R. Mastelaro, *J. Nanoparticle Res.* 13 (2011) 4937.
- [163] P. Bukovec, L. Golič, *Acta Crystallogr. Sect. B Struct. Crystallogr. Cryst. Chem.* 36 (1980) 1925.
- [164] M. SCHABERT, G. PAUSEWANG, *Zeitschrift Für Naturforschung. Tl. B, Anorg. Chemie, Org. Chemie* 40 (n.d.) 1437.
- [165] D.P.P. Grandjean, R.O. Benfield, C. Nayral, A. Maisonnat, B. Chaudret, *J. Phys. Chem. B* 108 (2004) 8876.
- [166] L. He, H. Yuan, K. Huang, C. Yan, G. Li, Q. He, Y. Yu, S. Feng, *J. Solid State Chem.* 182 (2009) 2208.
- [167] L. He, H. Yuan, K. Huang, C. Yan, G. Li, Q. He, Y. Yu, S. Feng, *J. Solid State Chem.* 182 (2009) 2208.
- [168] K. Suzuki, *J. Phys. Soc. Japan* 64 (1995) 674.
- [169] J.-C. Cros, C. Dance, J-M. Grenier, *Mat. Res. Bull* 12 (1977) 415.
- [170] A. Pantelouris, H. Modrow, M. Pantelouris, J. Hormes, D. Reinen, *Chem. Phys.* 300 (2004) 13.

- [171] M. Vlasse, F. Menil, C. Moriliere, J.M. Dance, A. Tressaud, J. Portier, J. Solid State Chem. 17 (1976) 291.
- [172] S. Becker, B.G. Müller, Angew. Chemie 102 (1990) 426.
- [173] (n.d.).
- [174] W.T. Fu, D.J.W. IJdo, J. Solid State Chem. 181 (2008) 1236.
- [175] R. Shannon, R. Fischer, Phys. Rev. B 73 (2006) 235111.
- [176] M. V. Reddy, S. Madhavi, G. V. Subba Rao, B.V.R. Chowdari, J. Power Sources 162 (2006) 1312.
- [177] S. Andersson, A.D. Wadsley, Acta Crystallogr. 14 (1961) 1245.
- [178] J.C. Pérez-Flores, F. García-Alvarado, M. Hoelzel, I. Sobrados, J. Sanz, A. Kuhn, Dalton Trans. 41 (2012) 14633.
- [179] Y. Bando, M. Watanabe, Y. Sekikawa, Acta Crystallogr. Sect. B Struct. Crystallogr. Cryst. Chem. 35 (1979) 1541.
- [180] A.D. Wadsley, W.G. Mumme, Acta Crystallogr. Sect. B Struct. Crystallogr. Cryst. Chem. 24 (1968) 392.
- [181] G.F. Schafer, Zeitschrift Für Krist. 1986 (1986) 269.
- [182] H. Li, P. Balaya, J. Maier, J. Electrochem. Soc. 151 (2004) A1878.
- [183] M. Dahbi, N. Yabuuchi, K. Kubota, K. Tokiwa, S. Komaba, Phys. Chem. Chem. Phys. 16 (2014) 15007.
- [184] V. Palomares, P. Serras, I. Villaluenga, K.B. Hueso, J. Carretero-González, T. Rojo, Energy Environ. Sci. 5 (2012) 5884.
- [185] P.R. Slater, J. Fluor. Chem. 117 (2002) 43.
- [186] F.J. Berry, X. Ren, R. Heap, P. Slater, M.F. Thomas, Solid State Commun. 134 (2005) 621.
- [187] R. Heap, P.R. Slater, F.J. Berry, O. Helgason, A.J. Wright, Solid State Commun. 141 (2007) 467.
- [188] O. Clemens, R. Haberkorn, P.R. Slater, H.P. Beck, Solid State Sci. 12 (2010) 1455.
- [189] T. Wei, Y. Gong, X. Zhao, K. Huang, Adv. Funct. Mater. 24 (2014) 5380.
- [190] T.P. Feist, P.K. Davies, J. Solid State Chem. 101 (1992) 275.
- [191] M. Shirpour, J. Cabana, M. Doeff, Chem. Mater. 26 (2014) 2502.
- [192] Y. Ide, M. Ogawa, Angew. Chem. Int. Ed. Engl. 46 (2007) 8449.
- [193] E.A. Behrens, P. Sylvester, A. Clearfield, Environ. Sci. Technol. 32 (1998) 101.
- [194] F. Farges, G. Brown, J. Rehr, Phys. Rev. B 56 (1997) 1809.

- [195] Y.-B. He, B. Li, M. Liu, C. Zhang, W. Lv, C. Yang, J. Li, H. Du, B. Zhang, Q.-H. Yang, J.-K. Kim, F. Kang, *Sci. Rep.* 2 (2012) 913.
- [196] S. Papp, L. Körösi, V. Meynen, P. Cool, E.F. Vansant, I. Dékány, *J. Solid State Chem.* 178 (2005) 1614.
- [197] H. Liu, D. Yang, Z. Zheng, X. Ke, E. Waclawik, H. Zhu, R.L. Frost, *J. Raman Spectrosc.* 41 (2010) 1331.

